

8-2011

Dual Energy Computed Tomography For Proton Therapy Treatment Planning

Ming Yang

Follow this and additional works at: https://digitalcommons.library.tmc.edu/utgsbs_dissertations



Part of the [Other Physics Commons](#)

Recommended Citation

Yang, Ming, "Dual Energy Computed Tomography For Proton Therapy Treatment Planning" (2011).
Dissertations and Theses (Open Access). 167.
https://digitalcommons.library.tmc.edu/utgsbs_dissertations/167

This Dissertation (PhD) is brought to you for free and open access by the MD Anderson UTHealth Houston Graduate School at DigitalCommons@TMC. It has been accepted for inclusion in Dissertations and Theses (Open Access) by an authorized administrator of DigitalCommons@TMC. For more information, please contact digcommons@library.tmc.edu.

**DUAL ENERGY COMPUTED TOMOGRAPHY FOR PROTON
THERAPY TREATMENT PLANNING**

by

Ming Yang, M.S.

APPROVED:

Lei Dong, Ph.D.
Supervisory Professor

Narayan Sahoo, Ph.D.

Chris C. Shaw, Ph.D.

Uwe Titt, Ph.D.

Susan L. Tucker, Ph.D.

Ronald X. Zhu, Ph.D.

APPROVED:

Dean, The University of Texas
Health Science Center at Houston
Graduate School of Biomedical Sciences

DUAL ENERGY COMPUTED TOMOGRAPHY FOR PROTON THERAPY
TREATMENT PLANNING

A
DISSERTATION

Presented to the Faculty of
The University of Texas
Health Science Center at Houston
Graduate School of Biomedical Sciences
and
The University of Texas
M. D. Anderson Cancer Center

in Partial Fulfillment
of the Requirements
for the Degree of
DOCTOR OF PHILOSOPHY

by

Ming Yang, M.S.
Houston, Texas

August 2011

Dedication

I would like to dedicate this work to my parents and my dear wife.

Acknowledgements

I would like to thank my advisor, Dr. Lei Dong, for his time and effort devoted to my graduate study. I have benefited a lot from his mentoring, both professionally and personally. I am truly grateful for that. I would also like to thank Dr. Ronald X. Zhu for his suggestions on my analysis of the range uncertainty in current practice. Thank you to the remainder of my committee, Dr. Sahoo, Dr. Shaw, Dr. Titt and Dr. Tucker, for providing invaluable advice on my research project and presentation skills.

I would like to thank Dr. Rong and Dr. Cody for helping me with the kV measurements. I would also like to thank Dr. McGary from the Methodist Hospital for his help with MV measurements using the TomoTherapy machine. I would also like to thank the QA physicist assistants for providing me the phantoms and equipments for my measurements. I would also like to thank Jennifer Johnson for her help with improving my clinical skills. I would also like to thank the Varian Medical Systems for their financial support. I also want to express my gratitude to Dr. Ed Jackson and Georgeanne Moore for their dedication in creating a healthy education environment within the graduate program. Thank you to all other faculty members and staff that have helped me personally or academically along the way.

I would like to thank my fellow graduate students Yevgeney Vinogradsky, Annelise Giebler, Adam Melancon, Adam Riegel, Derek Yaldo, Peter Park, Henry Yu, Joey Cheung, and Adam Yock for their help and friendship along the way.

Finally, I would like to thank my parents, Fengying Zhao and Jincheng Yang, and my dear wife, Qingyan Kong, for their unconditional love and support.

DUAL ENERGY COMPUTED TOMOGRAPHY FOR PROTON THERAPY TREATMENT PLANNING

Publication No. _____

Ming Yang, M.S.

Supervisory Professor: Lei Dong, Ph.D.

Abstract

Proton radiation therapy is gaining popularity because of the unique characteristics of its dose distribution, e.g., high dose-gradient at the distal end of the percentage-depth-dose curve (known as the Bragg peak). The high dose-gradient offers the possibility of delivering high dose to the target while still sparing critical organs distal to the target. However, the high dose-gradient is a double-edged sword: a small shift of the highly conformal high-dose area can cause the target to be substantially under-dosed or the critical organs to be substantially over-dosed. Because of that, large margins are required in treatment planning to ensure adequate dose coverage of the target, which prevents us from realizing the full potential of proton beams. Therefore, it is critical to reduce uncertainties in the proton radiation therapy.

One major uncertainty in a proton treatment is the range uncertainty related to the estimation of proton stopping power ratio (SPR) distribution inside a patient. The SPR distribution inside a patient is required to account for tissue heterogeneities when calculating dose distribution inside the patient. In current clinical practice, the SPR distribution inside a patient is estimated from the patient's treatment planning computed tomography (CT) images based on the CT number-to-SPR calibration curve. The SPR

derived from a single CT number carries large uncertainties in the presence of human tissue composition variations, which is the major drawback of the current SPR estimation method. We propose to solve this problem by using dual energy CT (DECT) and hypothesize that the range uncertainty can be reduced by a factor of two from currently used value of 3.5%.

A MATLAB program was developed to calculate the electron density ratio (EDR) and effective atomic number (EAN) from two CT measurements of the same object. An empirical relationship was discovered between mean excitation energies and EANs existing in human body tissues. With the MATLAB program and the empirical relationship, a DECT-based method was successfully developed to derive SPRs for human body tissues (the DECT method). The DECT method is more robust against the uncertainties in human tissues compositions than the current single-CT-based method, because the DECT method incorporated both density and elemental composition information in the SPR estimation.

Furthermore, we studied practical limitations of the DECT method. We found that the accuracy of the DECT method using conventional kV-kV x-ray pair is susceptible to CT number variations, which compromises the theoretical advantage of the DECT method. Our solution to this problem is to use a different x-ray pair for the DECT. The accuracy of the DECT method using different combinations of x-ray energies, i.e., the kV-kV, kV-MV and MV-MV pair, was compared using the measured imaging uncertainties for each case. The kV-MV DECT was found to be the most robust against CT number variations. In addition, we studied how uncertainties

propagate through the DECT calculation, and found general principles of selecting x-ray pairs for the DECT method to minimize its sensitivity to CT number variations.

The uncertainties in SPRs estimated using the kV-MV DECT were analyzed further and compared to those using the stoichiometric method. The uncertainties in SPR estimation can be divided into five categories according to their origins: the inherent uncertainty, the DECT modeling uncertainty, the CT imaging uncertainty, the uncertainty in the mean excitation energy, and SPR variation with proton energy. Additionally, human body tissues were divided into three tissue groups – low density (lung) tissues, soft tissues and bone tissues. The uncertainties were estimated separately because their uncertainties were different under each condition. An estimate of the composite range uncertainty (2σ) was determined for three tumor sites – prostate, lung, and head-and-neck, by combining the uncertainty estimates of all three tissue groups, weighted by their proportions along typical beam path for each treatment site.

In conclusion, the DECT method holds theoretical advantages in estimating SPRs for human tissues over the current single-CT-based method. Using existing imaging techniques, the kV-MV DECT approach was capable of reducing the range uncertainty from the currently used value of 3.5% to 1.9%-2.3%, but it is short to reach our original goal of reducing the range uncertainty by a factor of two. The dominant source of uncertainties in the kV-MV DECT was the uncertainties in CT imaging, especially in MV CT imaging. Further reduction in beam hardening effect, the impact of scatter, out-of-field object etc. would reduce the Hounsfield Unit variations in CT imaging. The kV-MV DECT still has the potential to reduce the range uncertainty further.

TABLE OF CONTENTS

TABLE OF CONTENTS	VIII
LIST OF TABLES.....	XIV
LIST OF FIGURES	XVIII
CHAPTER 1. BACKGROUND.....	1
1.1 Proton Radiation Therapy	1
1.1.1 Brief History	1
1.1.2 Proton Interactions.....	1
1.1.3 Delivery Techniques	3
1.1.4 Treatment Planning Systems	4
1.1.5 Range Uncertainties	5
1.2 CT Imaging	7
1.2.1 Artifacts	7
1.2.2 Dual Energy Computed Tomography (DECT).....	10
1.3 Methods of Deriving Proton Stopping Power Ratio (SPR)	12
1.3.1 CT Number-to-SPR Calibration Curve	12
1.3.2 Proton CT.....	14
1.4 Degeneracy Issue in the SPR Estimation.....	15
CHAPTER 2: HYPOTHESIS AND SPECIFIC AIMS.....	19

CHAPTER 3: SPECIFIC AIM I - ESTIMATION OF RANGE UNCERTAINTIES (SPR-RELATED) IN CURRENT PRACTICE	20
3.1 Introduction	20
3.2 Methods and Materials	21
3.2.1 Terminology	21
3.2.2 Stoichiometric Calibration Method	22
3.2.2.1 Determination of CT Scanner Specific Parameters.....	22
3.2.2.2 Bethe-Bloch Equation	24
3.2.2.3 Our Calibration	26
3.2.3 Uncertainties in SPR Estimation	32
3.2.3.1 Inherent Uncertainties	34
3.2.3.2 Modeling Errors in Predicted CT Numbers	36
3.2.3.3 CT Imaging Uncertainties	36
3.2.3.4 Uncertainties in Mean Excitation Energies	40
3.2.3.5 SPR Variations with Proton Energies	41
3.2.3.6 Composite Range Uncertainty.....	42
3.3 Results	45
3.3.1 Uncertainties in SPR Estimation	45
3.3.1.1 Inherent Uncertainties	45
3.3.1.2 Modeling Errors in Predicted CT Numbers	48

3.3.1.3	CT Imaging Uncertainties	50
3.3.1.4	Uncertainties in Mean Excitation Energies	56
3.3.1.5	SPR Variations with Proton Energies	57
3.3.1.6	Composite Range Uncertainty.....	60
3.4	Discussion	62
3.4.1	Comparison of Our Estimates with the Estimates from Other Groups	62
3.4.2	Measures to Mitigate Uncertainties in Current Practice.....	69
CHAPTER 4: SPECIFIC AIM II – DEVELOPMENT OF THE DECT METHOD.....		72
4.1	Introduction.....	72
4.2	Methods and Materials.....	72
4.2.1	Two-parameter Model	72
4.2.2	Our DECT Method of Deriving SPRs from EDRs and EANs	74
4.3	Results.....	77
4.3.1	Accuracy of EDR and EAN Calculation	78
4.3.2	Accuracy of SPR Derivation	79
4.3.2.1	‘Reference’ Human Tissues	80
4.3.2.2	Single Tissue Composition Variations	81
4.3.2.3	‘Individualized’ Human Tissues	83
4.4	Discussion	84
4.4.1	CT Calibration for DECT Calculation.....	84

4.4.2	Our Recipe for Implementing the DECT Method	89
CHAPTER 5. SPECIFIC AIM III – DEVELOPING CRITERIA FOR SELECTING X-RAY PAIRS FOR DECT		
		91
5.1	Introduction	91
5.2	Methods and Materials	92
5.2.1	Selection of Three Representative X-ray Pairs	92
5.2.2	Simulation of Random Noise and Beam Hardening Effect	94
5.2.3	Uncertainty Propagation	96
5.3	Results	98
5.3.1	Comparison of Three Representative X-ray Pairs	98
5.3.1.1	Tissue Composition Variations	98
5.3.1.2	Random Noise	99
5.3.1.3	Uncertainty Propagation	100
5.3.2	Comparison of Mono-energetic X-ray Pairs	102
5.4	Discussion	104
5.4.1	Criteria for Selecting X-ray Pairs	104
5.4.2	Interesting Observations about DECT Calculations	105
CHAPTER 6: SPECIFIC AIM IV – ESTIMATION OF MARGIN REDUCTION BY USING DECT		
		108
6.1	Introduction	108

6.2	Methods and Materials.....	108
6.2.1	Uncertainties in SPR Estimates Using the DECT Method.....	108
6.3	Results.....	109
6.3.1	Selection of the Best kV Beam to Pair with the MV Beam.....	110
6.3.2	MV Measurements using the TomoTherapy Machine	111
6.3.3	Summary.....	113
6.4	Discussion	114
6.4.1	Comparison of the DECT Method and the Stoichiometric Method	114
6.4.2	Measures to Improve the DECT Method's Accuracy	116
6.4.3	Practical Limitations of Estimating Patient SPRs Using DECT	117
6.4.4	Other Benefits of DECT	119
CHAPTER 7: CONCLUSIONS		122
7.1	Specific Aim I – Estimation of Range Uncertainty (SPR-related) in Current Practice	122
7.2	Specific Aim II – Development of the DECT Method	122
7.3	Specific Aim III – Developing Criteria for Selecting X-ray Pairs for DECT...123	
7.4	Specific Aim IV – Estimation of Margin Reduction using the DECT	123
7.5	Testing the Hypothesis.....	124
APPENDIX A – ESTIMATION OF UNCERTAINTIES IN HUMAN TISSUE COMPOSITIONS PUBLISHED IN THE LITERATURE		125

APPENDIX B – METAL ARTIFACT REDUCTION USING HIGH ENERGY COMPUTED	
TOMOGRAPHY	133
REFERENCES	139

LIST OF TABLES

Table 1. Recommended elemental compositions and densities (ρ) of air, water and human tissue substitutes provided with the RMI 467 phantom.	29
Table 2. Recommended elemental compositions and densities (ρ) of human body tissues from the literature.	29
Table 3. Summary of the systematic uncertainty (δ) and statistical uncertainty (σ) in the recommended values of the ‘reference’ human tissues.....	36
Table 4. Variation ratios calculated for tissue substitutes used to measure CT imaging uncertainties.	40
Table 5. Statistics of the inherent uncertainties (1σ) in SPRs of the ‘reference’ human body tissues estimated using the stoichiometric method.	46
Table 6. Statistics of the inherent uncertainties (1σ) in SPRs of the ‘individualized’ human body tissues estimated using the stoichiometric method.	48
Table 7. Statistics of the modeling errors (1σ) in predicted CT numbers of the tissue substitutes and the induced errors in estimated SPRs.	50
Table 8. CT measurements of tissue substitute inserts scanned during monthly QA for three treatment planning CT scanners at UTMDACC.....	51
Table 9. Statistics of CT number variations with time and scanner and the induced SPR variations for tissue substitutes.	51
Table 10. Statistics of relative CT number and SPR variations (1σ) with time and scanner for different tissue groups.....	52
Table 11. CT measurements of various tissue substitutes scanned at the center of the head phantom and the body phantom, respectively, and the relative differences in CT numbers and	

SPRs related to the size of the phantom. The maximal relative difference was determined based on the absolute values of relative differences of all the tissues within one tissue group.	53
Table 12. CT measurements of various tissue substitutes scanned at the center and the periphery of the body phantom, respectively, and the relative differences in CT numbers and SPRs related to the position in the phantom. The maximal relative difference was determined based on the absolute values of relative differences of all the tissue substitutes within one tissue group.....	54
Table 13. CT measurements of various tissue substitutes scanned in the RMI 467 phantom with two different couch positions, respectively, and the relative differences in CT numbers and SPRs. The maximal relative difference was determined based on the absolute values of relative differences of all the tissues within one tissue group.....	55
Table 14. Statistics of CT number uncertainties (1σ) due to different factors and the induced uncertainties in SPRs for different tissue groups.	56
Table 15. Statistics of relative differences in calculated SPRs due to variations of the elemental mean excitation energies.	57
Table 16. Summary of our estimates of relative range uncertainties (1σ) related to proton SPR estimation in current clinical practice.	61
Table 17. Mean, standard deviation (σ) and standard error of mean (SEM) of relative weights of each tissue group in different clinical situations.....	62
Table 18. Median, 90th percentile and 95th percentile of composite range uncertainties and the corresponding percentile when range uncertainty is equal to 3.5%, respectively, at different clinical situations.....	62
Table 19. Proton SPRs for adipose tissue and cortical bone at different proton energies and their relative differences compared to the SPRs at 175 MeV.....	66
Table 20. Comparison of our estimates of the relative range uncertainties (SPR related) and the estimates from the literature.....	68

Table 21. Comparison of the calculated and measured CT numbers of various tissue substitutes for the 100 kVp beam. The calculated CT numbers were based on the best-match mono-energy (70.0 keV) to the measured CT numbers. The measured CT numbers were further adjusted using the calibration curve shown in Fig. 25 so that they match with the calculated CT numbers.	87
Table 22. Comparison of the calculated and measured CT numbers of various tissue substitutes for the 100 kVp beam. The calculated CT numbers were based on the 100 kVp spectrum determined from Monte Carlo simulations. The measured CT numbers were adjusted using the calibration curve determined in Fig. 26 for better fitting.	88
Table 23. Ratios of absolute EAN variations and relative EDR variations over relative CT number variations in the DECT calculations for different x-ray energy pairs. The values were averaged of all tissue types within each tissue group.....	102
Table 24. SPR sensitivity ratio factors, R_L and R_H , calculated for all three x-ray beam pairs. The values were averaged of all tissue types within each tissue group.....	102
Table 25. Sensitivity ratio factors calculated for the 80 kVp, 100 kVp, 120 kVp and 140 kVp beams, respectively, when paired with the 1 MV beam.....	111
Table 26. Our estimates of imaging uncertainties (1σ) of the 80 kVp, 100 kVp, 120 kVp and 140 kVp beams.....	111
Table 27. Statistics of modeling uncertainties (1σ) for the 80 kVp, 100 kVp, 120 kVp, 140 kVp beams and the MV beam of the TomoTherapy machine.	111
Table 28. Statistics of CT number uncertainties ($1-\sigma$) due to different factors for different tissue groups for the MV TomoTherapy beam.	113
Table 29. Summary of our estimates of the relative SPR uncertainties ($1-\sigma$) when using the DECT with the 80 kVp – 1 MV pair.....	114
Table 30. Summary of comparison of the DECT method and the stoichiometric method.	116

Table 31. Comparison of the recommended density values of the same human tissue type from different publications.	126
Table 32. Mean densities ($\langle\rho\rangle$) and standard deviations (σ) of human tissues from Woodard and White (1986). The relative standard deviation (σ_{rel}) was also calculated.....	127
Table 33. Compositions of seven human tissues from Woodard and White (1986) and the calculated standard deviation of hydrogen percentages (σ'_H). Three tissue compositions are provided for each human tissue: mean and mean ± 1 standard deviation (σ). The hydrogen percentage was calculated based on the relative weight by mass and the hydrogen percentage of each tissue component.....	129
Table 34. Hydrogen percentages of major lipid substances from Woodard and White (1986).	129
Table 35. Hydrogen percentages of amino acids.	129
Table 36. Our estimates of the uncertainties corresponding to the first three items in Eq. 33 given by Woodard and White (1986) (σ'_H), our estimates of the uncertainties corresponding to the last three items in Eq. 33 ($\omega_W*\sigma_{HW}$ for water, $\omega_L*\sigma_{HL}$ for lipid, and $\omega_P*\sigma_{HP}$ for protein), and the total uncertainty (σ_H) calculated using Eq. 33 for seven human tissue types.....	130
Table 37. Calcium percentages in human cortical bone.....	131
Table 38. This table lists the materials of inserts used in the RMI 467 phantom and their positions in the phantom. The positions here correspond to the labels used in Fig. 33. Also listed are the nominal electron densities relative to water (EDRs), the mean CT number, and the standard error of the mean (SEM) CT number within the material insert.....	135

LIST OF FIGURES

Figure 1. An example CT number-to-SPR calibration curve. The proton SPR is derived from the CT number.	14
Figure 2. Demonstration of the degeneracy issue in SPR estimation based on the calibration curve. The skin and thyroid have close CT numbers but have very different SPRs. Another four human tissues (in the small red circle) have different CT numbers but have close SPRs. In either case, the uncertainties arise in SPRs estimated based on a single CT number and the calibration curve.....	16
Figure 3. Demonstration of sensitivity of current SPR estimation method to human tissue composition variations. The mandible with the published density and elemental composition fall on the calibration curve perfectly, so a negligible error (uncertainty) results when estimating its SPR based on the calibration curve. But when this mandible's density or calcium percentage is changed by 5%, it deviates from the calibration curve, which causes a large error in its estimated SPR.	18
Figure 4. Images of (a) the RMI 467 tissue characterization phantom and (b) the head- and body-size calibration phantoms.....	27
Figure 5. Stoichiometric calibration curves determined for the kV scanner (ACB CT1).....	28
Figure 6. Illustration of uncertainties in proton SPRs estimated using the stoichiometric calibration method. The blue triangles represent 'reference' human body tissues and the black solid line represents the stoichiometric calibration curve. The first category of uncertainties is the inherent uncertainty caused by the differences between the calculated SPRs and the SPRs derived based on the calibration curve. The other two categories of uncertainties are the uncertainties in the calculation of CT numbers and SPRs for the 'reference' human body tissues.	33

Figure 7. Axial CT images of the head phantom and the body phantom with the same tissue substitute insert at the center.	38
Figure 8. Axial CT images of the body phantom with the same tissue insert at the center and at the periphery.	38
Figure 9. Axial CT images of the RMI 467 phantom with two different couch positions: one inside the FOV and one outside the FOV.	39
Figure 10. (a) CT number histogram for lung, prostate and head-and-neck patients; (b) The zoomed-in version of (a), which shows 800 and 1200 can be used to separate soft tissues from lung tissues and bone tissues.	45
Figure 11. Histogram of the inherent uncertainties in SPRs of the ‘reference’ human body tissues estimated using the stoichiometric method.	46
Figure 12. CT calibration curve shown with the ‘reference’ body tissues and the ‘individualized’ body tissues. (a) and (b) are zoomed in on the soft tissue and bone tissue region, respectively.	48
Figure 13. Histograms of the inherent uncertainties in proton SPRs of the ‘individualized’ human body tissues estimated using the stoichiometric method.	48
Figure 14. (a) Measured versus calculated CT numbers of the tissue substitutes; (b) The difference between the measured and calculated CT numbers of the tissues substitutes relative to the calculated CT numbers.	50
Figure 15. Histograms of relative differences between the SPRs calculated based on the original elemental mean excitation energies and the SPRs calculated based on the values with variations for all 41 ‘reference’ human tissues (Table 2). The histograms were based on the maximal relative differences among all three scenarios.	57
Figure 16. Projected proton range in water at different energies from the NIST PSTAR database.	59

Figure 17. (a) relative and (b) absolute error in the calculated proton range caused by using SPRs based on a single energy of 175MeV versus the projected range in water for the adipose tissue (×) and cortical bone (♦).	60
Figure 18. (a) relative and (b) absolute error in proton range calculation induced by using SPRs of 175 MeV (black) and 100 MeV (blue), respectively, versus the projected range in water for the adipose tissue (×) and cortical bone (♦).	70
Figure 19. The soft tissue group and bone tissue group had separate linear relationships between the effective atomic number (EAN) and the logarithm of mean excitation energy ($\ln I_m$). Shown are plots for 41 ‘reference’ human body tissues listed in Table 2.....	77
Figure 20. Relative errors in EANs and EDRs of the ‘reference’ human body tissues calculated using our DECT Matlab program.	79
Figure 21. Histograms of relative uncertainties in proton SPRs of the ‘reference’ human tissues estimated using the DECT method and the stoichiometric calibration method, respectively.....	80
Figure 22. Uncertainties in SPRs derived using the stoichiometric and DECT method, respectively, when different levels of variations were introduced to (a) the density, (b) the percentage of the oxygen (O)–carbon (C) pair, (c) the percentage of the hydrogen (H)–oxygen pair and hydrogen–carbon pair and (d) the percentage of the calcium (Ca)–oxygen pair and calcium–carbon pair. The variation was relative for density while the percentage variation for elemental compositions was absolute. The percentage variation on the x -axis was introduced to the first element within each element pair, while the reverse variation was introduced to the second element, in order to keep the total percentage constant.	83
Figure 23. Histograms of relative errors in proton SPRs of the ‘individualized’ human tissues estimated using the DECT method and the stoichiometric calibration method, respectively.....	84
Figure 24. Comparison of CT numbers of various human body tissues and tissue substitutes calculated based on the poly-energetic x-ray beams and their equivalent mono-energetic x-ray beams.	86

Figure 25. Linear regression fit of the calculated and measured CT numbers of various tissue substitutes for the 100 kVp beam (Table 21). The fits were carried out for lung, soft and bone tissue groups separately. The calculated CT numbers were based on the best-match mono-energy (70.0 keV) to the measured CT numbers.	88
Figure 26. Linear regression fit of the calculated and measured CT numbers for various tissue substitutes using a 100 kVp beam (Table 22). The fits were carried out for lung, soft and bone tissue groups separately.....	89
Figure 27. X-ray spectra generated for the (a) 100 kVp and 140 kVp beams and (b) 1MV 0mmCu and 1MV 3mmCu beams using the BEAMnrc Monte Carlo simulation package.	94
Figure 28. Histograms of the relative errors in SPRs estimated using the kV-kV, kV-MV, and MV-MV DECT for the (a) ‘reference’ human body tissues and (b) ‘individualized’ human body tissues. The RMS error was calculated to describe the overall magnitude of uncertainty distribution. The results showed that, under ideal conditions (i.e., without imaging artifacts), the uncertainties in the DECT calculation were independent of the x-ray energy pairs.	99
Figure 29. Dependence of the RMS errors in SPRs estimated using the DECT method on random noise in CT numbers for the ‘reference’ human body tissues.....	100
Figure 30. Relationship between the SPR sensitivity ratio factors (the absolute value of RL and RH) and the energy of (a) the high-energy x-ray beam and (b) the low-energy x-ray beam used for DECT scans. In (a), the energy of the low-energy x-ray beam was 60 keV, and in (b), the energy of the high-energy x-ray beam was 400 keV. Mono-energetic x-ray beams were used in these simulations.	104
Figure 31. Elemental proportions of Hydrogen (H), Potassium (P), Calcium (Ca) and the summation of elemental proportion of Carbon (C), Nitrogen (N) and Oxygen (O), respectively, versus the effective atomic number (EAN) of human bone tissues listed in Table 2.	121
Figure 32. Experimental setup of the bench-top CT imaging system.	134

- Figure 33. Axial CT images of the RMI 467 phantom scanned using KVCT (left) versus OVCT (right) beam, respectively. The arrangement of the inserts is identical in both images, for which the keys are provided in Table 38. The object distortion and streak artifacts are significantly reduced by using OVCT. Note that the same window and level was used for both images. Ten rectangular ROIs were chosen, which were grouped to four groups based on the level of the artifact in KVCT image, to evaluate the CT number deviations of solid water affected by the metal streaking artifact. 134
- Figure 34. Relationship between the relative electron density and the measured CT number (HU) of the materials for x-ray beams with different energy spectra. ‘125 kVp + 1.05mm Cu’ represents the beam of 125 kVp with 1.05mm extra Au filter, and ‘320 kVp + 0mmCu’ represents the beam of 320 kVp with no Au filter. The relationship between relative electron density and the measured CT number are shown to follow a more predictable linear relationship for OVCT than for KVCT. 136
- Figure 35. Stoichiometric CT Number calibration curves for KVCT (a,c) and OVCT (b,d). (c) and (d) are the zoomed-in versions of (a) and (b), respectively. The crosses represent real tissue and the triangles represent tissue substitutes. The solid line represent the calibration curve, which is obtained by three linear regression fit to real tissue points. Real tissue points are shown to fit better with the calibration curve for OVCT than for KVCT. 137
- Figure 36. Comparison of KVCT and OVCT showing the deviation of estimated relative electron densities from true relative electron densities for solid water ROIs belonging to four different groups. ROIs are grouped based on the metal artifact level in KVCT image in Fig. 33(a) – (d) are histograms of the deviation distribution for Group 1 with most severe artifact, Group 2 with heavy artifact, for Group 3 with medium artifact, for Group 4 with least artifact, respectively. The maximal absolute deviation, the root-mean-square (RMS) deviation and the standard deviation (STD) are provided for each deviation distribution. 138

BACKGROUND

1.1 Proton Radiation Therapy

1.1.1 Brief History

Protons were discovered by Ernest Rutherford in 1919 (Rutherford, 1919). In 1946, Robert Wilson proposed to use protons to treat deep-seated tumors, taking advantage of protons' unique dose-deposition characteristics (Wilson, 1946). In 1955, the first patient was treated with proton beams at the Lawrence Berkeley Laboratory (Lawrence *et al.*, 1958). In the following 35 years, the progress in proton radiation therapy was slow. During this period, patients could only receive proton treatments at few research facilities, e.g., the Harvard Cyclotron Laboratory. Nevertheless, the accumulated clinical results confirmed the efficacy of proton radiation therapy. In 1990, the Loma Linda University Medical Center opened the first hospital-based proton treatment facility (Slater *et al.*, 1992), which started a new era of proton radiation therapy. Since then, approximately 30 proton facilities have been built worldwide, and another 24 proton facilities will be built in the next decade, according to the Particle Therapy Co-Operative Group (PTCOG).

1.1.2 Proton Interactions

Protons experience four major interactions when passing through a medium: Coulomb interactions with atomic nuclei and orbiting electrons, elastic and inelastic interactions with atomic nuclei (Lomax, 2009). The Coulomb interactions with orbiting electrons occur much more frequently than the other three interactions. Although

occurring less frequently, the other three interactions have important consequences as well, e.g., degrading the pristine Bragg peak, generating secondary particles, etc.

The Coulomb interaction between a proton and an electron is essentially the electrostatic interaction between two electrically charged particles, which is a long range interaction. A proton loses only a small amount of energy for every interaction with an electron, because the proton has a much larger mass than the electron. It is based on this fact that the continuous-slowing-down-approximation (CSDA) algorithm can be used to estimate the range of protons in a medium. The energy loss over a unit distance, known as the stopping power, is inversely proportional to the square of the proton velocity. Because of the inverse square relationship, the deposited dose (energy) by protons increases substantially toward the end of the proton range, as the proton velocity becomes close to zero. This explains the “Bragg peak” seen at the distal end of the proton percentage-depth-dose (PDD) curve.

The Coulomb interaction between a proton and a nucleus is similar to that between a proton and an electron, except that the proton undergoes a much greater deflection from the Coulomb interaction with the nucleus because of the larger mass of the nucleus. Protons experience numerous such interactions as they penetrate through a medium, known as “multiple Coulomb scattering (MCS).” It is the major cause of deflection and lateral broadening of proton beams.

Elastic and inelastic interactions occur when protons hit target nuclei directly. One significant consequence of these two interactions on the incident protons is that about 1% of the incident protons are ‘lost’ from the beam for every centimeter of penetration of water (Lomax, 2009). In other words, about 20% of the incident protons

are removed due to the nuclear interactions before reaching the depth of the Bragg peak, for a proton beam with a range of 20 cm water-equivalent-thickness (WET) in water. Consequently, the measured Bragg peak is lower than the ideal Bragg peak expected from energy loss alone. In addition, inelastic interactions can generate secondary particles, e.g., secondary neutrons. Secondary neutrons pose additional risk to normal tissues because of their long range and high “relative biological effectiveness (RBE)” (Hall, 2006). The effective radiation dose due to secondary neutrons generated in proton therapies has been studied extensively in the past few years (Polf and Newhauser, 2005; Hall, 2006; Gottschalk, 2006; Anferov, 2010; Zheng *et al.*, 2009; Perez-Andjar *et al.*, 2009). Inelastic interactions can also generate short-lived isotopes, such as positron emitters, ^{15}O and ^{11}C . Currently, active research is being done to test if the distribution of these two isotopes can be used for *in vivo* verification of proton beam delivery and range (Parodi *et al.*, 2007; Knopf *et al.*, 2008; Knopf *et al.*, 2011; Finger and Chin, 2011).

1.1.3 Delivery Techniques

There are two main types of proton delivery techniques in general: the passive scattering technique and the spot scanning technique (Smith, 2009). In the passive scattering technique, the lateral spread of proton beams is achieved by use of scattering devices. Collimators are used to achieve conformity of the radiation field and lateral extension of the targets in the beam’s-eye-view (BEV). In the longitudinal direction, a so-called spread-out-Bragg peak (SOBP) is generated by using range modulator wheels (RMW), wheels of varying thickness rotating through the beam and thus producing an oscillating energy absorber. Conformality of the proton dose with the target volume in

the beam direction is achieved by using a range compensator, in order to account for tissue heterogeneities along the beam path, target surface changes, etc. One drawback of the passive scattering technique is that the SOBP may extend into normal tissues proximal to the target, because the size of the SOBP is determined by the largest extent of the target volume along the beam direction.

For the spot scanning technique, the target volume is scanned by individual Bragg peaks of proton beams exiting the delivery nozzle with individual energies and directions. The beam direction is manipulated by varying the field strength of steering magnets, while the range in the patient is manipulated by changing the energy of the proton beam. In general, the spot scanning technique offers more flexibility, and thus promises superior dose conformity compared to the passive scattering technique. Highly localized dose distributions may be achieved by the proton treatments delivered with the spot scanning technique, especially the so-called intensity modulated proton therapy (IMPT). However, high dose conformity also means high sensitivity to uncertainties, especially the uncertainties in proton range calculations and the uncertainties introduced by intra-fractional patient motion.

1.1.4 Treatment Planning Systems

Most proton treatment planning systems use analytical pencil beam algorithms to calculate proton dose distributions in patients (Smith, 2009). The advantage of the pencil beam algorithms is their fast calculation speed. Its disadvantage is that they are associated with sizable uncertainties under some conditions, e.g., in the proximity of tissue interfaces, in heterogeneous materials, etc. Those uncertainties can be reduced by using Monte Carlo simulations for proton dose calculations. Several Monte Carlo-based

treatment planning systems have been developed for the proton therapy, but they are not used routinely for clinical cases because Monte Carlo calculations are generally computational expensive. In the near future, Monte Carlo proton dose calculations may be used more routinely with rapid advances in computer technologies.

Both the pencil beam and Monte Carlo dose calculations use patient CT images to account for tissue heterogeneities. The pencil beam algorithms need the proton SPR distribution inside a patient for dose calculation, which is normally derived from patient treatment planning CT images according to the calibration curve linking CT numbers and SPRs. Monte Carlo dose calculations need both densities and elemental compositions to determine cross sections (Schneider *et al.*, 2000) and stopping powers. Mass densities can be easily derived from CT numbers from the CT number-to-density calibration curve. Various methods have been proposed to correlate CT numbers with elemental weights of human tissues (DeMarco *et al.*, 1998; Du Plessis *et al.*, 1998; Schneider *et al.*, 2000). In general, the range of CT numbers is divided into various bins. For each bin, a constant set of elemental composition was assigned (Jiang *et al.*, 2007).

1.1.5 Range Uncertainties

The strength of the proton radiation therapy is its capability of delivering highly conformal dose to the target while still sparing critical organs distal to the target, which is vulnerable to uncertainties (Unkelbach *et al.*, 2009). Various uncertainties exist in proton therapies, such as range uncertainties related to patient SPR estimation and tissue heterogeneities, setup uncertainties, patient motion and so on (Lomax, 2008a, b). In order to realize the full potential of proton beams, those uncertainties need to be

minimized. As one of the most important uncertainties, the range uncertainty may compromise the quality of proton treatments seriously.

Current treatment planning systems need patient SPR information to calculate water equivalent path lengths (WELs), based on which the proton range in the patient is determined. Currently, the SPR distribution inside a patient is derived from the patient's treatment planning CT images. There are two main sources of uncertainties in SPRs estimated from CT numbers: CT imaging uncertainties due to random noise or image artifacts, and the uncertainties in SPR conversion from CT numbers (Schaffner and Pedroni, 1998; Flampouri *et al.*, 2007; Jäkel and Reiss, 2007). In current clinical practice, the range uncertainties due to these two sources are accounted for by adding 3.5% of the radiological path length as a margin at the proximal and distal end of the target volume (Moyers *et al.*, 2001; Moyers *et al.*, 2009). A large margin will inevitably increase the treatment volume, resulting in higher doses to normal tissues near the target. The goal of this study is to reduce this margin by using DECT to estimate the SPR distribution in patients. The range uncertainties due to complex tissue heterogeneities can be reduced by using Monte Carlo dose calculations.

Setup uncertainties and patient motions can also degrade proton dose distributions severely. For example, a patient shift can cause a shift of dose distributions of individual beams, which may cause the overall dose distribution in the clinical target volume (CTV) to be inhomogeneous. Another example is that the WET along the beam path can change due to setup errors and/or patient motion, e.g., when a high density object such as metal inserts moves into the beam path. That may cause substantial changes in the dose distribution of a single beam. For passive-scattering proton

therapies, these uncertainties are accounted for by a method called “compensator smearing” (Urie *et al.*, 1984). For scanning beams, which do not use range compensators, new methods such as probabilistic treatment planning and beam-specific PTV (bsPTV) have been proposed to reduce the impact of those uncertainties (Unkelbach *et al.*, 2009).

1.2 CT Imaging

The CT image dataset of an object of interest is essentially a 3-dimensional representation of the object’s photon linear attenuation coefficients, which is reconstructed based on the x-ray projections of the same object from different angles. The first CT scanner was installed for clinical use in 1972 (Kalender, 2006). Since then, the CT imaging has become the most important imaging modality, which is used mainly for diagnostic purposes. In radiation therapies, patient CT images are mainly used for contouring the target and critical structures, and providing attenuation information required for dose calculations.

1.2.1 Artifacts

In CT imaging, the term ‘artifact’ is used when there are systematic differences between the measured attenuation coefficients from CT images and their true values (Barrett and Keat, 2004; Hsieh, 2003). Compared to the conventional projection imaging, the CT imaging is naturally more prone to artifacts because of its complicated reconstruction process, involving numerous independent measurements from the detector array. CT image artifacts arise from the discrepancies between the models assumed in the reconstruction algorithms and actual CT data formation process

(Williamson *et al.*, 2002). CT artifacts are usually manifested in streaking, shading, rings, and distortion. Based on the origins of artifacts, they can be grouped into four categories: physics-based artifacts, patient-based artifacts, scanner-based artifacts and reconstruction-based artifacts. The physics-based artifacts include artifacts due to beam hardening, partial volume, photon starvation, under-sampling, etc. The patient-related artifacts include artifacts due to patient motion, incomplete projections when a part of the patient falls outside the scan field of view, etc. The scanner-based artifacts include ring artifacts due to imperfect calibration of the detectors. The reconstruction-based artifacts include cone beam artifacts, stair step artifacts, zebra artifacts, etc. Among all artifacts, the distortions caused by beam hardening, partial volume and patient's motion have the largest impact to proton treatment planning, which will be introduced with more details in the following paragraphs.

Modern CT scanners normally use poly-energetic x-ray beams for scanning. The beam will become 'harder' as it penetrates through an object, because lower energy photons have higher attenuation coefficients and thus are removed from the incident beam more quickly. This effect is known as the beam hardening effect. The CT reconstruction algorithm usually does not consider the spectrum change along the beam path, which may lead to artifacts such as the so-called cupping artifact. It refers to the observation that the CT number at the periphery is higher than that at the center in CT images of a homogeneous object. As a result, the linear attenuation coefficients at the center are under-estimated, while those at the periphery are over-estimated. Dark streaking artifacts occurring between dense objects are also caused by under-estimation for similar reasons as the cupping artifacts: the beam passing through the dense objects

is harder than the one assumed in the reconstruction algorithm. The metal artifact, i.e., dark area around metal objects, is caused by such an effect as well. Various methods have been used to minimize artifacts caused by the beam hardening effect, such as extra filtration, calibration correction and software-based correction (Barrett and Keat, 2004). Metallic external filters are placed between the x-ray source and patients to remove low energy x-ray components. In addition, a shaped, so-called bowtie filter is used to harden the beam at the edge so that the beam at the edge will have comparable hardness as the beam at the center. The calibration correction involves calibrating the CT scanner with water phantoms of different diameters, in order to correct the beam hardening for body parts of different sizes. The software-based correction methods usually involve iterative reconstructions to mitigate the beam hardening in the reconstruction process. Although minimized by the correction methods, the beam hardening artifact cannot be completely removed. The beam hardening artifact is actually one major contributor to the CT imaging uncertainties and thus the range uncertainties (Moyers *et al.*, 2009).

In treatment planning CT images, the typical dimension of a CT voxel is about 1 mm (x-axis) by 1 mm (y-axis) by 2-5mm (z-axis). Partial volume averaging happens for voxels containing more than one material. For those voxels, especially the voxels containing both lung tissues and bone tissues, there exist large uncertainties in the estimated SPRs, because the tissue compositions in those voxels can be substantially different from any ‘reference’ human tissue used in the calibration process (Yang *et al.*, 2010).

Patient motion normally results in shades and streaks in CT images. Voluntary motions may be prevented by auditory instructions, while certain involuntary motions

such as heart beating cannot be avoided. Various methods have been developed to minimize motion artifacts such as cardiac gating, software corrections, etc. In addition, various 4-dimensional (4D) CT techniques have been introduced into the treatment planning process to improve the accuracy of contours and dose calculations, e.g., for thoracic cancer patients (Rietzel *et al.*, 2005; Keall *et al.*, 2005; Underberg *et al.*, 2004).

1.2.2 Dual Energy Computed Tomography (DECT)

In a DECT scan, the object of interest is scanned by two x-ray beams with different energy spectra. The x-ray beams with different energy spectra are normally generated by varying the tube voltage or external filtration. As mentioned before, CT voxel values are direct measures of photon linear attenuation coefficients, which are dominated by photoelectric interactions and Compton interactions. These two interactions vary differently with photon energy and material effective atomic numbers. Because of that, the CT voxel values of the same object measured at two different energies can be used to extract additional information of the object.

Experiments with the DECT started in the late 1970s around the time when the CT scanner was invented (Millner *et al.*, 1979; Di Chiro *et al.*, 1979; Genant and Boyd, 1977). However, the DECT did not make its way to wide clinical applications at that time, because of large uncertainties in CT numbers, low spatial resolution and long scan durations of early CT scanners (Kelcz *et al.*, 1979). In addition, x-ray tubes at that time could not provide sufficient currents at low voltage to achieve a comparable output of quanta as that at high voltage (Kelcz *et al.*, 1979). For those reasons, bone densitometry was the only dual energy application widely used. Some other useful dual energy applications, such as quantifying fat tissue (Svendsen *et al.*, 1993), detecting

calcifications in pulmonary nodules (Fraser *et al.*, 1986; Cann *et al.*, 1982) and so on, were only used occasionally. Recent advances in CT technologies and image processing tools, such as the introduction of the dual source CT scanner and the fast electronics, allowed the DECT to gain popularity in clinical applications.

The DECT modality has several clinical applications in diagnostic imaging, e.g., material decomposition (differentiation), energy-selective reconstruction, beam hardening correction, extraction of effective atomic number information, and attenuation correction in positron emission tomography (PET) (Coleman and Sinclair, 1985; Alvarez and MacOvski, 1976; Liu *et al.*, 2009; Noh *et al.*, 2009; Rutherford *et al.*, 1976). One important clinical application of the DECT is generating material-selective images from material decomposition (Primak *et al.*, 2009; Tran *et al.*, 2009; De Cecco *et al.*, 2010). The material-selective images can be used to enhance the display of vessels containing contrast material without displaying structures containing calcium, to differentiate contrast materials from other high-density material, and to differentiate body tissues without injecting contrast agents (Johnson *et al.*, 2007). There are two major decomposition methods – the image-based decomposition method and the raw data-based decomposition method (Maaß *et al.*, 2009). In the image-based decomposition method, CT images with material-selective information are determined by linear combinations of the post-reconstructed CT images (Brooks, 1977; Granton *et al.*, 2008). The raw data-based decomposition method uses a decomposition function to process the raw projection data from both CT scans into material-selective raw data first, which are then reconstructed into material-selective images (Alvarez and Seppi, 1979). The raw data-based decomposition method achieves better image quality in

general, but it requires the raw data to be matched, i.e., both x-ray beams need to go through the same path lines. This requirement may not be easily satisfied in some situations, e.g., when using a dual-source DECT scanner.

Recently, several therapy applications based on the DECT were proposed. Torikoshi *et al.* (2003) proposed to use the DECT to estimate electron density distributions in patients, which was used for treatment planning for charged-particle radiation therapies. They claimed to be able to achieve 1% accuracy in electron density estimations by using the DECT. However, their DECT utilized mono-energetic x-rays generated by a synchrotron, which is not widely available. Bazalova *et al.* (2008) suggested using additional elemental composition information from DECT scans to improve tissue segmentation, which is needed in Monte Carlo dose calculations. Williamson *et al.* (2006) proposed to use the DECT to estimate photon cross sections for brachytherapy treatment planning.

1.3 Methods of Deriving Proton Stopping Power Ratio (SPR)

1.3.1 CT Number-to-SPR Calibration Curve

In current proton clinics, patient SPR distributions are normally derived from patient treatment planning CT images based on the linear relationships between CT numbers and SPRs (Fig. 1). These linear relationships are also known as the CT number-to-SPR calibration curve, which is specific for each treatment planning CT scanner. The accuracy of the calibration curve is important to the accuracy of dose calculations.

Various methods have been proposed to determine a CT number-to-SPR calibration curve. The most straightforward method is scanning a set of tissue substitutes of known mass densities and elemental compositions and plotting their measured CT numbers against their SPRs. However, human tissue equivalent materials are not truly tissue equivalent. Schneider *et al.* (1996) from the Paul Scherrer Institute (PSI) pointed out that the calibration curves determined based on tissue substitutes are sensitive to the selection of tissue substitutes used for the calibration. They proposed a new method to solve this problem, i.e., the stoichiometric calibration method. In their method, the CT measurements of tissue substitutes are not directly used to determine the calibration curve. Instead, they are used to determine a set of CT modeling parameters first, which are then used to calculate the ‘predicted’ CT numbers of human body tissues. The calibration curve is finally determined from the ‘predicted’ CT numbers of human body tissues. Later, another group from Japan proposed a new calibration method, which is based on a poly-binary tissue model (Kanematsu *et al.*, 2003). They claimed that their new method is capable of achieving similar accuracy as the stoichiometric method but does not require complicated calculations. Currently, the calibration method used most widely in proton clinics is still the stoichiometric calibration method.

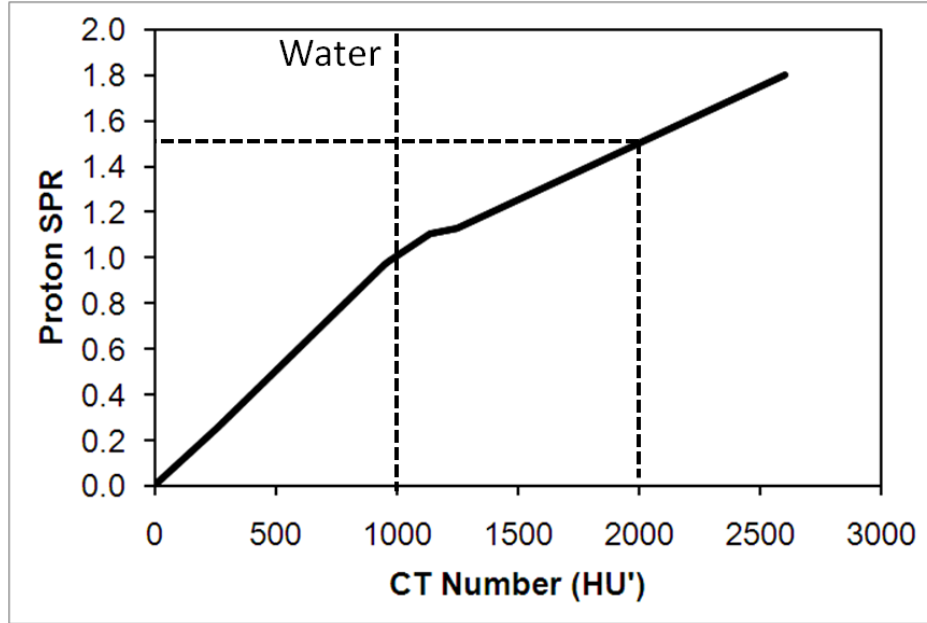


Figure 1. An example CT number-to-SPR calibration curve. The proton SPR is derived from the CT number.

1.3.2 Proton CT

Proton beams can also be used to scan patients to generate 3D images, similar to the conventional photon CT. The image voxel value is a direct measure of the proton SPR. In theory, the direct SPR measurement by proton CT should yield higher accuracy than that derived from photon CT images.

The idea of proton CT has been around for some time (Cormack, 1963, 1964; Cormack and Koehler, 1976; Hanson *et al.*, 1981), but its development is still in early phase because of the technical challenges. One major difficulty for reconstructing proton CT images is the numerous small-angle scatterings due to Coulomb interactions, which pose an inherent limit on the spatial resolution that can be achieved by proton CT (Li *et al.*, 2006). In order to reduce the blurring effect, a detecting device capable of single proton tracking is needed. Currently, there are two major collaborations actively

working on the development of proton CT: one involves several institutions in the United States such as the Santa Cruz Institute of Particle Physics (SCIPP), the Loma Linda University Medical Center (LLUMC) and the Northern Illinois University (NIU), and the other involves two Italian institutions, the University of Florence and the University of Catania. The first collaboration group is currently in the development of a prototype of proton CT capable of imaging head-size objects based on existing detectors (Talamonti *et al.*, 2010). The second collaboration group, also known as Italian PRIMA (PRoton IMAGING), is currently developing prototypes capable of carrying out two dimensional projections (Civinini *et al.*, 2010; Sipala *et al.*, 2010; Menichelli *et al.*, 2010). Another practical difficulty for proton CT now is that proton beams used in current clinics do not have energy high enough to penetrate the whole patient body.

1.4 Degeneracy Issue in the SPR Estimation

As known, the SPR and the CT number measures two different physical properties. Although both quantities are dominated by the electron density ratio (EDR), the elemental composition also matters. Because of that, there is no true one-to-one correspondence between CT numbers and the SPRs. As seen in Fig. 2, human tissues with similar CT numbers can have different SPRs. In the mean time, human tissues with different CT numbers can also have similar SPRs. Because of the degeneracy issue, there exist inherent uncertainties in SPRs estimated from a single CT number. Our preliminary study showed that the inherent uncertainty is the dominant contributing factor to the uncertainties in SPR estimation in current practice, which needs to be reduced in order to reduce the total uncertainty.

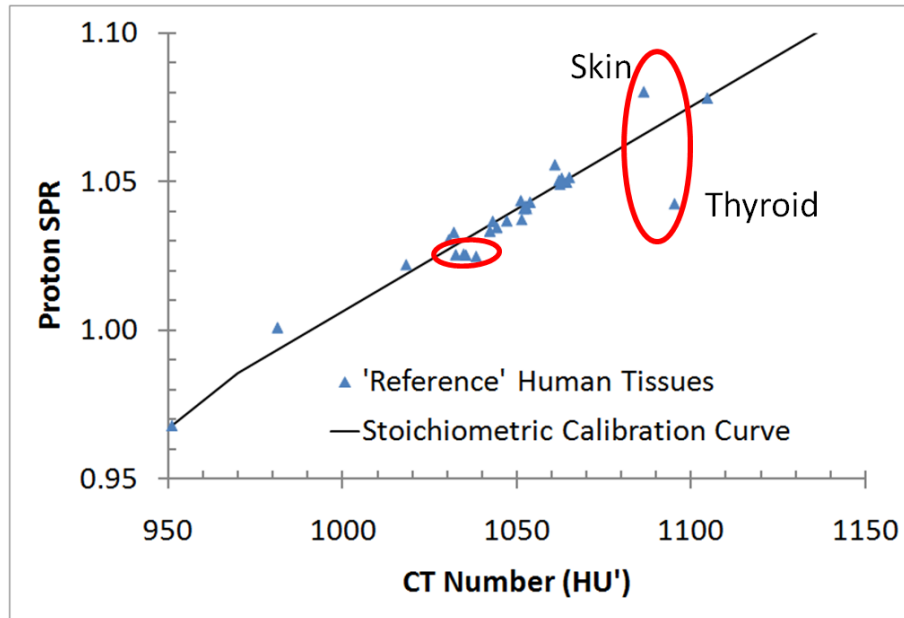


Figure 2. Demonstration of the degeneracy issue in SPR estimation based on the calibration curve. The skin and thyroid have close CT numbers but have very different SPRs. Another four human tissues (in the small red circle) have different CT numbers but have close SPRs. In either case, the uncertainties arise in SPRs estimated based on a single CT number and the calibration curve.

The degeneracy issue makes current SPR estimation method susceptible to human tissue composition variations. For example in Fig. 3, the mandible with the published density and elemental composition falls on the calibration curve perfectly, so negligible error (uncertainty) exists in its estimated SPR. However, if one mandible has a density of 5% different from the published value, it does not fall on the calibration curve any more. Thus, a non-negligible error arises in its estimated SPR. If the calcium percentage is different, a bigger difference arises. The increase of calcium percentage cause the CT number to increase substantially because of its higher atomic number (Z)

compared to other common elements in human tissues – carbon and oxygen. In the mean while, the increase of calcium percentage actually causes the SPR to decrease slightly, because calcium is slightly harder to excite compared to carbon and oxygen. But according to the calibration curve, an increase of the CT number should always lead to an increase of the stopping power, which results in a larger error. Similar patterns were observed for all human tissue types when their densities and calcium percentages are different from the published values. This shows that the accuracy of SPRs estimated from a single CT number is susceptible to the uncertainties in human tissue compositions.

In this study, we propose to use the DECT scan to estimate patient SPR distribution. We hypothesize that the SPR estimated based on both density and elemental composition information, acquired through the DECT scan, is more accurate and robust against uncertainties in human tissue composition than that derived using the conventional calibration method.

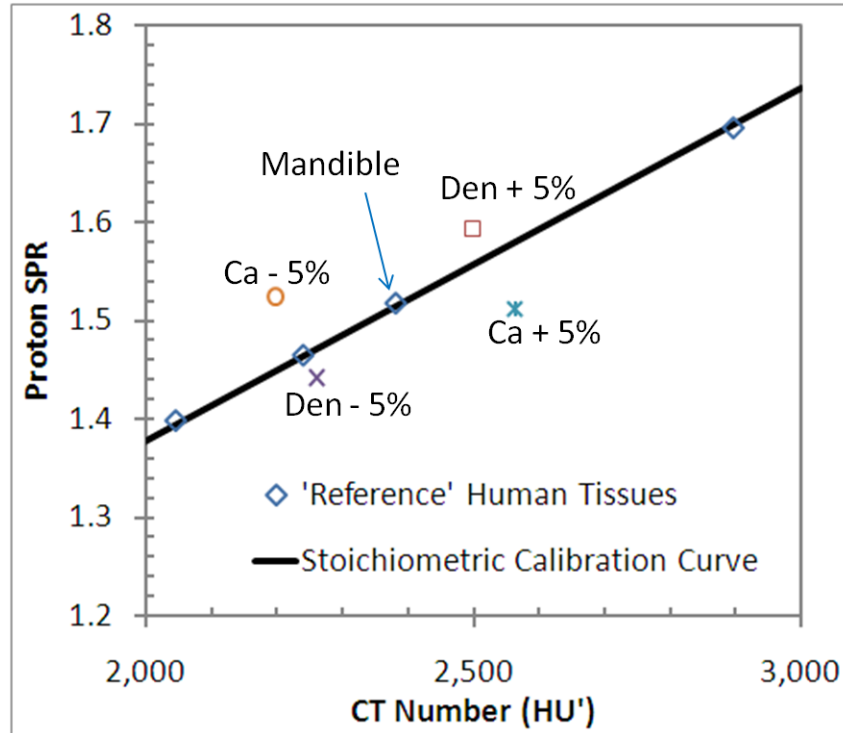


Figure 3. Demonstration of sensitivity of current SPR estimation method to human tissue composition variations. The mandible with the published density and elemental composition fall on the calibration curve perfectly, so a negligible error (uncertainty) results when estimating its SPR based on the calibration curve. But when this mandible's density or calcium percentage is changed by 5%, it deviates from the calibration curve, which causes a large error in its estimated SPR.

CHAPTER 2: HYPOTHESIS AND SPECIFIC AIMS

The hypothesis of this study is that the dual energy computed tomography can be used to derive more accurate proton stopping power ratios for human tissues than the current standard method (the stoichiometric method), and the margin to account for range uncertainties in SPRs for treatment planning can be reduced by a factor of two. This hypothesis will be tested in the following specific aims:

1. To evaluate range uncertainties related to CT imaging in current practice. This aim is necessary to establish a baseline in existing practice despite the fact that a 3.5% range uncertainty is assumed historically.
2. To develop a two-parameter model and a computational method for using the DECT scan to derive proton SPRs of human tissues. The goal of this aim is to develop a method to calculate SPRs from DECT images.
3. To develop criteria to select x-ray energy pairs for using in a DECT configuration. This is necessary in order to reduce the impact of uncertainties in CT measurements to the DECT calculation.
4. To evaluate the margin reduction by using the DECT for treatment planning. This aim is necessary to study the clinical benefit of the DECT in proton therapy and to test our hypothesis.

CHAPTER 3: SPECIFIC AIM I - ESTIMATION OF RANGE UNCERTAINTIES (SPR-RELATED) IN CURRENT PRACTICE

3.1 Introduction

Specific Aim I: Evaluation of range uncertainties related to SPR estimation in current practice

This specific aim is necessary to establish the baseline data for uncertainties encountered in existing practice despite the fact that a 3.5% range uncertainty is assumed historically. One major innovation in our estimation is that the uncertainty estimates were determined for different tissue groups separately, i.e., lung tissues, soft tissues, and bone tissues. Another innovation is that the uncertainties related to human tissue composition variations were estimated in our study.

This chapter starts with a detailed description of the stoichiometric calibration method and its key elements – the modeling of treatment planning CT scanners and the calculation of proton SPRs of human body tissues using the Bethe-Bloch equation. The equipments and tissue composition data from the literature, used to determine the calibration curve in this study, are also described. Then our methods of categorizing and estimating the uncertainties in current practice, and combining the uncertainties associated with each tissue group to a composite range uncertainty are explained in detail. Lastly, our estimates of the uncertainties in current SPR estimation are presented,

followed by a discussion to compare our estimates with the estimates made by other groups and the possible measures to mitigate the composite range uncertainty in current practice.

3.2 Methods and Materials

3.2.1 Terminology

A few terms, which are used frequently in this study but may be confusing, are defined here for clarification. In general, if the value of a quantity is derived indirectly using the stoichiometric method or the DECT method, its value is termed as the ‘estimated’ value. Meanwhile, if the value is calculated directly based on the elemental composition information, it is termed as the ‘true’ or ‘theoretical’ value. A few important examples are listed below.

- **‘True’ or ‘Theoretical’ CT number:** the CT number calculated directly based on the elemental composition information and the x-ray spectrum according to the CT number definition (Eq. 6)
- **‘Predicted’ CT number:** the CT number calculated based on the specific parameter set used in either the stoichiometric method or the DECT method for CT modeling.
- **‘True’ SPR:** the SPR calculated directly based on the elemental composition using the Bethe-Bloch equation (Eq. 10).
- **‘Estimated’ SPR:** the SPR derived from the CT number(s) by using either the stoichiometric method or the DECT method.

3.2.2 Stoichiometric Calibration Method

The stoichiometric calibration procedure (Schneider *et al.*, 1996) consists of four major steps:

- 1) Acquire images of several tissue substitutes of known densities and elemental compositions using a treatment planning CT scanner.
- 2) Model the treatment planning CT scanner by calculating scanner specific parameters (K^{ph} , K^{coh} , and K^{KN}) based on CT measurements of the tissue substitutes in step one.
- 3) Predict CT numbers of various human body tissue types based on the parameters determined in step two.
- 4) Determine the calibration curve by linear regression fit within each tissue group and connect them piecewise.

3.2.2.1 Determination of CT Scanner Specific Parameters

The key step in the stoichiometric calibration procedure is the second step – modeling the CT scanner. The CT number (Hounsfield unit or *HU*) yielded by a CT scan is essentially a measure of the photon linear attenuation coefficient, and is defined as

$$HU = \frac{\langle \mu_x \rangle - \langle \mu_{\text{water}} \rangle}{\langle \mu_{\text{water}} \rangle} \times 1000 \quad , \quad (1)$$

where $\langle \mu_x \rangle$ and $\langle \mu_{\text{water}} \rangle$ are the photon linear attenuation coefficients averaged over the x-ray spectrum of the object of interest and water, respectively. The following CT number definition was used in this study for convenience:

$$HU' = \frac{\langle \mu_x \rangle}{\langle \mu_{\text{water}} \rangle} * 1000 \quad . \quad (2)$$

In this way, $\frac{dHU'}{HU'} = \frac{d\langle\mu_x\rangle}{\langle\mu_x\rangle}$.

The photon linear attenuation coefficient ($\langle\mu_x\rangle$) of a composite material for a poly-energetic x-ray beam with peak energy below 1.02 MeV can be expressed as

$$\langle\mu_x\rangle = \rho_e (K^{\text{ph}} \tilde{Z}^{3.62} + K^{\text{coh}} \hat{Z}^{1.86} + K^{\text{KN}}) \quad , \quad (3)$$

where K^{ph} , K^{coh} and K^{KN} are constants describing the photoelectric interaction, coherent scattering, and Compton scattering, respectively. ρ_e is the electron density which can be calculated by

$$\rho_e = \rho * N_A * \sum_{i=1}^N \frac{Z_i \omega_i}{A_i} \quad , \quad (4)$$

where Z_i , A_i , ω_i , N_A and N are the atomic number, atomic weight, relative weight (by mass) of the i_{th} element, Avogadro's number, and the number of elements in the composite material, respectively. \tilde{Z} and \hat{Z} are the effective atomic numbers of the composite material which are defined as

$$\begin{aligned} \tilde{Z} &= \left[\sum_{i=1}^N \frac{Z_i \omega_i}{A_i} * Z_i^{3.62} \right]^{1/3.62} \\ \hat{Z} &= \left[\sum_{i=1}^N \frac{Z_i \omega_i}{A_i} * Z_i^{1.86} \right]^{1/1.86} \end{aligned} \quad . \quad (5)$$

After substituting $\langle\mu_x\rangle$ and $\langle\mu_{\text{water}}\rangle$ with Eq. 3, Eq. 2 becomes

$$HU' = \rho'_e (K^{\text{ph}'} \tilde{Z}^{3.62} + K^{\text{coh}'} \hat{Z}^{1.86} + K^{\text{KN}'}) * 1000 \quad , \quad (6)$$

where $\rho'_e = \frac{\rho_e}{\rho_{\text{e,water}}}$, $K^{\text{ph}'} = \frac{K^{\text{ph}}}{C_{\text{water}}}$, $K^{\text{coh}'} = \frac{K^{\text{coh}}}{C_{\text{water}}}$, $K^{\text{KN}'} = \frac{K^{\text{KN}}}{C_{\text{water}}}$, and $C_{\text{water}} =$

$(K^{\text{ph}} \tilde{Z}_{\text{water}}^{3.62} + K^{\text{coh}} \hat{Z}_{\text{water}}^{1.86} + K^{\text{KN}})$. $\rho_{\text{e,water}}$ is the electron density of water.

According to Eq. 6, the measured CT number (HU') is a function of six variables. Three of them (ρ'_e , $\tilde{Z}^{3.62}$, and $\hat{Z}^{1.86}$) are only related to the object of interest, and can be calculated when the object's elemental composition is known. The other three variables ($K^{\text{ph}'}$, $K^{\text{coh}'}$, and $K^{\text{KN}'}$) are only related to the CT scanner, and can be determined by linear regression fit when more than three tissue substitutes of known elemental compositions are scanned. With those three scanner specific parameters known, the CT numbers of human body tissues can be calculated using Eq. 6.

3.2.2.2 *Bethe-Bloch Equation*

Another key step is to determine the SPRs for human body tissues. It is impractical to prepare samples of all human tissue types and measure their SPRs directly. Therefore, the SPRs of human body tissues that are used in current practice for calibration are normally calculated using the Bethe-Bloch equation.

The stopping power (ρ_s) of a moderately relativistic proton is well-described by the Bethe-Bloch equation

$$\rho_s = K\rho \frac{Z}{A} \frac{1}{\beta^2} \left[\frac{1}{2} \ln \frac{2m_e c^2 \beta^2 T_{\text{max}}}{1 - \beta^2} - \beta^2 - \ln I_m - \frac{\delta(\beta\gamma)}{2} \right], \quad (7)$$

where ρ , Z , A and I_m are the density, atomic number, atomic mass and mean excitation energy of the absorber, respectively (Nakamura, 2010; ICRU, 1993). β is the velocity of the incident proton relative to the velocity of light, and m_e is the mass of the electron. $K = 4\pi N_A r_e^2 m_e c^2 = 0.307 \text{ MeV g}^{-1} \text{cm}^2$, where r_e is the classical electron radius. T_{max} is the maximal kinetic energy that can be transferred to a single electron in a single collision, which is given by

$$T_{\max} = \frac{2m_e c^2 \beta^2 \gamma^2}{1 + \frac{2\gamma m_e}{M} + \left(\frac{m_e}{M}\right)^2} , \quad (8)$$

where $\gamma = (1 - \beta^2)^{-1/2}$ and M is the mass of the proton. At the University of Texas MD Anderson Cancer Center (UTMDACC) Proton Therapy Center (PTC), the maximal proton energy is 250 MeV. For protons with energy lower than 250 MeV, $T_{\max} \approx 0.9987 \times 2m_e c^2 \beta^2 \gamma^2 \approx 2m_e c^2 \beta^2 \gamma^2$. The term $\frac{\delta(\beta\gamma)}{2}$ is the ‘density correction’ to the ionization energy loss due to the shielding of remote electrons by close electrons, which is approximately zero for the proton energies considered in this study.

After ignoring the ‘density correction’ term and plugging $T_{\max} \approx 2m_e c^2 \beta^2 \gamma^2$ back into Eq. 7, the proton stopping power is approximately equal to

$$\rho_s = K\rho \frac{Z}{A} \frac{1}{\beta^2} \left[\ln \frac{2m_e c^2 \beta^2}{1 - \beta^2} - \beta^2 - \ln I_m \right] . \quad (9)$$

For protons with energy beyond 100 MeV, the difference between the stopping power of water calculated using the original form (Eq. 7) and the one calculated using the simplified form (Eq. 9) is well below 0.1%, justifying our stopping power calculation using the simplified form. Based on Eq. 9, the proton SPR of a material relative to water is defined as

$$\rho'_s = \frac{\rho_{s,x}}{\rho_{s,\text{water}}} = \rho'_e \times \frac{\ln \frac{2m_e c^2 \beta^2}{1 - \beta^2} - \beta^2 - \ln I_{m,x}}{\ln \frac{2m_e c^2 \beta^2}{1 - \beta^2} - \beta^2 - \ln I_{m,\text{water}}} , \quad (10)$$

where ρ'_e is the EDR of the object of interest relative to water.

The SPRs calculated using Eq. 10 based on the elemental composition information are referred to as “true” SPRs, while the SPRs derived from CT numbers

using either the stoichiometric calibration method or the DECT method are referred to as “estimated” SPRs. The relative error in the estimated SPR is defined as

$$Relative\ Error\ (\%) = \frac{Est.\ SPR - True\ SPR}{True\ SPR} \times 100\% \quad . \quad (11)$$

The root-mean-square (RMS) error is defined as

$$RMS\ Error\ (\%) = \sqrt{\frac{\sum_{i=1}^N \left(\frac{Est.\ SPR_i - True\ SPR_i}{True\ SPR_i} \right)^2}{N}} \times 100\% \quad , \quad (12)$$

where N is the number of samples.

3.2.2.3 *Our Calibration*

The tissue substitutes chosen in our stoichiometric calibration were adipose tissue (AP6), solid water, brain (SR2), liver (LV1), water, B200, CB2-30%, CB2-50% and cortical bone (SB3) (Table 1), which are all from the RMI 467 tissue characterization phantom (Gammex, Middleton, WI). CT measurements of the same object may vary strongly with scanning conditions because of the beam hardening effect. To be consistent in our calibration, one insert was scanned a time and it was always located at the center of the phantom during the scan. In addition, to account for the patient size effect, the calibration curves were determined for two phantom sizes (head- and body-size), and the average calibration curve of the two was used for patient SPR estimation. The diameters of the head- and body-size calibration phantoms are 16 cm and 32 cm, respectively, and both phantoms are made of acrylic. The images of the RMI 467 phantom and the head- and body-size calibration phantoms are shown in Fig. 4.

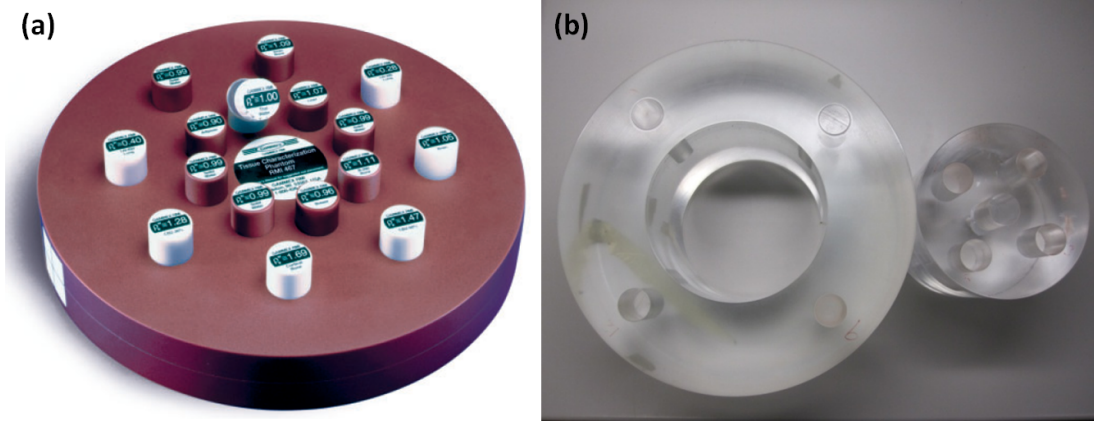


Figure 4. Images of (a) the RMI 467 tissue characterization phantom and (b) the head- and body-size calibration phantoms.

41 types of human body tissues were chosen in our stoichiometric calibration. Table 2 lists their densities and elemental compositions recommended in the literature (Woodard and White, 1982, 1986; White *et al.*, 1987; White *et al.*, 1991; ICRU, 1989). The human body tissues with the recommended values of densities and elemental compositions are referred to as ‘reference’ human body tissues in this study. The ‘reference’ human body tissues listed in Table 2 were divided into three tissue groups – lung tissues, soft tissues, and bone tissues. The lung tissue group consists of just one tissue – lung (inflated). The soft tissue group consists of 29 body tissues that do not contain a substantial amount of calcium ($>1\%$), while the bone tissue group consist of 11 body tissues that contain a substantial amount of calcium.

The stoichiometric calibration was performed on the treatment planning CT scanner (ACB CT1) at the UTMDACC. Figure 5 shows the calibration curves determined for ACB CT1 for different phantom sizes.

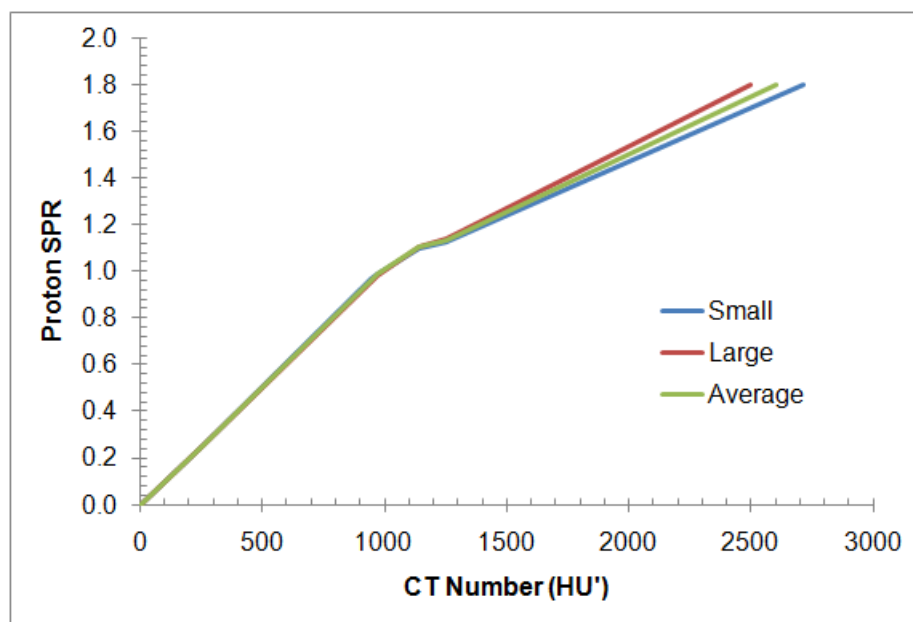


Figure 5. Stoichiometric calibration curves determined for the kV scanner (ACB CT1).

Table 1. Recommended elemental compositions and densities (ρ) of air, water and human tissue substitutes provided with the RMI 467 phantom.

	H	C	N	O	Mg	Si	P	Cl	Ar	Ca	ρ (g/cm ³)
Atomic Number (Z)	1	6	7	8	12	14	15	17	18	20	
Atomic Weight (A)	1.008	12.01	14.01	16.00	24.31	28.09	30.97	35.45	39.95	40.08	
Tissue Substitutes	Elemental Compositions (percentage by mass)										
Air	0.0	0.02	75.5	23.19	0.0	0.0	0.0	0.0	1.3	0.0	0.001
Lung (LN300)	8.5	59.3	2.0	18.1	11.2	0.8	0.0	0.1	0.0	0.0	0.3
Lung(LN450)	8.5	59.5	2.0	18.1	11.2	0.6	0.0	0.1	0.0	0.0	0.45
Solid Water	8.1	67.2	2.4	19.8	0.0	0.0	0.0	0.1	0.0	2.3	1.12
SR2 Brain	10.8	72.5	1.7	14.9	0.0	0.0	0.0	0.1	0.0	0.0	0.99
IB1, Inner Bone	7.9	63.8	4.2	9.9	0.0	0.0	0.0	14.2	0.0	0.0	1.015
AP6 Adipose	9.1	72.2	2.3	16.3	0.0	0.0	0.0	0.1	0.0	0.0	1.049
Breast	8.7	70.0	2.4	17.9	0.0	0.0	0.0	0.1	0.0	1.0	0.92
Liver	11.0	4.1	1.2	82.5	0.0	0.0	0.0	1.2	0.0	0.0	1.08
Water	11.2	0.0	0.0	88.8	0.0	0.0	0.0	0.0	0.0	0.0	1.0
B200 Bone Mineral	6.6	55.6	2.0	23.6	0.0	0.0	3.2	0.1	0.0	8.9	1.145
CB2-30% CaCO3	6.7	53.5	2.1	25.6	0.0	0.0	0.0	0.1	0.0	12.0	1.34
CB2-50% CaCO3	4.8	41.6	1.5	32.0	0.0	0.0	0.0	0.1	0.0	20.0	1.56
SB3 Bone Cortical	3.4	31.4	1.8	36.5	0.0	0.0	0.0	0.0	0.0	26.8	1.819

Table 2. Recommended elemental compositions and densities (ρ) of human body tissues from the literature.

	H	C	N	O	Na	Mg	P	S	Cl	K	Ca	Fe	I	ρ (g/cm ³)
Atomic Number (Z)	1	6	7	8	11	12	15	16	17	19	20	26	53	
Atomic Weight (A)	1.008	12.01	14.01	16.00	22.99	24.31	30.97	32.06	35.45	39.10	40.08	55.85	126.90	
Human Body Tissues	Elemental Composition (percentage by mass)													

Lung (inflated)	10.3	10.5	3.1	74.9	0.2	0.0	0.2	0.3	0.3	0.2	0.0	0.0	0.0	0.26
Adipose tissue	11.4	59.8	0.7	27.8	0.1	0.0	0.0	0.1	0.1	0.0	0.0	0.0	0.0	0.95
Adrenal gland	10.6	28.4	2.6	57.8	0.0	0.0	0.1	0.2	0.2	0.1	0.0	0.0	0.0	1.03
Aorta	9.9	14.7	4.2	69.8	0.2	0.0	0.4	0.3	0.0	0.1	0.4	0.0	0.0	1.05
Bladder – filled	10.8	3.5	1.5	83.0	0.3	0.0	0.1	0.1	0.5	0.2	0.0	0.0	0.0	1.03
Blood (whole) (erythrocytes/plasma 44:56, by mass)	10.2	11.0	3.3	74.5	0.1	0.0	0.1	0.2	0.3	0.2	0.0	0.1	0.0	1.06
Brain (grey/white matter 50:50, by mass)	10.7	14.5	2.2	71.2	0.2	0.0	0.4	0.2	0.3	0.3	0.0	0.0	0.0	1.04
Breast (mammary gland)	10.6	33.2	3.0	52.7	0.1	0.0	0.1	0.2	0.1	0.0	0.0	0.0	0.0	1.02
Connective Tissue	9.4	20.7	6.2	62.2	0.6	0.0	0.0	0.6	0.3	0.0	0.0	0.0	0.0	1.12
Eye lens	9.6	19.5	5.7	64.6	0.1	0.0	0.1	0.3	0.1	0.0	0.0	0.0	0.0	1.07
Gallbladder – Bile	10.8	6.1	0.1	82.2	0.4	0.0	0.0	0.0	0.4	0.0	0.0	0.0	0.0	1.03
GI tract (intestine)	10.6	11.5	2.2	75.1	0.1	0.0	0.1	0.1	0.2	0.1	0.0	0.0	0.0	1.03
Heart (blood filled)	10.3	12.1	3.2	73.4	0.1	0.0	0.1	0.2	0.3	0.2	0.0	0.1	0.0	1.06
Kidney	10.3	13.2	3.0	72.4	0.2	0.0	0.2	0.2	0.2	0.2	0.1	0.0	0.0	1.05
Liver	10.2	13.9	3.0	71.6	0.2	0.0	0.3	0.3	0.2	0.3	0.0	0.0	0.0	1.06
Lung (deflated)	10.3	10.5	3.1	74.9	0.2	0.0	0.2	0.3	0.3	0.2	0.0	0.0	0.0	1.05
Lymph	10.8	4.1	1.1	83.2	0.3	0.0	0.0	0.1	0.4	0.0	0.0	0.0	0.0	1.03
Muscle (skeletal)	10.2	14.3	3.4	71.0	0.1	0.0	0.2	0.3	0.1	0.4	0.0	0.0	0.0	1.05
Ovary	10.5	9.3	2.4	76.8	0.2	0.0	0.2	0.2	0.2	0.2	0.0	0.0	0.0	1.05
Pancreas	10.6	16.9	2.2	69.4	0.2	0.0	0.2	0.1	0.2	0.2	0.0	0.0	0.0	1.04
Prostate	10.5	8.9	2.5	77.4	0.2	0.0	0.1	0.2	0.0	0.2	0.0	0.0	0.0	1.04
Skin	10.0	20.4	4.2	64.5	0.2	0.0	0.1	0.2	0.3	0.1	0.0	0.0	0.0	1.09
Spleen	10.3	11.3	3.2	74.1	0.1	0.0	0.3	0.2	0.2	0.3	0.0	0.0	0.0	1.06
Stomach	10.4	13.9	2.9	72.1	0.1	0.0	0.1	0.2	0.1	0.2	0.0	0.0	0.0	1.05
Testis	10.6	9.9	2.0	76.6	0.2	0.0	0.1	0.2	0.2	0.2	0.0	0.0	0.0	1.04
Thyroid	10.4	11.9	2.4	74.5	0.2	0.0	0.1	0.1	0.2	0.1	0.0	0.0	0.1	1.05
Trachea	10.1	13.9	3.3	71.3	0.1	0.0	0.4	0.4	0.1	0.4	0.0	0.0	0.0	1.06
Skeleton-Red Marrow	10.5	41.4	3.4	43.9	0.0	0.0	0.1	0.2	0.2	0.2	0.0	0.1	0.0	1.03

Skeleton-Yellow marrow	11.5	64.4	0.7	23.1	0.1	0.0	0.0	0.1	0.1	0.0	0.0	0.0	0.0	0.98
Skeleton-Cartilag	9.6	9.9	2.2	74.4	0.5	0.0	2.2	0.9	0.3	0.0	0.0	0.0	0.0	1.10
Skeleton-Cortical bone	3.4	15.5	4.2	43.5	0.1	0.2	10.3	0.3	0.0	0.0	22.5	0.0	0.0	1.92
Skeleton-Spongiosa	8.5	40.4	2.8	36.7	0.1	0.1	3.4	0.2	0.2	0.1	7.4	0.1	0.0	1.18
Skeleton-Cranium	5.0	21.2	4.0	43.5	0.1	0.2	8.1	0.3	0.0	0.0	17.6	0.0	0.0	1.61
Skeleton-Femur	7.0	34.5	2.8	36.8	0.1	0.1	5.5	0.2	0.1	0.0	12.9	0.0	0.0	1.33
Skeleton-Humerus	6.0	31.4	3.1	36.9	0.1	0.1	7.0	0.2	0.0	0.0	15.2	0.0	0.0	1.46
Skeleton-Mandible	4.6	19.9	4.1	43.5	0.1	0.2	8.6	0.3	0.0	0.0	18.7	0.0	0.0	1.68
Skeleton-Ribs (2nd,6th)	6.4	26.3	3.9	43.6	0.1	0.1	6.0	0.3	0.1	0.1	13.1	0.0	0.0	1.41
Skeleton-Ribs (10th)	5.6	23.5	4.0	43.4	0.1	0.1	7.2	0.3	0.1	0.1	15.6	0.0	0.0	1.52
Skeleton-Sacrum	7.4	30.2	3.7	43.8	0.0	0.1	4.5	0.2	0.1	0.1	9.8	0.1	0.0	1.29
Skeleton-Vertebral column (C4)	6.3	26.1	3.9	43.6	0.1	0.1	6.1	0.3	0.1	0.1	13.3	0.0	0.0	1.42
Skeleton-Vertebra column (D6,L3)	7.0	28.7	3.8	43.7	0.0	0.1	5.1	0.2	0.1	0.1	11.1	0.1	0.0	1.33

3.2.3 Uncertainties in SPR Estimation

We found that the uncertainties in SPR estimation using the stoichiometric calibration method can be divided into three major categories. The first major category is the inherent uncertainty due to the inherent flaw of the current calibration method, estimating the SPR from a single CT number. The calibration curve is determined by linear regression fit of the ‘reference’ human body tissues. Figure 6 shows a zoomed-in version of the calibration curve overlaid with the ‘reference’ human body tissues. Clearly seen in Fig. 6, the fitting between the human tissue data points and the calibration curve is not perfect because the CT number and the SPR relate to different physical properties. Both quantities are linearly proportional to EDRs. But the CT number also depends on the cross sections of various photon interactions, among which the photoelectric interaction is approximately proportional to Z^3 , while the SPR also depends on the mean excitation energy which only changes with Z slightly. Therefore, there is no ‘perfect’ linear correspondence between CT numbers and SPRs of human tissues, which results in the inherent uncertainties (or residue error) when estimating the SPR from a single CT number based on a linear calibration curve (Fig. 6).

The other two major categories are the uncertainties in calculated CT numbers and the uncertainties in calculated SPRs. The stoichiometric calibration curve is determined based on CT numbers and SPRs of human body tissues, which are all calculated instead of measured. The potential differences between the calculated values and their measured counterparts cause uncertainties.

The uncertainties in calculated CT numbers can be divided further into two independent sources of uncertainties: the difference between the predicted CT number

and the measured CT number at the reference condition, and the difference between the CT numbers measured at the reference condition and at a non-reference condition. The first category of uncertainties in predicted CT numbers is caused by the ‘imperfectness’ of CT modeling, while the second category is caused by CT number variation with scanning conditions, largely due to the beam hardening effect. These two categories of uncertainties are referred to as modeling error in predicted CT numbers and CT imaging uncertainty.

There are also two major sources of uncertainties when calculating SPRs of human tissues using the Bethe-Bloch equation: the uncertainties in mean excitation energies of human tissues and water, and the uncertainties due to SPR variations with proton energy. The details of how the uncertainties of each category were estimated will be shown in the following sections.

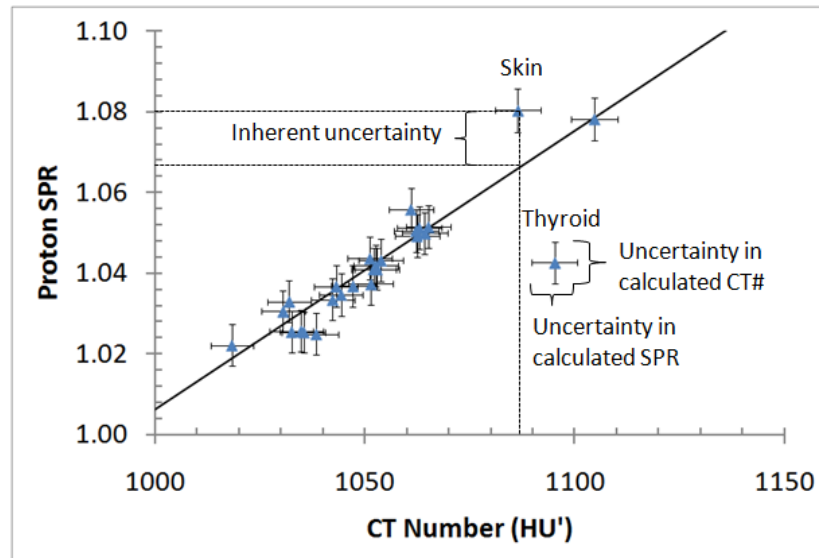


Figure 6. Illustration of uncertainties in proton SPRs estimated using the stoichiometric calibration method. The blue triangles represent ‘reference’ human body tissues and the black solid line represents the stoichiometric calibration curve. The first category of uncertainties is

the inherent uncertainty caused by the differences between the calculated SPRs and the SPRs derived based on the calibration curve. The other two categories of uncertainties are the uncertainties in the calculation of CT numbers and SPRs for the ‘reference’ human body tissues.

3.2.3.1 *Inherent Uncertainties*

It was straightforward to estimate the inherent uncertainties by comparing the SPRs calculated using the Bethe-Bloch equation and the ones derived from the predicted CT numbers. The predicted CT numbers can be calculated using Eq. 6 based on the scanner specific parameters ($K^{\text{ph'}}$, $K^{\text{coh'}}$, and $K^{\text{KN'}}$) determined in the calibration process. In this study, the inherent uncertainties were estimated for not only ‘reference’ human tissues, but also ‘individualized’ human tissues. The ‘individualized’ human tissues were generated from the ‘reference’ human tissues by introducing variations to the recommended tissue compositions. Our previous study (Appendix A) showed that uncertainties exist in the recommended tissue compositions of the ‘reference’ human tissues, and that the inherent uncertainties increase substantially in the presence of tissue composition variations. Therefore, it was necessary to consider the uncertainties in the recommended tissue composition when estimating the inherent uncertainties.

We found that there exist two categories of uncertainties in the recommended tissue compositions of the ‘reference’ human body tissues (Table 2). The first is a possible systematic uncertainty of the given values. The recommended values are supposed to represent the population average. In reality, they may deviate from the true population average due to a variety of reasons such as a biased sample, a flawed measurement method, etc. The second is a statistical uncertainty caused by individual

patient-to-patient variation. ICRU Report No. 44 (1989) states explicitly that “the elemental compositions of most body tissues are known to vary considerably between individuals of the same age” and that “the composition of a given tissue within one individual may vary from one body site to another.”

A population of 'individualized' human tissues was generated for each 'reference' human tissue type. The 'reference' human tissue was used as a template: all quantities of the 'individualized' human tissues were kept the same as the corresponding 'reference' human tissue except for key factors. The key factors were found to be the density, the percentage of hydrogen for soft tissues, and the percentage of calcium for bone tissues. To simulate individual (statistical) variations, the values of the key factors were determined by drawing random numbers from a Gaussian distribution. To account for the systematic uncertainty, a small difference was introduced between the mean of the Gaussian distribution and the original value of the key factor. The densities of 'individualized' human tissues were determined from a Gaussian distribution $\sim N(\mu', \sigma')$, where μ' and σ' are the mean and standard deviation, respectively. $\mu' = \mu * (1 \pm \delta)$, where μ and δ are the density of the corresponding 'reference' human tissue template and the relative systematic uncertainty, respectively. $\sigma' = \mu * \sigma$, where σ is the relative statistical uncertainty. The percentages of key elements of the 'individualized' human tissues were determined from a Gaussian distribution with μ' and σ' equal to $\mu \pm \delta$ and σ , respectively, where μ is the percentage of the 'reference' human tissue template, and δ and σ are the systematic uncertainty and statistical uncertainty, respectively. Table 3 lists the values of δ and σ in this study. These values were determined through a thorough literature search, which is described in detail in

Appendix A. 2000 ‘individualized’ human tissues were generated for each tissue type in this study.

Table 3. Summary of the systematic uncertainty (δ) and statistical uncertainty (σ) in the recommended values of the ‘reference’ human tissues.

	Systematic Uncertainty (δ)	Statistical (Individual) Uncertainty (σ)
Density	2.1%	1.7%
H (%)	0.2%	0.5%
Ca (%)	1%	1%

3.2.3.2 *Modeling Errors in Predicted CT Numbers*

It was difficult to directly estimate the possible differences between the predicted and measured CT numbers for human body tissues. Therefore, we chose to estimate the modeling errors based on the data of tissue substitutes. We scanned a set of tissue substitutes of known elemental compositions. Their measured CT numbers were then compared with the CT numbers predicted based on the model. Because the model for predicting CT numbers should work for both human tissues and tissues substitutes, the uncertainty estimates based on tissues substitutes were considered to be equivalent to those based on human tissues.

3.2.3.3 *CT Imaging Uncertainties*

There are various factors that can cause CT number variations. In this study, general factors such as time, scanner, patient size, position in the scan, surrounding objects, and a special factor – the object outside field-of-view (FOV) – were considered.

Although modern CT scanners are stable, CT measurements of the same object under the same conditions by the same CT scanner may still vary from time to time, due to random noise or systematic problems. In addition to that, CT measurements of the

same object may differ when using different CT scanners, especially scanners made by different manufactures. In this study, CT number variations with time and scanner were estimated based on the monthly quality assurance (QA) data of different treatment planning CT scanners. During monthly QAs, the same set of tissue substitutes is scanned for each scanner. Therefore, monthly CT QA data provides a perfect reference of CT number variations with time and scanner.

CT number variations with patient size were estimated by scanning the same material insert in the head phantom and the body phantom, respectively (Fig. 7). The material insert was always located at the center so the size of the phantom was the only differing parameter.

CT number variations with the position in the scan were estimated by scanning the same material insert at the center and at the periphery of the body phantom, respectively (Fig. 8). The body phantom was selected because it offered larger position differences.

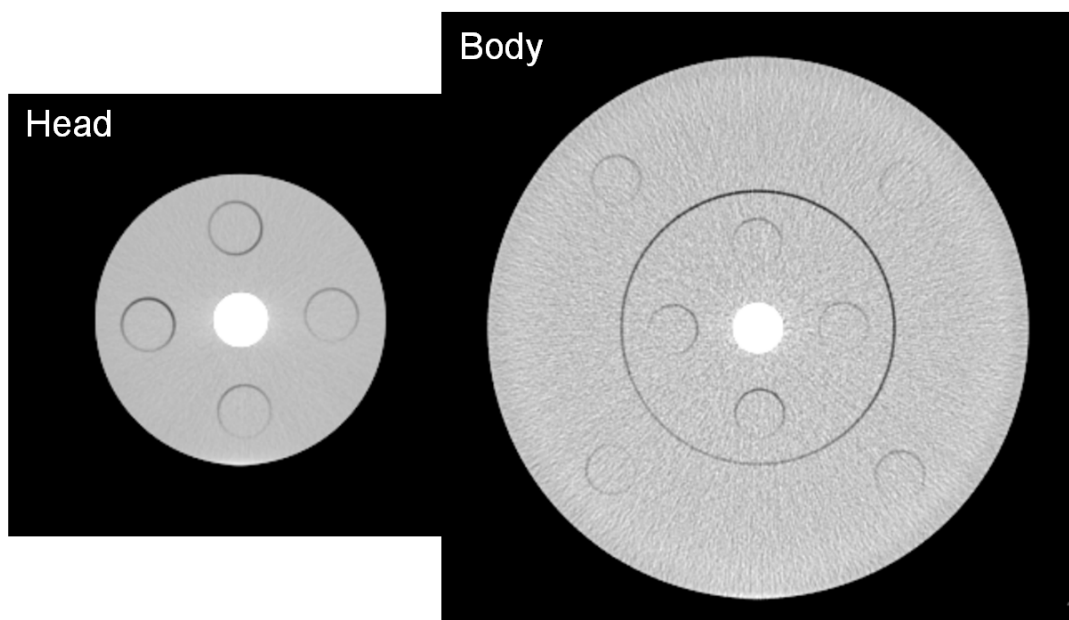


Figure 7. Axial CT images of the head phantom and the body phantom with the same tissue substitute insert at the center.

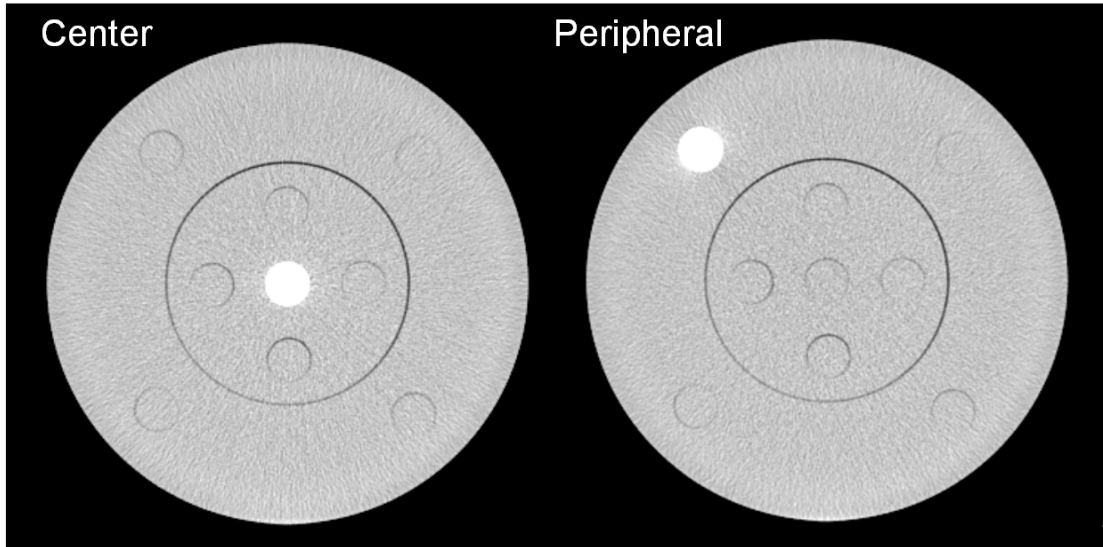


Figure 8. Axial CT images of the body phantom with the same tissue insert at the center and at the periphery.

CT number variations with different objects in the surrounding area were estimated by placing different tissue substitutes at the periphery of the body phantom and measuring CT numbers of solid water inserts at other locations. CT number variations caused by the objects outside the FOV were estimated by scanning the RMI 467 phantom with the same distribution of material inserts with and without a particular material insert of choice outside the FOV, respectively. One special object that can be outside the FOV is the couch of the CT scanner. In order to study the impact of the couch position, the RMI 467 phantom of the same distribution of tissue substitutes were scanned at two different couch positions: the couch inside the FOV and the couch outside the FOV (Fig. 9).

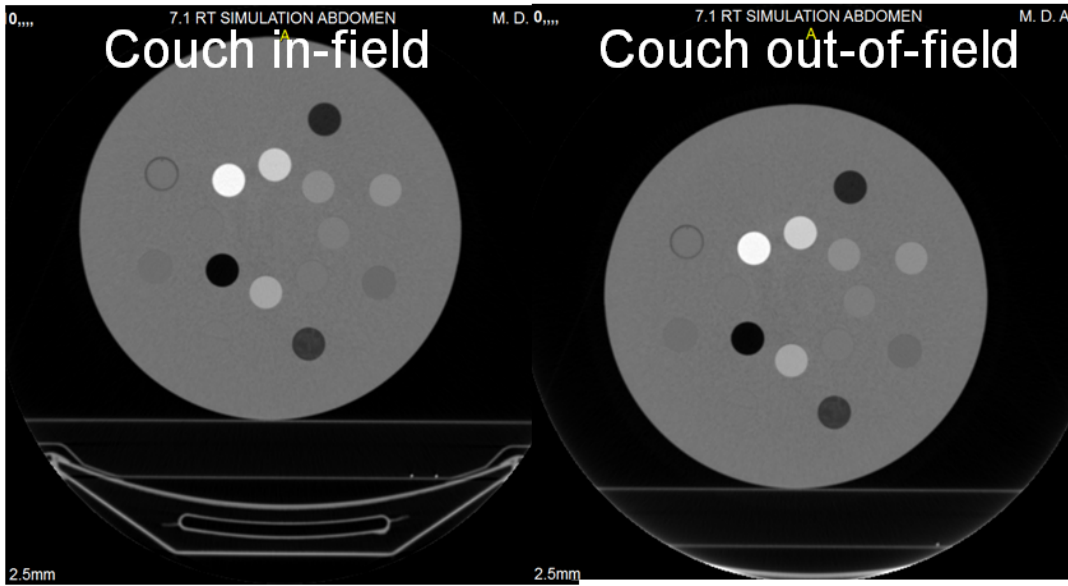


Figure 9. Axial CT images of the RMI 467 phantom with two different couch positions: one inside the FOV and one outside the FOV.

In addition, we found that relative CT number variations do not translate into the same amount of relative SPR variations because of the slope of the calibration curve. The calibration curve relates SPRs and CT numbers essentially by a linear relationship, $\rho'_s = a * HU' + b$, where a and b are the slope and the residue of the calibration curve. By taking the first derivative, the relative SPR variation is related to the relative CT number variation by

$$\frac{d\rho'_s}{\rho'_s} = \frac{dHU'}{HU'} * \frac{HU'}{HU' + b/a} \quad (13)$$

The variation ratio, $\frac{HU'}{HU' + b/a}$, was calculated for all tissue substitutes used to measure CT imaging uncertainties (Table 4).

Table 4. Variation ratios calculated for tissue substitutes used to measure CT imaging uncertainties.

Tissue Substitutes	Ratio
LN-300	1.03
LN-450	1.02
Adipose	0.91
Breast	0.68
Solid Water	0.69
Brain	0.69
Liver	0.70
Water	0.69
Inner Bone	0.54
B-200	0.55
CB2-30%	0.59
CB2-50%	0.64
Cortical Bone	0.69

3.2.3.4 *Uncertainties in Mean Excitation Energies*

It is not a trivial task to determine the mean excitation energy for a material. Even for water, there are several different values suggested based on experiments in the literature – 67eV, 75 eV, 78 eV and 80 eV (ICRU, 2005; Paul *et al.*, 2007; ICRU, 1993; Kumazaki *et al.*, 2007; Emfietzoglou *et al.*, 2009; Bischel and Hiraoka, 1992). The variation of this value causes up to 1% uncertainty in the calculated stopping power of water. The mean excitation energies of human body tissues from the literature are likely to carry larger uncertainties than that of water, because they were mostly determined by calculations using the Bragg additivity rule (ICRU, 1993; Seltzer and Berger, 1982) instead of direct measurements like water. If the mean excitation energies of human body tissues vary by 10%, the SPRs vary about 1% as well. Thus the total uncertainty in the calculated SPRs will be about 1.4% if considering these two uncertainty factors to be independent.

However, there exist correlations between these two variations because a major fraction of soft tissues is water (Valentin and Streffer, 2002; Woodard and White, 1986). The mean excitation energies of water and soft tissues should vary in the same direction, so the uncertainties in the calculated SPRs of human tissues should be smaller. A variation study was conducted to estimate the uncertainties in SPR calculations with this correlation considered. Our way of considering the correlation was to introduce variations to the mean excitation energies of the elements first and then calculating the mean excitation energies of human tissues based on those varied values of elements, instead of introducing variations to the mean excitation energies of human tissues directly. Three variation scenarios were considered:

- Scenario 1: increasing or decreasing the mean excitation energies of all elements by 10% at the same time;
- Scenario 2: increasing or decreasing the mean excitation energies of all elements by 10% except for H and O;
- Scenario 3: increasing or decreasing only the mean excitation energies of H and O by 10%.

3.2.3.5 *SPR Variations with Proton Energies*

Another source of uncertainties in calculated SPRs is the proton energy. According to the Bethe-Bloch equation, the SPR is a function of proton energy (β). But current treatment planning systems ignore the SPR's dependency on proton energy by calculating dose based on SPRs at a single proton energy for simplicity. Although the

SPR is known to be approximately constant with proton energy, this approximation causes additional uncertainty.

The uncertainty from ignoring the SPR dependency on proton energy was estimated by comparing proton ranges in human tissues calculated with and without considering proton energy variations. Two human tissues, the adipose tissue and the cortical bone, were chosen for this comparison, because the differences between their mean excitation energies and that of water are the largest among all ‘reference’ human tissues listed in Table 2. According to the Bethe-Bloch equation, their SPRs have the largest variation with proton energy. The proton range in human tissues without considering proton energy variation was calculated by simply multiplying the proton range in water and the SPR at a chosen proton energy, simulating the process of current treatment planning systems. In this study, the chosen proton energy was 175 MeV, i.e., the energy chosen for treatment planning at the UTMDACC PTC. The proton range in human tissues with considering SPR variation with energy was taken from the database on the website of the National Institutes of Standards and Technology (NIST) – the stopping-power and range tables for protons (PSTAR). The PSTAR database provides the projected proton ranges of various materials including water, adipose tissue and cortical bone (ICRU, 1993).

3.2.3.6 *Composite Range Uncertainty*

In addition to dividing the uncertainties into different categories according to their origins, human tissues were also divided into three different tissue groups, i.e., lung tissues, soft tissues and bone tissues, because their uncertainty estimates were found to be substantially different. An uncertainty estimate of each category was

determined for each tissue group separately. The total uncertainty was determined for each tissue group by adding the uncertainty estimates of all categories in quadrature. For treatment planning purposes, it is best to provide a single composite range uncertainty. The composite range uncertainty was estimated by combining the uncertainty estimates for all tissue groups into a single value based on their tissue proportions.

15 proton patients, including 5 prostate, 5 lung and 5 head-and-neck (H&N) patients, were selected to determine the tissue proportion for each tissue group. The beam angles and planning target volume (PTV) from the original proton plan were used, in order to make realistic estimates. The CT voxels along each ray to the proximal or distal end of the PTV were categorized into lung tissues, soft tissues, and bone tissues based on their CT numbers. In order to identify the appropriate CT numbers to separate tissue groups, CT number histograms were generated based on patients CT images (Fig. 10). From the histograms, a CT number value of 800 was chosen to separate lung tissues and soft tissues, and 1200 chosen to separate soft tissues and bone tissues. The range uncertainties of all three tissue groups were combined to produce a composite range uncertainty (σ_R) for each ray by

$$\sigma_R = w_L * \sigma_L + w_S * \sigma_S + w_B * \sigma_B \quad , \quad (14)$$

where w_L , w_S and w_B are the tissue proportions of lung tissues, soft tissues, and bone tissues along each ray, respectively, and σ_L , σ_S and σ_B are the range uncertainties for lung tissues, soft tissues, and bone tissues, respectively. The values of σ_L , σ_S and σ_B , used in calculating the composite range uncertainty for each ray, were sampled from a

Gaussian distribution with mean equal to zero and standard deviation equal to the estimated uncertainty (1σ) of the corresponding tissue group.

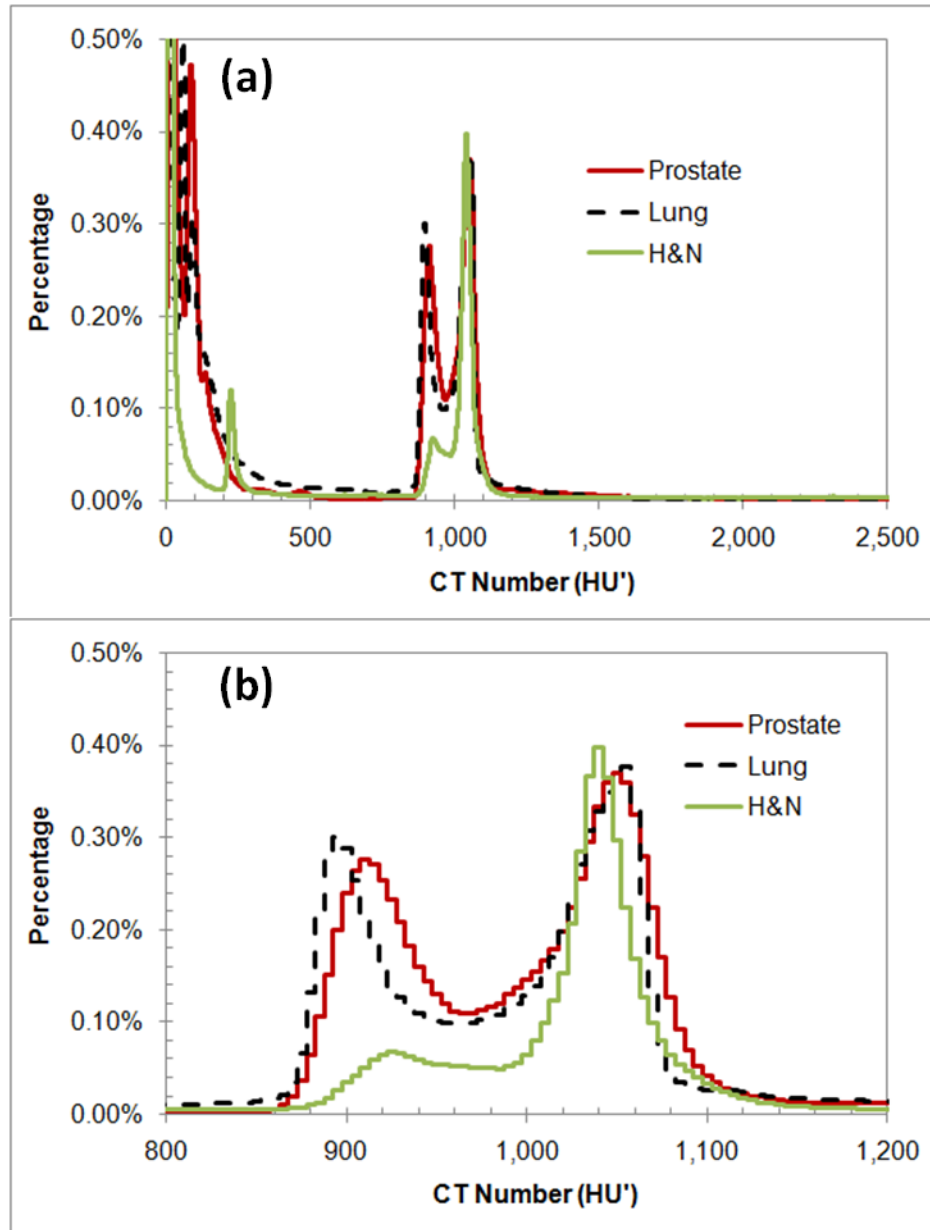


Figure 10. (a) CT number histogram for lung, prostate and head-and-neck patients; (b) The zoomed-in version of (a), which shows 800 and 1200 can be used to separate soft tissues from lung tissues and bone tissues.

3.3 Results

3.3.1 Uncertainties in SPR Estimation

3.3.1.1 *Inherent Uncertainties*

The histogram and statistics of the inherent uncertainties are shown in Fig. 11 and Table 5, respectively. The soft tissue group had the largest inherent uncertainties. The bone tissue group had relatively smaller inherent uncertainties because of the good linearity between CT numbers and SPRs of bone tissues. It could be due to the fact that the densities and elemental compositions of bone tissues, except the cortical bone, were simply determined by linear combinations of the densities and elemental compositions of the cortical bone and a few soft tissues such as red marrow, yellow marrow and cartilage (Woodard and White, 1982).

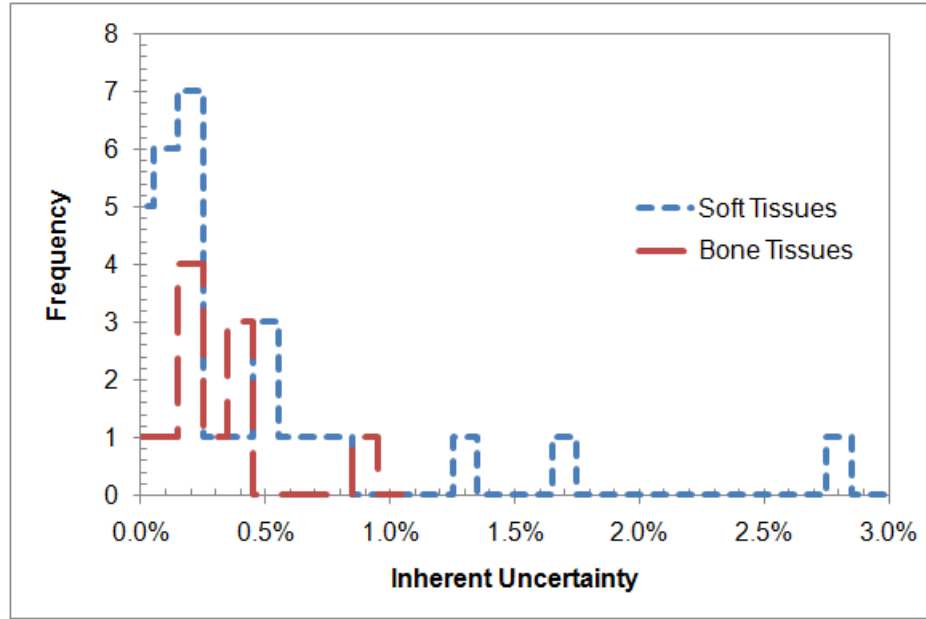


Figure 11. Histogram of the inherent uncertainties in SPRs of the ‘reference’ human body tissues estimated using the stoichiometric method.

Table 5. Statistics of the inherent uncertainties (1σ) in SPRs of the ‘reference’ human body tissues estimated using the stoichiometric method.

Tissue Groups	Inherent Uncertainties (1σ)
Lung Tissues	0.00%
Soft Tissues	0.43%
Bone Tissues	0.29%

The SPRs of the ‘individualized’ human tissues calculated using the Bethe-Bloch equation were plotted against their predicted CT numbers calculated using Eq. 6 in Fig. 12, together with the ‘reference’ human tissues and the calibration curve. The ‘individualized’ human tissues fitted worse with the calibration curve than the ‘reference’ human tissues as expected. For soft tissues, the density variation was the dominant factor (Fig. 12(a)). The histogram and statistics of the inherent uncertainties for the ‘individualized’ human tissues are shown in Fig. 13 and Table 6, respectively.

The inherent uncertainties increased substantially for both soft tissues and bone tissues in the presence of tissue composition variations. For soft tissues, the inherent uncertainties doubled at least, while for bone tissues it increased by at least four times. The large increase of the inherent uncertainties for bone tissues shows that the SPR estimation for bone tissues is very sensitive to tissue composition variations.

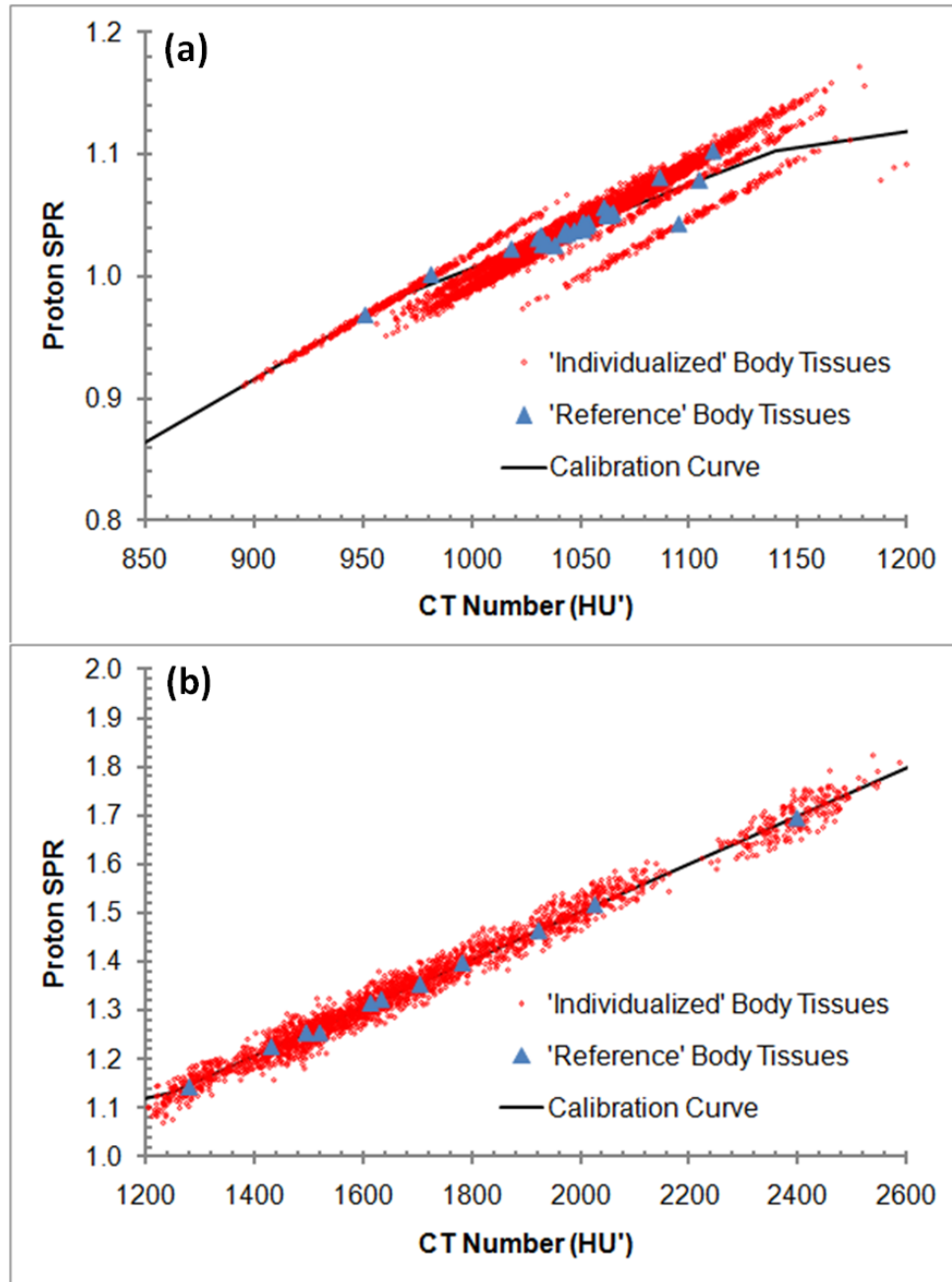


Figure 12. CT calibration curve shown with the ‘reference’ body tissues and the ‘individualized’ body tissues. (a) and (b) are zoomed in on the soft tissue and bone tissue region, respectively.

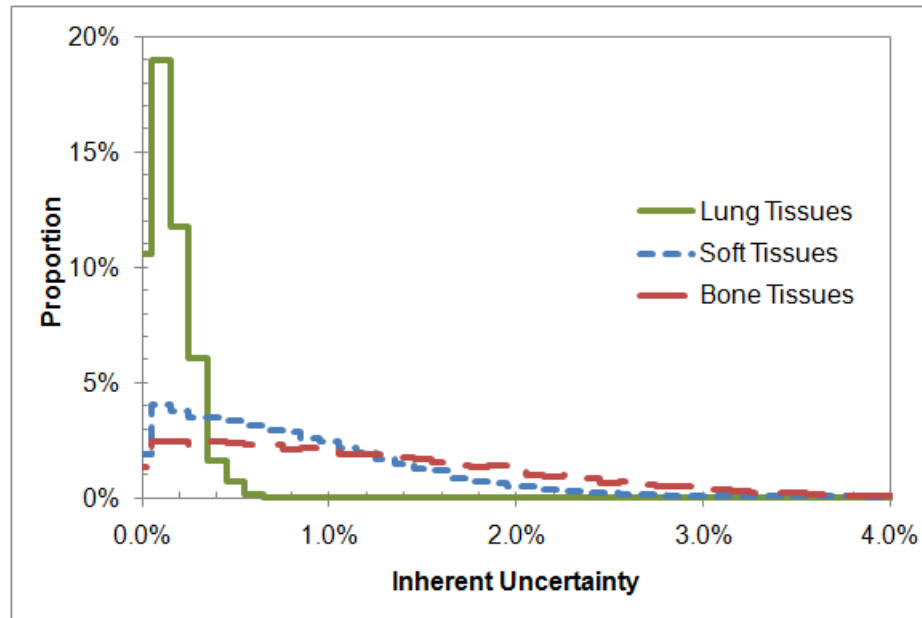


Figure 13. Histograms of the inherent uncertainties in proton SPRs of the ‘individualized’ human body tissues estimated using the stoichiometric method.

Table 6. Statistics of the inherent uncertainties (1σ) in SPRs of the ‘individualized’ human body tissues estimated using the stoichiometric method.

Tissue Groups	Inherent Uncertainties (1σ)
Lung Tissues	0.18%
Soft Tissues	1.24%
Bone Tissues	1.59%

3.3.1.2 Modeling Errors in Predicted CT Numbers

The measured CT numbers of the tissue substitutes used in the calibration were compared with their predicted CT numbers (Fig. 14). The lung tissue group had the largest errors in the predicted CT numbers (Table 7), which is probably due to the fact that the lung tissue substitute was not included in the calibration subset in order to

achieve a better fit in the soft tissue and bone tissue range. The modeling errors in the soft tissue group had the largest spread. This agrees with our observation in Table 5 that the soft tissue group had the largest inherent uncertainties, which is a manifestation of the non-linearity between CT numbers and SPRs of soft tissues.

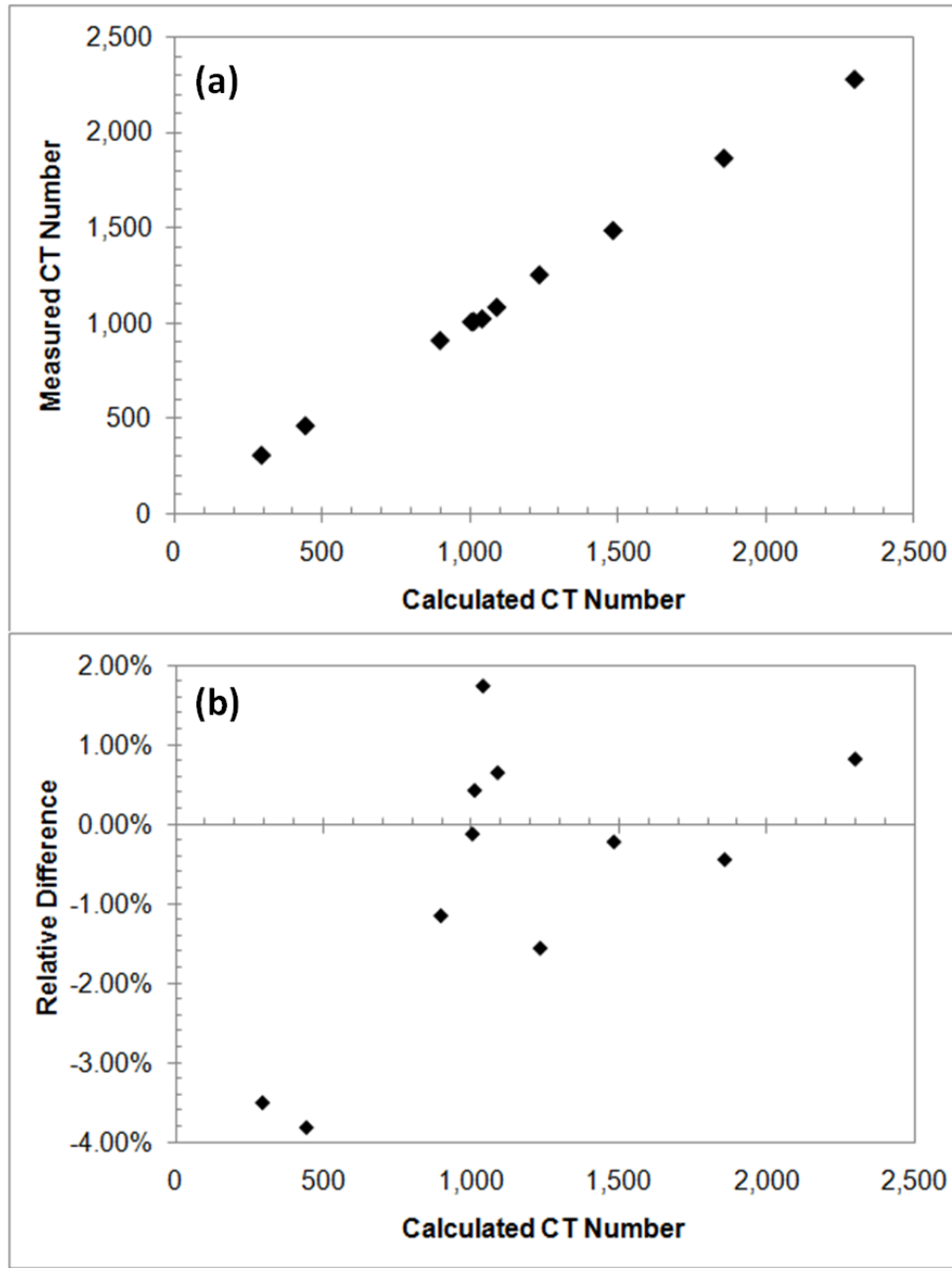


Figure 14. (a) Measured versus calculated CT numbers of the tissue substitutes; (b) The difference between the measured and calculated CT numbers of the tissues substitutes relative to the calculated CT numbers.

Table 7. Statistics of the modeling errors (1σ) in predicted CT numbers of the tissue substitutes and the induced errors in estimated SPRs.

Tissue Groups	Modeling Errors (1σ)	
	CT Number	SPR
Lung Tissues	3.66%	3.76%
Soft Tissues	1.00%	0.75%
Bone Tissues	0.92%	0.53%

3.3.1.3 *CT Imaging Uncertainties*

We obtained five monthly QA data sets for the ACB CT1 and CT2, and seven data sets for the PTC CT (Table 8). The mean CT numbers measured by different scanners were within 1% from each other for most tissue substitutes (Table 9). The mean CT numbers and standard deviations were calculated for each tissue substitute based on the data from all three CT scanners. The monthly QA for the PTC CT included 5 additional tissue substitutes, which were not used for the ACB CT1 and CT2. For those tissue substitutes, only the data from the PTC CT were used to calculate the mean values and standard deviations. The SPR variations were calculated by multiplying the CT number variations with the CT number-to-SPR variation ratios listed in Table 4. The CT numbers of the soft tissue group varied less than those of the lung and bone tissue groups (Table 10).

Table 8. CT measurements of tissue substitute inserts scanned during monthly QA for three treatment planning CT scanners at UTMDACC.

Tissue Substitutes	ACB CT1					ACB CT2					PTC CT						
LN-450	471	477	468	472	470	471	487	472	471	470	463	465	464	464	466	467	465
Adipose	914	914	917	914	915	915	922	913	914	912	920	913	913	917	915	910	911
Solid Water	1010	1006	1004	1012	1012	1005	1000	1004	1004	1007	1005	1004	1008	1010	1008	1006	1007
Real Water	1007	1007	1013	1009	1012	1006	1009	1007	1007	1007	1004	1007	1007	1007	1006	1004	1004
Breast	957	955	957	957	958	956	958	955	954	954	958	969	966	966	963	963	960
Inner Bone	1222	1221	1215	1223	1220	1213	1196	1213	1215	1213	1223	1216	1221	1223	1220	1222	1223
Cortical Bone	2233	2234	2216	2231	2223	2208	2176	2208	2211	2209	2181	2188	2200	2222	2218	2228	2211
LN-300											316	309	315	315	314	314	314
Liver											1087	1087	1091	1094	1092	1091	1090
B-200											1221	1223	1228	1232	1230	1234	1235
CB2-30%											1437	1440	1442	1423	1448	1454	1443
CB2-50%											1800	1799	1816	1804	1821	1821	1800

Table 9. Statistics of CT number variations with time and scanner and the induced SPR variations for tissue substitutes.

Tissue Substitutes	ACB CT1		ACB CT2		PTC CT		Mean	σ	Rel. CT# Var. (σ/Mean)	Rel. SPR Var. (σ/Mean)
	Mean	σ	Mean	σ	Mean	σ				
Lung-450	471	3.4	474	7.3	465	1.4	469	5.8	1.2%	1.3%
Adipose	915	1.5	915	3.9	914	3.6	915	3.1	0.3%	0.3%
Solid Water	1009	3.6	1004	2.7	1007	2.1	1007	3.2	0.3%	0.2%
Water	1010	2.6	1007	1.2	1005	1.6	1007	2.5	0.2%	0.2%
Breast	957	1.1	955	1.8	964	3.8	959	4.6	0.5%	0.3%
Inner Bone	1220	3.1	1210	7.8	1221	2.5	1218	6.7	0.6%	0.3%
Cortical Bone	2227	7.7	2202	14.8	2207	17.6	2212	17.3	0.8%	0.5%
Lung-300					314	2.2	314	2.2	0.7%	0.7%
Liver					1090	2.5	1090	2.5	0.2%	0.2%
B-200					1229	5.2	1229	5.2	0.4%	0.2%
CB2-30%					1441	9.8	1441	9.8	0.7%	0.4%
CB2-50%					1809	10.1	1809	10.1	0.6%	0.4%

Table 10. Statistics of relative CT number and SPR variations (1σ) with time and scanner for different tissue groups.

Tissue Groups	Relative Variation (1σ)	
	CT#	SPR
Lung Tissues	1.00%	1.03%
Soft Tissues	0.33%	0.25%
Bone Tissues	0.61%	0.38%

Table 11 lists CT numbers of various tissue substitutes scanned at the center of the head phantom and the body phantom, respectively. The relative difference in the measured CT numbers was calculated for each tissue substitute by $\frac{HU'_{\text{Large}} - HU'_{\text{Small}}}{HU'_{\text{Large}} + HU'_{\text{Small}}}$. The CT numbers of the soft tissue group were very stable as the phantom size changed: the maximal CT number difference was only 0.6%. The CT number of water was even more stable: the difference was less than 0.2%. However, the CT numbers of the lung tissue and bone tissue group varied substantially with a maximal difference larger than 3.5%. This large CT number variation for the lung tissue and bone tissue groups was due to the fact that their photon attenuation properties are very different from water and current CT scanners are calibrated using water phantom. It was observed in Table 11 that the CT numbers of lung tissues scanned in the large (body) phantom were always larger than the values scanned in the small (head) phantom. The opposite was observed for bone tissues: the CT numbers acquired in the body phantom were always smaller than those in the head phantom. This was most likely due to the beam hardening effect. The x-ray beam passing through the body phantom should be ‘harder’ compared to the one passing through the head phantom. For a ‘harder’ x-ray beam, the difference between photon attenuation coefficients of the material of interest and the reference

material, water, becomes smaller. Thus, the CT numbers of lung tissues increase and the CT numbers of bone tissues decrease.

Table 11. CT measurements of various tissue substitutes scanned at the center of the head phantom and the body phantom, respectively, and the relative differences in CT numbers and SPRs related to the size of the phantom. The maximal relative difference was determined based on the absolute values of relative differences of all the tissues within one tissue group.

Tissue Groups	Tissue Substitutes	CT Number			Relative Difference		Maximal Relative Difference	
		Small	Large	Mean	CT#	SPR	CT#	SPR
Lung Tissues	LN-300	292	323	308	5.13%	5.30%	5.13%	5.30%
	LN-450	447	478	463	3.40%	3.48%		
Soft Tissues	Adipose	902	919	910	0.93%	0.85%	0.93%	0.85%
	Breast	950	961	955	0.61%	0.41%		
	Solid Water	1007	1012	1010	0.24%	0.16%		
	Brain	1019	1030	1024	0.54%	0.38%		
	Liver	1084	1085	1085	0.05%	0.04%		
	Water	1006	1010	1008	0.19%	0.13%		
Bone Tissues	Inner Bone	1020	1022	1021	-1.27%	-0.69%	3.69%	2.53%
	B-200	1271	1239	1255	-1.29%	-0.70%		
	CB2-30%	1517	1459	1488	-1.93%	-1.13%		
	CB2-50%	1924	1812	1868	-2.98%	-1.91%		
	Cortical Bone	2367	2198	2282	-3.69%	-2.53%		

Table 12 lists CT numbers of various tissue substitutes when scanned at the center and at the periphery of the body phantom, respectively. The relative CT number difference was calculated by $\frac{HU'_{\text{Peripheral}} - HU'_{\text{Center}}}{(HU'_{\text{Peripheral}} + HU'_{\text{Center}})/2}$. The CT numbers of the soft tissue group remained very stable with the position in the scan: the maximal difference was less than 0.2%. The CT numbers of the lung and bone tissue groups varied substantially, with the maximal difference larger than 2%. The CT numbers of lung tissues scanned at the center were found to be larger than those scanned at the periphery, while the CT

numbers of bone tissues were found to vary in the opposite direction. Again, this was likely due to the beam hardening effect: the beam spectrum at the center was ‘harder’ than that at the periphery so the CT number difference between the material of interest and water was smaller at the center compared to that at the periphery.

Table 12. CT measurements of various tissue substitutes scanned at the center and the periphery of the body phantom, respectively, and the relative differences in CT numbers and SPRs related to the position in the phantom. The maximal relative difference was determined based on the absolute values of relative differences of all the tissue substitutes within one tissue group.

Tissue Groups	Tissue Substitutes	CT Number		Relative Difference		Maximal Relative Difference	
		Center	Peripheral	CT#	SPR	CT#	SPR
Lung Tissues	LN-300	323	315	-2.64%	-2.73%	2.64%	2.73%
	LN-450	478	471	-1.57%	-1.61%		
Soft Tissues	Adipose	919	917	-0.25%	-0.23%	0.25%	0.23%
	Breast	961	961	0.00%	0.00%		
	Solid Water	1012	1012	0.02%	0.01%		
	Brain	1030	1030	0.00%	0.00%		
	Liver	1085	1087	0.16%	0.11%		
	Water	1010	1011	0.15%	0.11%		
Bone Tissues	Inner Bone	1022	1025	0.74%	0.40%	2.06%	1.42%
	B-200	1239	1248	0.67%	0.37%		
	CB2-30%	1459	1475	1.05%	0.62%		
	CB2-50%	1812	1842	1.62%	1.04%		
	Cortical Bone	2198	2244	2.06%	1.42%		

The body phantom was scanned sequentially with three different materials inserted at the same peripheral location, which were air, liver and cortical bone. The CT numbers of solid water inserts at other locations were measured and compared among all three scans. The CT number difference was negligible ($\sim 0.1\%$) so the data is not shown here.

In order to investigate the impact of objects outside the FOV to CT measurements inside the FOV, the RMI 467 phantom with the same distribution of

tissue substitute inserts was scanned while different material inserts were put outside the FOV. The impact of this was also found to be negligible. However, one special object to consider was the couch of the CT scanner, which can be inside or outside the FOV depending on patient size and tumor location. The couch position was found to have a relatively large impact to the CT measurements inside the FOV (Table 13), especially for lung and bone tissues. The relative CT number difference was calculated by

$$\frac{HU'_{\text{out-of-field}} - HU'_{\text{in-field}}}{(HU'_{\text{out-of-field}} + HU'_{\text{in-field}})/2}.$$

Table 13. CT measurements of various tissue substitutes scanned in the RMI 467 phantom with two different couch positions, respectively, and the relative differences in CT numbers and SPRs. The maximal relative difference was determined based on the absolute values of relative differences of all the tissues within one tissue group.

Tissue Groups	Tissue Substitutes	CT Number		Relative Difference		Maximal Relative Difference	
		In-field	Out-of-field	CT#	SPR	CT#	SPR
Lung Tissues	LN-300	320	316	-1.36%	-1.40%	2.09%	2.14%
	LN-450	479	489	2.09%	2.14%		
Soft Tissues	Breast	955	960	0.54%	0.37%	0.54%	0.37%
	Solid Water	1008	1009	0.09%	0.06%		
	Brain	1023	1028	0.47%	0.33%		
	Liver	1080	1083	0.24%	0.17%		
	Water	1003	1007	0.32%	0.22%		
Bone Tissues	Inner Bone	1207	1214	0.56%	0.30%	0.91 %	0.62%
	B-200	1227	1235	0.69%	0.38%		
	CB2-30%	1435	1441	0.37%	0.22%		
	CB2-50%	1775	1792	0.92%	0.59%		
	Cortical Bone	2159	2179	0.91%	0.62%		

Table 14 lists our estimates of CT imaging uncertainties (1σ) due to each major factor and their induced SPR uncertainties. Overall, CT measurements of soft tissues

were much more stable than those of lung and bone tissues. For soft tissues, the factors – time and scanner, patient size and couch position had similar impact. For both lung and bone tissues, patient size was the dominant factor. These factors were independent so the uncertainties due to each factor were added in quadrature to estimate the total uncertainty.

Table 14. Statistics of CT number uncertainties (1σ) due to different factors and the induced uncertainties in SPRs for different tissue groups.

	Tissue Groups	Major Uncertainty Contributing Factors				Total (Root-sum-square)
		Time and Scanner	Patient Size	Position in the Scan	Couch Position	
CT#	Lung	1.00%	2.56%	1.32%	1.05%	3.23%
	Soft	0.33%	0.30%	0.08%	0.27%	0.53%
	Bone	0.61%	1.85%	1.03%	0.46%	2.25%
SPR	Lung	1.03%	2.65%	1.37%	1.07%	3.33%
	Soft	0.25%	0.21%	0.06%	0.18%	0.38%
	Bone	0.38%	1.27%	0.71%	0.31%	1.53%

3.3.1.4 *Uncertainties in Mean Excitation Energies*

Variations were introduced to the mean excitation energies of elements as described in Section 3.2.3.4. The SPRs calculated based on the new values of elemental mean excitation energies were compared to the SPRs calculated based on the original values of elemental mean excitation energies. In Scenario 1, when the mean excitation energies of all elements were increased or decreased by 10% simultaneously, the SPR differences were less than 0.1% for all tissues. In Scenario 2 and 3, when the mean excitation energies of either only hydrogen (H) and oxygen (O), or all elements except for H and O were changed by 10%, the SPR deviations were found to be larger, especially for bone tissues. The maximal difference among all scenarios was chosen for

each tissue and used to calculate statistics (Fig. 15). Soft tissues tended to have smaller SPR differences compared to bone tissues, as expected (Table 15).

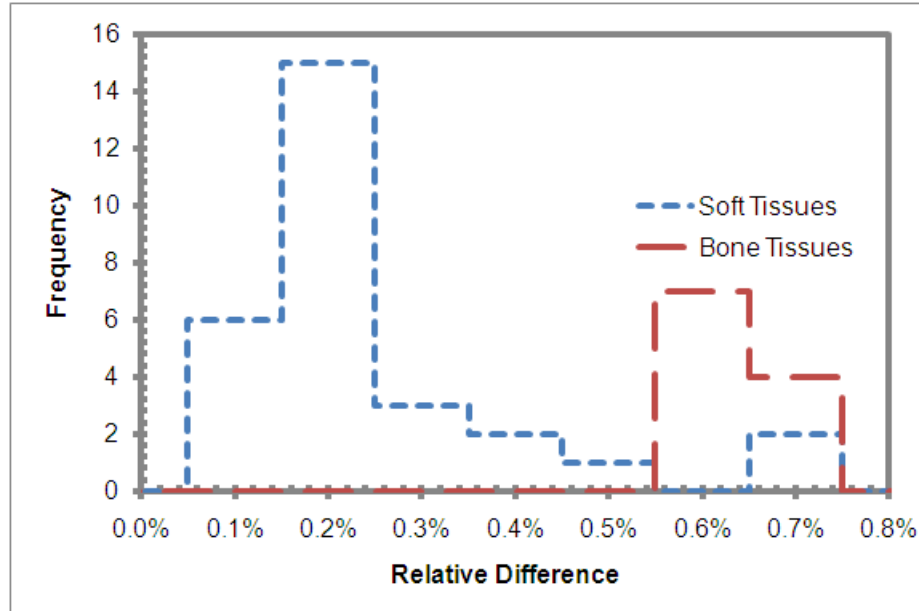


Figure 15. Histograms of relative differences between the SPRs calculated based on the original elemental mean excitation energies and the SPRs calculated based on the values with variations for all 41 ‘reference’ human tissues (Table 2). The histograms were based on the maximal relative differences among all three scenarios.

Table 15. Statistics of relative differences in calculated SPRs due to variations of the elemental mean excitation energies.

Tissue Groups	Relative Differences in Calculated SPRs (1σ)
Lung Tissues	0.17%
Soft Tissues	0.23%
Bone Tissues	0.65%

3.3.1.5 *SPR Variations with Proton Energies*

Relative errors in the calculated proton ranges in human tissues when ignoring proton energy variation were determined for various initial proton energies. In proton radiotherapy, the initial proton energy before entering patients varies depending on the depth of the tumor, so it is more straightforward to plot the relative range error versus the projected range in water instead of the proton energy. For reference, the projected range in water versus the proton energy is shown in Fig. 16. The absolute value of the relative range error increases as the projected range in water decreases (Fig. 17(a)). According to our experience, the distal end of tumors treated at the PTC is mostly deeper than 5 cm. Thus, the relative range error at 5 cm was regarded as the worst-case estimate (2σ). The relative error in the calculated proton range is small at typical tumor depths for both the adipose tissue and cortical bone (less than 0.5% for tumors deeper than 10 cm). Even when the tumor is as shallow as 5 cm, the relative range error is still less than 0.5% for soft tissues similar to adipose tissue. The absolute range error was also plotted against the projected range in water (Fig. 17(b)). The largest absolute range error is about 0.3 mm and 0.6 mm for the adipose tissue and cortical bone, respectively, occurring when the tumor is at about 20 cm depth.

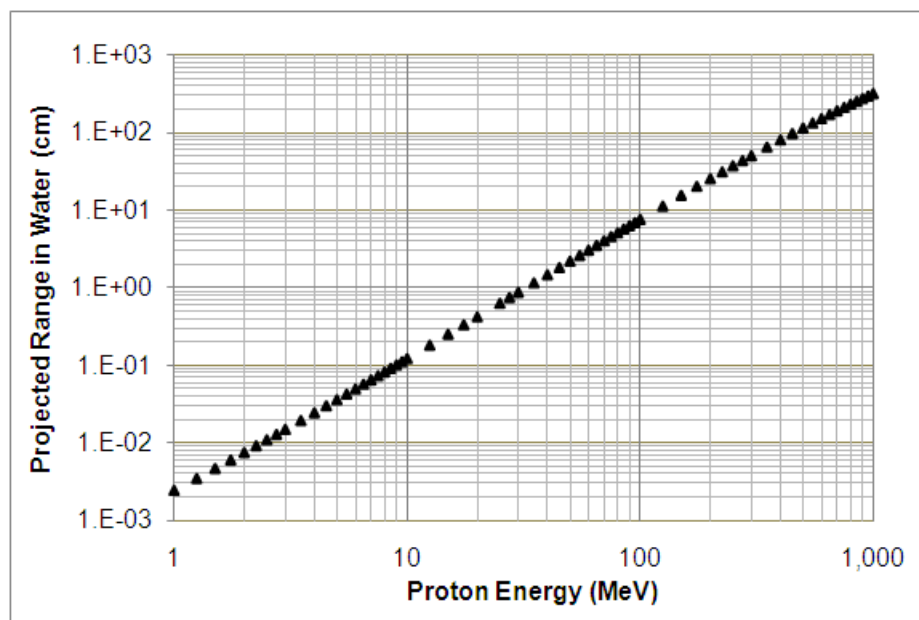


Figure 16. Projected proton range in water at different energies from the NIST PSTAR database.

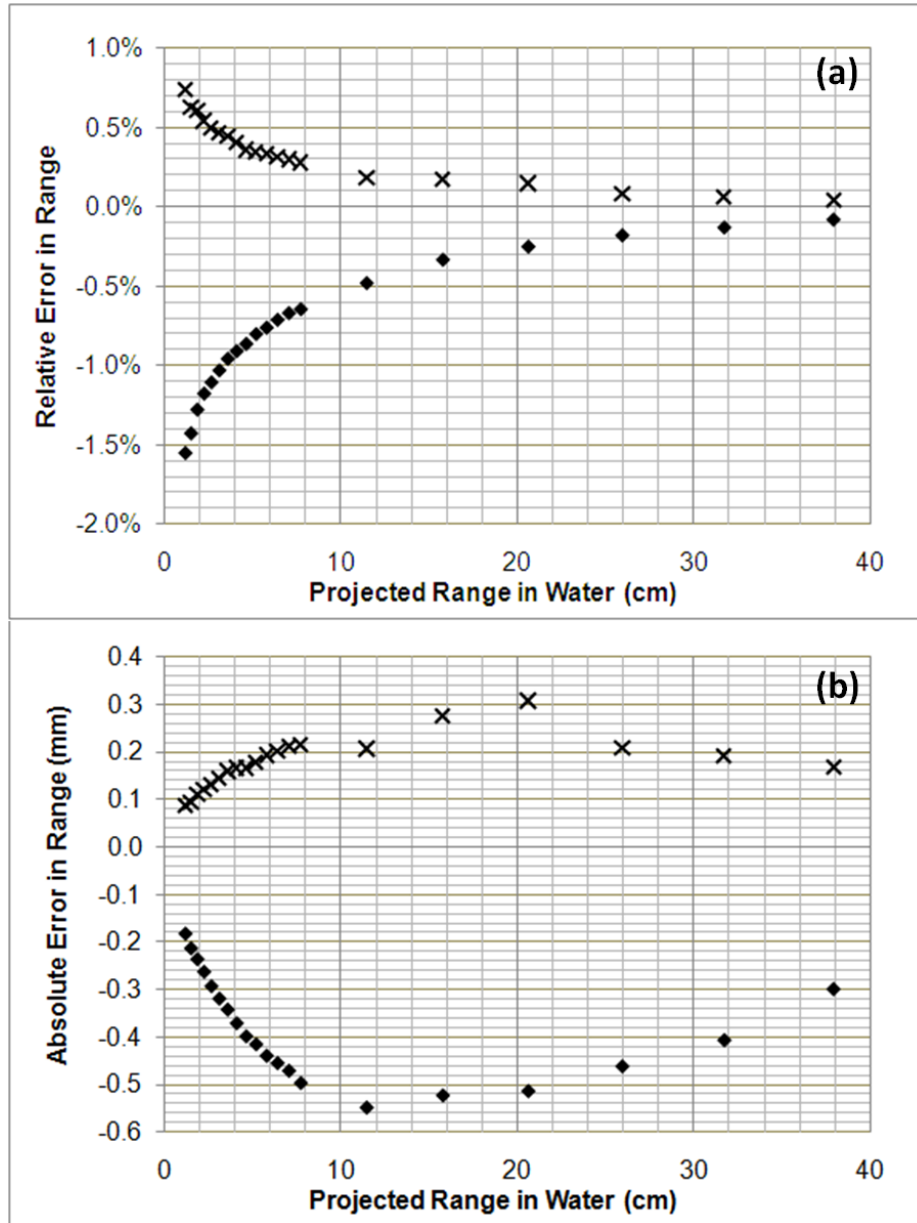


Figure 17. (a) relative and (b) absolute error in the calculated proton range caused by using SPRs based on a single energy of 175MeV versus the projected range in water for the adipose tissue (x) and cortical bone (♦).

3.3.1.6 Composite Range Uncertainty

Table 16 lists our estimates of the relative range uncertainties related to proton SPR estimation. The dominant uncertainty contributing factor for soft tissues and bone tissues is the inherent uncertainty in the presence of tissue composition variations, while

it is CT imaging uncertainty for lung tissues. This shows that it is important to reduce the impact of tissue composition variations in order to reduce the overall uncertainty in proton SPR estimation.

Table 16. Summary of our estimates of relative range uncertainties (1σ) related to proton SPR estimation in current clinical practice.

Uncertainty Sources		Relative Range Uncertainty		
		Lung	Soft	Bone
Inherent uncertainty in the presence of human tissue composition variations		0.2%	1.2%	1.6%
CT# Related	Modeling errors in predicted CT numbers	3.8%	0.8%	0.5%
	CT imaging uncertainties	3.3%	0.6%	1.5%
SPR Related	Uncertainties in mean excitation energies	0.2%	0.2%	0.6%
	SPR variations with proton energy	0.2%	0.2%	0.4%
Total (RSS)		5.0%	1.6%	2.4%

The relative weight of each tissue group along the beam path from skin to the proximal or distal end of the PTV was determined for three tumor sites commonly treated with proton therapy, i.e., prostate, lung and head-and-neck (Table 17). Based on the tissue proportion and the estimated uncertainties for each tissue group (Table 16), the composite range uncertainty was calculated using Eq. 14. Table 18 lists the median, the 90th percentile and the 95th percentile composite range uncertainty for prostate, lung and head-and-neck patients. No significant difference exists between the range uncertainties to the proximal and distal ends. Table 18 shows that the current value used for the distal and proximal margin design, 3.5%, is comparative to what we estimated (3.0- 3.4%).

Table 17. Mean, standard deviation (σ) and standard error of mean (SEM) of relative weights of each tissue group in different clinical situations.

Tumor Sites	Distal or Proximal	Relative Weight (%)								
		Lung Tissues			Soft Tissues			Bone Tissues		
		Mean	σ	SEM	Mean	σ	SEM	Mean	σ	SEM
Prostate	Distal	0.5	0.2	0.00	80.2	8.4	0.10	19.3	8.4	0.10
	Proximal	0.7	0.2	0.00	75.8	10.7	0.13	23.5	10.7	0.13
Lung	Distal	11.1	10.2	0.05	81.6	11.9	0.05	7.3	7.4	0.03
	Proximal	10.2	9.8	0.05	80.2	13.4	0.07	9.6	10.9	0.05
Head & Neck	Distal	2.6	2.3	0.02	86.8	11.2	0.11	10.5	10.8	0.11
	Proximal	3.5	2.6	0.03	82.9	12.5	0.13	13.6	12.5	0.13

Table 18. Median, 90th percentile and 95th percentile of composite range uncertainties and the corresponding percentile when range uncertainty is equal to 3.5%, respectively, at different clinical situations.

Tumor Sites	Distal or Proximal	Composite Range Uncertainty			Percentile when Range Uncertainty = 3.5%
		Median	90th Percentile	95th Percentile	
Prostate	Distal	1.3%	2.5%	3.0%	98.4%
	Proximal	1.3%	2.6%	3.0%	98.4%
Lung	Distal	1.5%	2.9%	3.4%	95.6%
	Proximal	1.5%	2.9%	3.4%	96.0%
Head & Neck	Distal	1.3%	2.6%	3.0%	97.7%
	Proximal	1.3%	2.7%	3.1%	97.6%

3.4 Discussion

3.4.1 Comparison of Our Estimates with the Estimates from Other Groups

An estimate of the 3.5% range uncertainty in current clinical practice was first proposed by Moyers *et al.* (2001). Since then, people started to use that value to design proximal and distal target volume margins for proton therapy. However, Moyers *et al.* did not explain how they derived that value until their recent paper (Moyers *et al.*, 2009), which gave a detailed analysis. We used their analysis as a reference in our

evaluation, but we did not agree with their estimates for some categories. In the following discussion, we focused on comparing our estimates to theirs and also to the estimates from other groups (Schaffner and Pedroni, 1998; Trofimov *et al.*, 2010).

The major difference between our estimates and the estimates by Moyers *et al.* is the CT imaging uncertainty. They stated that the measured CT number values of water were found to vary up to 2.5% (5% spread) with the size of the phantom and the position in the scan. Their statement was based on some data from the literature (Chen *et al.*, 1979; Cann, 1987; Constantinou *et al.*, 1992), which were all measured more than 15 years ago. Modern CT scanners, however, are much more stable. According to the CT accreditation requirements published by the American College of Radiology (2003), modern CT scanners should achieve a flat profile less than $\pm 0.5\%$ for a scan of a uniform water phantom. In our measurements, the mean CT number of water in a region-of-interest (ROI) did not vary by much. The variation of mean CT numbers of water was always less than 0.5%, even when the phantom size and the position in the scan were changed together. The total imaging uncertainties for soft tissue substitutes were found to be less than 1%. However, we did observe that the CT numbers of lung tissues and bone tissues could vary up to 4%. But the large CT number uncertainties of lung tissues and bone tissues do not make large contributions to the composite range uncertainty because of their low percentages in human bodies. In addition, the variation ratio between CT numbers and SPRs ($\frac{d\rho'_s/\rho'_s}{dHU'/HU'}$) was not considered in their estimates. As shown in Section 3.2.3.3, 1% CT number variation only translates into about 0.7% SPR variation for soft tissues and bone tissues.

Another major difference between our estimates and their estimates is that we considered the uncertainties in the recommended tissue compositions of human body tissues from the literature while Moyers *et al.* did not. Our survey of the literature shows that there existed uncertainties in the recommended tissue compositions (Woodard and White, 1986; White *et al.*, 1991). The estimate of the uncertainties in the conversion of CT numbers to SPRs made by Moyers *et al.* was based on the results from Schaffner and Pedroni (1998), which measured a limited number of animal tissue samples. Our estimate was based on a ‘population’ study, which considered both systematic and individual (statistical) uncertainties in the recommended tissue compositions. The parameters used in the population study were determined through a thorough literature search.

Another difference between our estimates and their estimates is that Moyers *et al.* included the uncertainty in the stopping power of water (~1%) while we did not. We agree that there exists at least 1% uncertainty in the stopping power of water, but we do not agree that it should be included when calculating range uncertainty. This is because the stopping power of water is not directly used by current treatment planning systems to calculate proton range and dose distribution in tissue. The proton range in tissue is determined by multiplying the proton range in water and the tissue’s SPR relative to water. The range in water is directly measured for protons of various energies during the commissioning of the treatment planning system. The precision of range measurements in water is 0.5 mm. At UTMDACC, this uncertainty is covered by a 3 mm distal margin in addition to the 3.5% margin.

Our approach to estimate the uncertainties in calculated SPRs of human body tissues is also different from the approach taken by Moyers *et al.* They estimated the uncertainties by comparing the measured SPRs and the calculated SPRs of various materials. Their approach is straightforward, and they did observe some large differences between the measured SPRs and the calculated SPRs (1% - 3%). But there are other potential factors contributing to the observed differences in addition to the uncertainties in SPR calculation, such as the SPR measurement uncertainties (up to 2%), and the uncertainties in the elemental compositions of the materials used in their SPR calculation. We took a theoretical approach by introducing variations to elemental mean excitation energies directly and then estimated the variations in calculated SPRs of human tissues. Our reasoning was that the uncertainties in calculated SPRs of human tissues are primarily due to the uncertainties in the mean excitation energies of water and human tissues in the literature. The advantages of our approach include that the whole analysis was based on human body tissues, and other contributing factors existing in the measurement approach are ruled out. In addition, the ‘correlation’ between human tissues and water were considered.

The last difference between our estimates and their estimates is the uncertainty in range calculation due to ignoring the proton energy change along the beam path. The estimate by Moyers *et al.* was based on the difference of SPRs of the same material at different energies while our estimate was based on the difference between proton ranges calculated with and without considering proton energy change. Our analysis showed that the SPR at very low energies (≤ 10 MeV) can be a few percent different from the SPR at 175 MeV. The relative difference between SPRs at 10 MeV and 175 MeV is

1.0% for adipose tissue and -2.1% for cortical bone (Table 19). But the distance that a low energy proton can travel is very limited (a 10 MeV proton's projected range in water is less than 2 millimeters). This indicates that a large difference of SPR at very low energies does not translate to a large range difference. Therefore, it will be over-estimating to use the differences between SPRs at different energies as a rough estimate of the range uncertainty caused by ignoring SPR variation with energy.

Table 19. Proton SPRs for adipose tissue and cortical bone at different proton energies and their relative differences compared to the SPRs at 175 MeV.

Proton Energy (MeV)	SPR		Relative Difference Compared to the SPR at 175MeV	
	Adipose Tissue	Cortical Bone	Adipose Tissue	Cortical Bone
250	1.02	0.96	-0.1%	0.2%
175	1.02	0.96	0.0%	0.0%
125	1.02	0.96	0.1%	-0.2%
75	1.02	0.95	0.2%	-0.4%
50	1.02	0.95	0.3%	-0.7%
25	1.03	0.95	0.5%	-1.2%
10	1.03	0.94	1.0%	-2.1%
5	1.03	0.93	1.4%	-3.0%
1	1.05	0.90	3.0%	-6.5%

Schaffner and Pedroni's (1998) estimates included two parts: the uncertainty in converting CT numbers to SPRs, and the uncertainty due to the beam hardening effect. They measured both CT numbers and SPRs experimentally for a limited number of animal tissues. The measured SPRs were then compared to the SPRs derived from the CT numbers using the calibration curve. They found that the differences between the measured SPRs and the derived SPRs were less than 1%. The strength of their estimates was that they were based on direct experimental measurements. However, because of

this, they could not measure SPRs for a large range of tissue samples. They admitted in their paper that their estimates were based on the assumption that there would not be considerable variations in human tissue compositions. Our estimates were based on a 'population' study which considered both systematic uncertainties in the recommended values of tissue compositions and individual (statistical) uncertainties. As to the second part, the CT imaging uncertainties, our estimates did agree with theirs.

Recently, Trofimov *et al.* (2010) estimated that the relative range uncertainty for prostate cancer patients was less than 2.5%. They used the values suggested by Schaffner and Pedroni (1998), i.e., 1.1% and 1.8% for soft tissues and bone tissues, respectively, and added 1% on top of that to account for scanner calibration uncertainties. They studied 10 prostate cancer patients and concluded that the relative range uncertainties were less than 2.5%. Our final estimated value of the total uncertainty is close to their estimate.

Table 20. Comparison of our estimates of the relative range uncertainties (SPR related) and the estimates from the literature.

Uncertainty Sources		Relative Range Uncertainties							
		Our Estimation (2σ)			Moyers <i>et al</i>	Schaffner <i>et al</i>		Trofimov <i>et al</i>	
		Lung	Soft	Bone		Soft	Bone	Soft	Bone
Inherent uncertainty in the presence of human tissue composition variations		0.4%	2.0%	3.0%	1.6%	1%		Based on Schaffner's estimates	
CT#	Modeling errors in predicted CT numbers	7.5%	1.5%	1.1%					
Related	CT imaging uncertainties	6.7%	1.1%	3.1%		2.5%	0.5%		
SPR Related	Uncertainties in mean excitation energies	0.2%	0.6%	0.7%	1%	n/a		1%	
	SPR variations with proton energy	0.3%		0.8%	1.2%				
	Uncertainties in proton ranges in water	n/a			1%				
Total		10.1%	2.9%	4.5%	3.5%	1.1%	1.8%	2.1%	2.8%
								2.5%	

3.4.2 Measures to Mitigate Uncertainties in Current Practice

In this section, the possible measures to mitigate range uncertainties in current practice are discussed.

The first method is related to the proton energy assumed in the treatment planning system. We found that the relative uncertainties in range calculation could be reduced by using SPRs at 100 MeV instead of 175 MeV for dose calculation, especially for tumors with the distal end shallower than 20 cm WET from the skin surface (Fig. 18). This change would reduce the relative uncertainty from 0.18% and 0.48% to 0.05% and 0.17% for the adipose tissue and cortical bone of 10 cm WET, respectively. If assuming that the typical tumor depth is about 20 cm WET, the initial proton energy required to reach that depth is about 200 MeV, according to Fig. 16. As shown in Table 19, the SPR changes monotonically with energy (decreases for adipose tissue and increases for cortical bone). Therefore, it is logical to choose an energy that is in the middle of the initial energy and the end energy to minimize errors. In our case, the initial energy is about 200 MeV and the end energy is 0 MeV thus the energy in the middle will be 100 MeV. As shown in Fig. 18(a), this change results in minimizing the relative range error – less than 0.1% for both the adipose tissue and cortical bone of 20 cm WET.

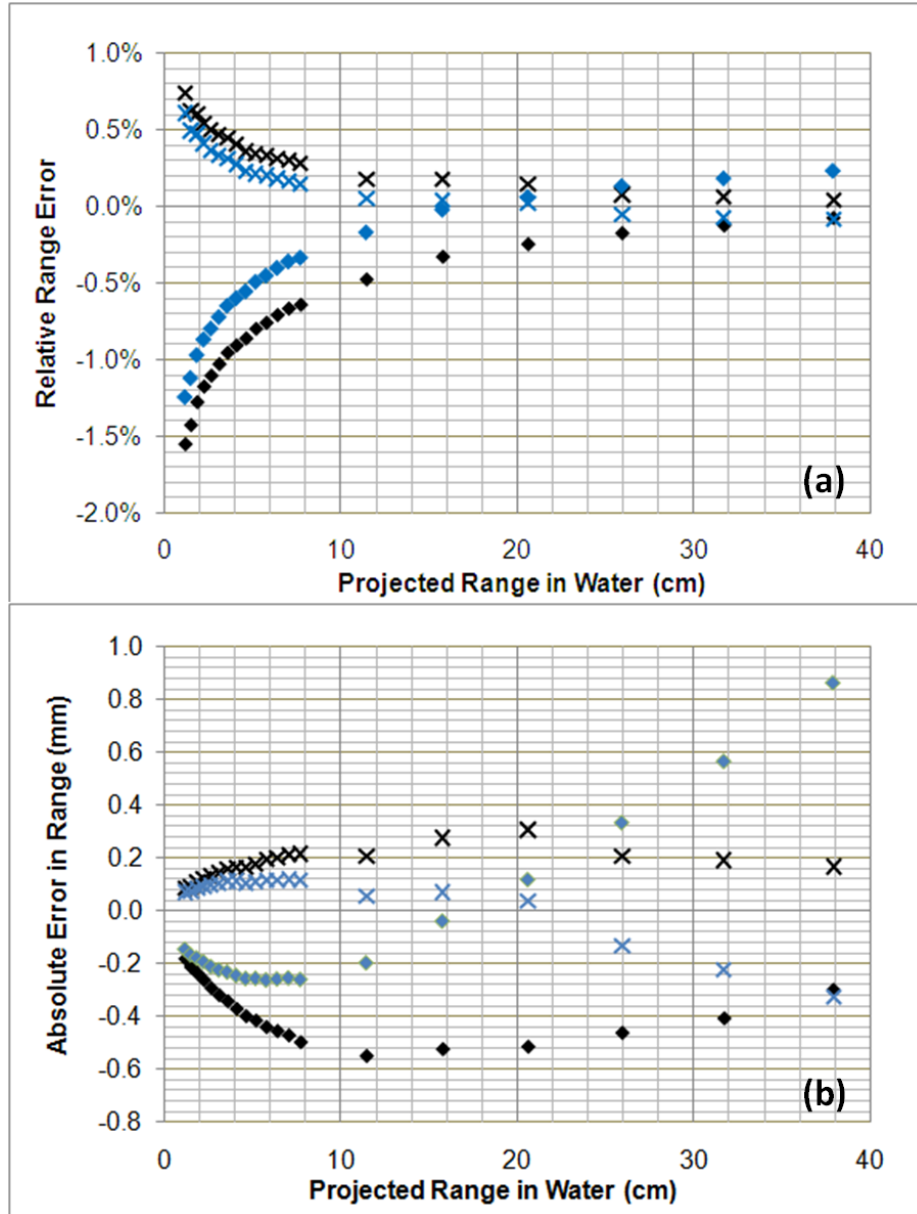


Figure 18. (a) relative and (b) absolute error in proton range calculation induced by using SPRs of 175 MeV (black) and 100 MeV (blue), respectively, versus the projected range in water for the adipose tissue (x) and cortical bone (♦).

The second method is a patient-specific calibration, which was also referred to as the patient-specific scaling by Moyers *et al.* (2009). The essence of this technique is to scan patients together with some reference materials and use the CT numbers of these

reference materials to calibrate patient images based on their CT numbers measured at reference conditions. For example, Moyers *et al.* chose air and water as the reference materials and determined a rescale ratio by comparing the CT numbers of air and water in patient CT images and their theoretical values – 0 and 1000. The rescale ratio would then be applied to patient images. This technique can reduce CT number variations caused by patient size, especially for lung tissues. But this technique requires the presence of air and water in patient images and the knowledge of their location in the images. Air is always present surrounding patients. Water can sometimes be found in patient CT images, e.g., water in a rectal balloon, urine in the bladder, etc. Besides, a small water tube can be intentionally placed adjacent to patients during scanning. We found that this technique could reduce CT number variations caused by patient size (1σ) from 2.6%, 0.42% and 1.3%, to 0.42%, 0.25% and 0.93% for lung tissues, soft tissues and bone tissues, respectively. This technique can be extended to include bone tissues by putting a small insert of cortical bone or other similar high-Z materials adjacent to patients during the scan and using its CT number to rescale CT numbers of bone tissues. In this way, CT number variations of bone tissues were found to be reduced further down from 0.93% to 0.07%. After applying this technique, the total uncertainty in SPR calculation was reduced from 5.1%, 1.6% and 2.4% to 4.3%, 1.5% and 2.0% for lung tissues, soft tissues and bone tissues, respectively.

CHAPTER 4: SPECIFIC AIM II – DEVELOPMENT OF THE DECT METHOD

4.1 Introduction

Specific Aim II: To develop a two-parameter model and a computational method for using the DECT scan to derive proton SPRs of human tissues.

The goal of this aim is to develop a method to calculate SPRs from DECT images, which is necessary for the final goal of this research project. This eventually leads to the reduction of uncertainties in SPR estimation. The key finding, which enabled us to achieve this aim, was the discovery of an empirical relationship existing between mean excitation energies and effective atomic numbers (EANs) of ‘reference’ human body tissues (Table 2).

This chapter starts with a description of the two-parameter model of calculating EDR and EAN from CT numbers obtained with two different energies. Then our DECT method of deriving SPR from EDR and EAN based on the empirical relationship is described. Lastly, the results of the DECT method’s accuracy in estimating SPRs for human body tissues under different conditions are presented, with a discussion of CT calibration for DECT calculation and our method for implementing the DECT method.

4.2 Methods and Materials

4.2.1 Two-parameter Model

The two-parameter model used in this study to calculate EDR and EAN from two CT measurements was first described by Torikoshi *et al.* (2003) for monochromatic x-rays, and later extended by Bazalova *et al.* (2008) for polychromatic x-rays, which is described in detail below.

The elemental linear attenuation coefficient (μ) for monoenergetic x-rays with peak energies below 1.02 MeV can be calculated by

$$\mu = \rho_e [Z^4 F(E, Z) + G(E, Z)] \quad , \quad (15)$$

where ρ_e , Z , and E , are the electron density, atomic number, and x-ray energy, respectively. The terms $\rho_e Z^4 F(E, Z)$ and $\rho_e G(E, Z)$ describe the photoelectric interaction and the combined effects of Compton interaction and coherent interaction, respectively. In this study, the values of $F(E, Z)$ and $G(E, Z)$ were interpolated based on the photoelectric and scattering cross section data from the XCOM database provided by the NIST (Berger *et al.*, 2005).

The linear attenuation coefficient of a composite material for polyenergetic x-rays with peak energies below 1.02 MeV can be calculated by

$$\langle \mu \rangle = \rho_e \sum_{i=1}^N w_i [Z_x^4 F(E_i, Z_x) + G(E_i, Z_x)] \quad , \quad (16)$$

where w_i is the weighting factor of E_i , and Z_x is the EAN of the composite material.

Combining Eq. 2 and Eq. 16 yields the equation below

$$\frac{HU'}{1000} = \frac{\rho_{e,x} \sum_{i=1}^N w_i [Z_x^4 F(E_i, Z_x) + G(E_i, Z_x)]}{\rho_{e,w} \sum_{i=1}^N w_i [Z_w^4 F(E_i, Z_w) + G(E_i, Z_w)]} \quad . \quad (17)$$

Eq. 17 can be rearranged and expressed by

$$\frac{HU'}{1000} = \frac{\rho'_{e,x}}{A_{w,k}} \times [SumF(Z_x) \times Z_x^4 + SumG(Z_x)] \quad , \quad (18)$$

where $A_w = \sum_{i=1}^N w_i [Z_w^4 F(E_i, Z_w) + G(E_i, Z_w)]$, $SumF(Z_x) = \sum_{i=1}^N w_i F(E_i, Z_x)$ and $SumG(Z_x) = \sum_{i=1}^N w_i G(E_i, Z_x)$.

The two unknowns in Eq. 18, $\rho'_{e,x}$, and Z_x , are solvable if two CT measurements are provided. Because $SumF(Z_x)$ and $SumG(Z_x)$ does not strongly depend on Z_x , Z_x^4 can be solved iteratively by

$$Z_x^4 = \frac{\mu'_{x,H} \times A_{w,H} \times SumG(Z_x)_L - \mu'_{x,L} \times A_{w,L} \times SumG(Z_x)_H}{\mu'_{x,L} \times A_{w,L} \times SumF(Z_x)_H - \mu'_{x,H} \times A_{w,H} \times SumF(Z_x)_L}, \quad (19)$$

where $\mu'_x = \frac{HU'_x}{1000} = \frac{\langle \mu_x \rangle}{\langle \mu_{water} \rangle}$. The DECT method involves two x-ray beams with different spectra. In this study, the one with lower effective energy is referred to as the low-energy x-ray beam (denoted by subscript L), while the one with higher effective energy is referred to as the high-energy x-ray beam (subscript H). $\rho'_{e,x}$ can be calculated from Z_x by

$$\rho'_{e,x} = \frac{\mu'_{x,L} \times A_{w,L} \times SumF(Z_x)_H - \mu'_{x,H} \times A_{w,H} \times SumF(Z_x)_L}{SumF(Z_x)_H \times SumG(Z_x)_L - SumF(Z_x)_L \times SumG(Z_x)_H}. \quad (20)$$

A MATLAB (The Mathworks, Natick, MA) program was developed to solve Eq. 19 iteratively and to calculate EAN and EDR. The program inputs include CT spectra, measured CT numbers, and elemental photon attenuation coefficients from the NIST XCOM database (Berger *et al.*, 2005). The same calculation can be performed for every pair of CT pixels on DECT images, which will result in a map of EDR and EAN. The DECT calculation for different CT voxel pairs is completely independent from each other, so it can be done in parallel easily.

4.2.2 Our DECT Method of Deriving SPRs from EDRs and EANs

As shown in Section 3.2.2.2, proton SPRs can be calculated by the Bethe-Bloch equation. According to the equation, the two variables needed to derive the SPR of protons with certain energy are EDR and mean excitation energy ($\ln I_m$). The EDR is a direct output of the DECT calculation. One problem remains: how to determine $\ln I_m$ from another output of the DECT calculation, EAN.

In order to solve the problem, we calculated $\ln I_m$ and EANs for all ‘reference’ human body tissues listed in Table 2 and plotted them in Fig. 19. $\ln I_m$ was calculated based on the Bragg additivity rule:

$$\ln I_m = \frac{\sum_{i=1}^N \frac{\omega_i Z_i}{A_i} \times \ln I_{m,i}}{\sum_{i=1}^N \frac{\omega_i Z_i}{A_i}}, \quad (21)$$

where A_i , $I_{m,i}$, Z_i , ω_i and N are the atomic number, mean excitation energy, atomic mass, mass weight of the i^{th} element, and the number of elements in the composite material, respectively (Seltzer and Berger, 1982; Schneider *et al.*, 1996). The I_m of elements used in this study were taken from the work of Seltzer and Berger (1982). Seltzer and Berger found that I_m of composite materials calculated directly based on the measured I_m of elements are not accurate. They suggested specific values of I_m for abundant elements in human tissues such as hydrogen, carbon, oxygen, nitrogen and fluorine, which should be used to calculate accurate I_m for composite materials. For other elements, they suggested a 13% rule, i.e., increasing the I_m -values measured at condensed phase by 13%.

The EAN of a composite material can be calculated by

$$EAN = \sqrt[E]{ \left(\sum_{i=1}^N \frac{\omega_i Z_i}{A_i} Z_i^E \right) / \left(\sum_{i=1}^N \frac{\omega_i Z_i}{A_i} \right) } . \quad (22)$$

The value of E in Eq. 22 was chosen to be 3.3, which minimized the difference between the EANs of the ‘reference’ human body tissues calculated using Eq. 22 and the ones calculated through the DECT calculation. Clearly shown in Fig. 19, human tissue data points are broken into two groups, one comprises only soft tissues and the other only bone tissues. A good linear relationship exists between $\ln I_m$ and EANs for human tissues within one group, except the thyroid which consists of 0.1% iodine. The thyroid was not included for linear regression of soft tissues. Based on the linear relationships, the value of $\ln I_m$ of any human body tissue can be derived from its EAN value. When both EDR and $\ln I_m$ are known, the SPR can be calculated using the Bethe-Bloch equation.

In this study, the EDR and EAN calculated from two CT numbers using Eqs. 19 and 20 are referred to as the “estimated EDR and EAN”, respectively. The mean excitation energy determined from the estimated EAN based on the empirical relationship is referred to as the “estimated mean excitation energy”. The SPR calculated based on the estimated EDR and mean excitation energy using the Bethe-Bloch equation is referred to as the “estimated SPR”. The EDR, EAN, and mean excitation energy calculated directly from material composition information using Eqs. 4, 22, and 21 are referred to as the “true EDR”, “true EAN”, and “true mean excitation energy”, respectively. The SPR calculated from the true EDR and mean excitation energy using the Bethe-Bloch equation is referred to as the “true SPR”.

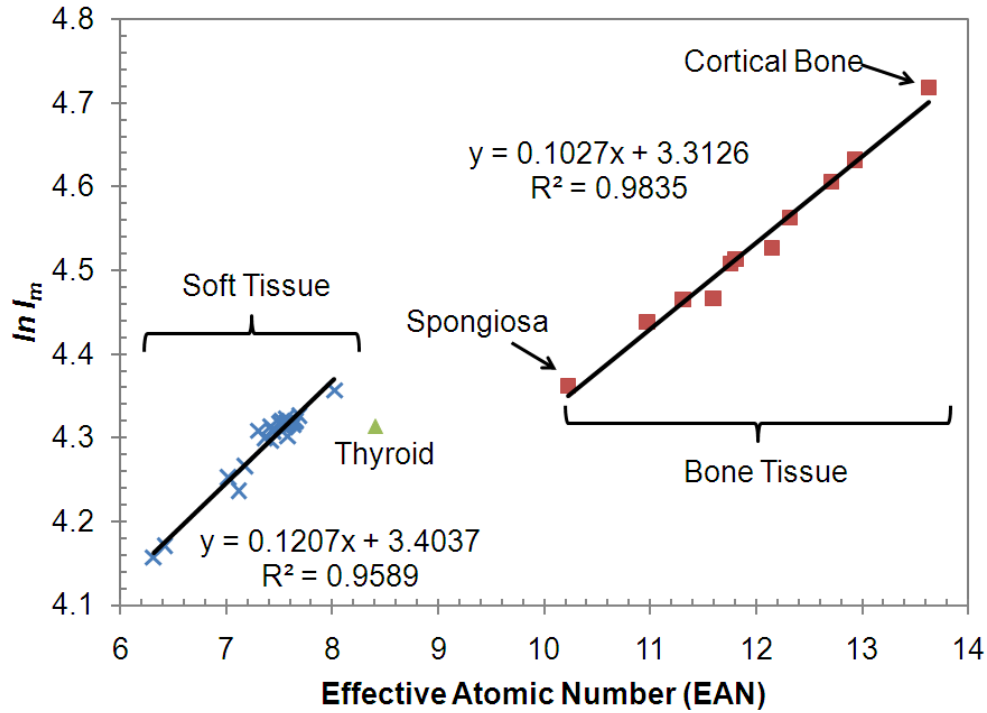


Figure 19. The soft tissue group and bone tissue group had separate linear relationships between the effective atomic number (EAN) and the logarithm of mean excitation energy ($\ln I_m$). Shown are plots for 41 ‘reference’ human body tissues listed in Table 2.

4.3 Results

We developed a Matlab program that can calculate the EDR and EAN simultaneously from two CT numbers. We also discovered an empirical relationship between EANs and mean excitation energies of the ‘reference’ human tissues listed in Table 2. These two developments enabled us to derive protons SPRs of human tissues by using DECT.

In the following, the accuracy of our DECT Matlab program was first tested when calculating EDRs and EANs for human body tissues. Then, its accuracy was tested for deriving SPRs of human body tissues and compared with the stoichiometric

method. In this part, true CT numbers were used as inputs to the DECT calculation program so that we could know the ideal accuracy of the DECT method and the comparison would be focused on the methods themselves.

4.3.1 Accuracy of EDR and EAN Calculation

The EDRs and EANs calculated using the DECT method for the ‘reference’ human body tissues were compared with the true EDRs and EANs calculated based on their composition information using Eq. 4 and 22. Figure 20 shows that the relative errors in calculated EANs and EDRs are less than 1% and 0.5%, respectively, for all tissues except the thyroid and cortical bone.

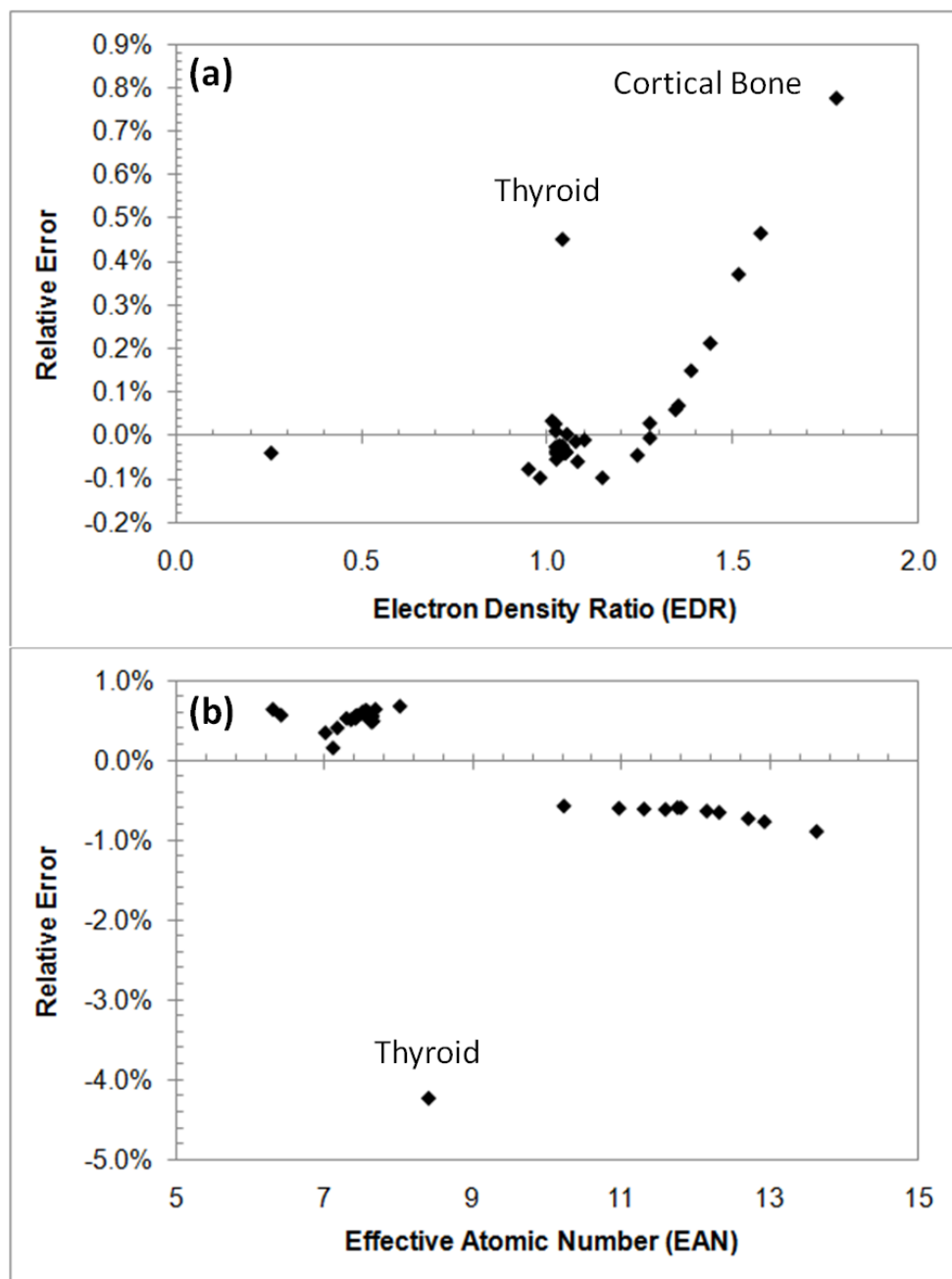


Figure 20. Relative errors in EANs and EDRs of the ‘reference’ human body tissues calculated using our DECT Matlab program.

4.3.2 Accuracy of SPR Derivation

In the following section, the estimated SPRs were compared with the true SPRs for the ‘reference’ human body tissues and human body tissues with variations introduced to the recommended densities and elemental compositions as described in Section 3.2.3.1.

4.3.2.1 ‘Reference’ Human Tissues

Figure 21 shows that both methods can achieve high accuracy in estimating SPRs of the ‘reference’ human body tissues with the RMS error well below 1%. Nonetheless, the DECT method’s accuracy is still higher than the stoichiometric method: the maximum (MAX) and RMS uncertainties of the DECT method are 1.01% and 0.24%, respectively, compared to 2.96% and 0.65% of the stoichiometric method.

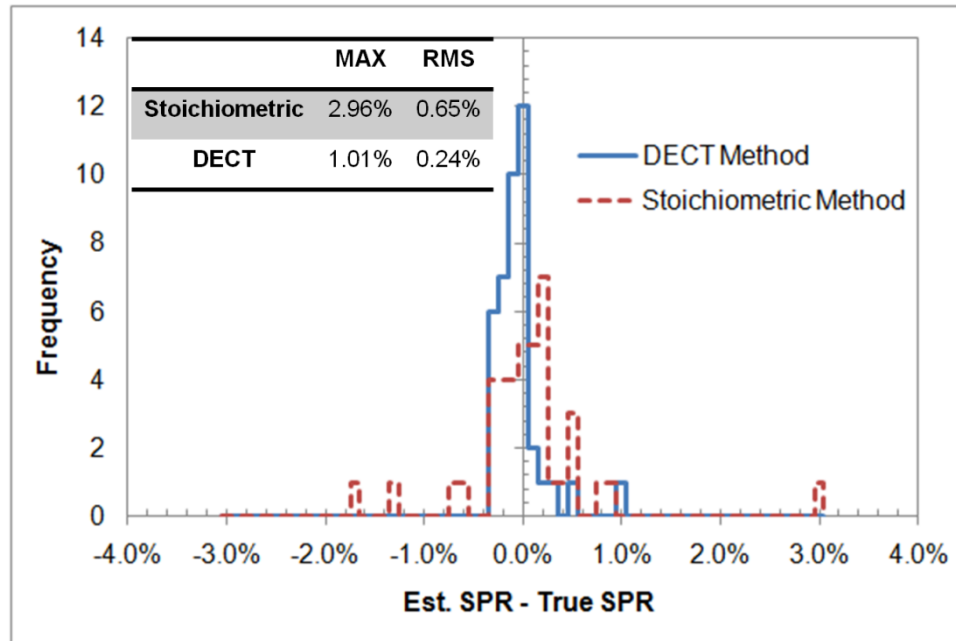


Figure 21. Histograms of relative uncertainties in proton SPRs of the ‘reference’ human tissues estimated using the DECT method and the stoichiometric calibration method, respectively.

4.3.2.2 *Single Tissue Composition Variations*

Separate variations were introduced to the densities and elemental compositions of the ‘reference’ human body tissues listed in Table 2. For simplicity, the density and elemental composition were assumed to be independent from each other. The variation scheme for the density was simple. The original value was either increased or decreased by a certain percentage. For the elemental composition, the variation scheme was more complex. First, three elements with the highest weight were identified for each tissue. Oxygen (O) and carbon (C) were most abundant by weight in all tissues. Hydrogen (H) is the third most abundant element in soft tissues, while calcium (Ca) is in bone tissues except for the spongiosa tissue which contains more hydrogen (8.9% by weight) than calcium (7.5% by weight). However, we still decided to vary the percentage of calcium instead of hydrogen for the spongiosa tissue to be consistent. Second, one element was chosen from those top three elements and its percentage was added or subtracted by a certain percentage. To keep the total percentage constant at 100, one of the remaining two elements was chosen, and its percentage was changed by the same value as the first element in the opposite direction.

Figure 22 shows how the uncertainties in SPR estimates change when variations are introduced one key quantity at a time. The accuracy of the DECT method is less sensitive to single component variation than the stoichiometric method. The uncertainties in the estimated SPRs increase with the deviations from the ‘reference’ human tissues. Generally, the increase for the stoichiometric method is more linear than that for the DECT method. Figure 22(a) shows that the accuracy of SPRs estimated using the DECT method is totally immune to the density variation, while the accuracy

becomes substantially worse for the stoichiometric method. The RMS error in the stoichiometric method increases from 0.6% to 1.4% as the relative variation in density increases from 0% to 4%. This feature of the DECT method can yield high clinical benefits because density variations are commonly seen in human body tissues with different ages or stature. The accuracy of SPR estimates has almost no dependence on the percentage change between C and O for both methods (Fig. 22(b)). This is possibly due to the fact that C and O have similar characteristics.

Overall, for the stoichiometric method, the variations applied to the weight percentages of Ca and H caused the largest impact on the SPR estimates, followed by density variations. For the DECT method, the variations to H had the largest impact, followed by the variations to Ca. The DECT method achieved higher accuracy at all levels, compared to the stoichiometric calibration method.

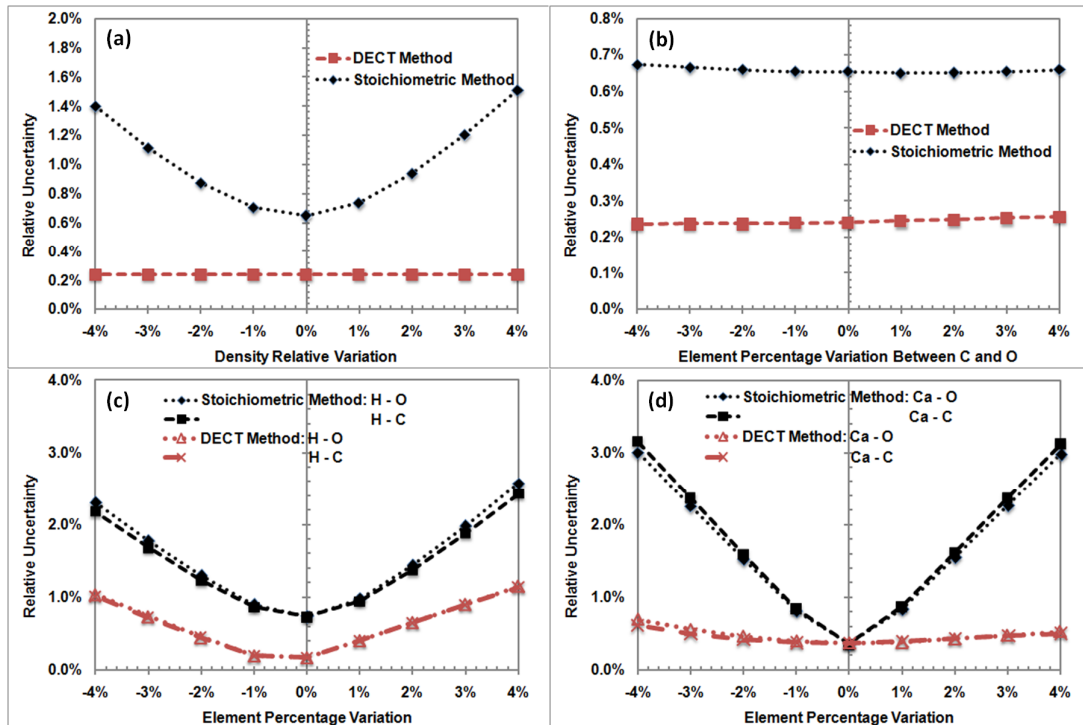


Figure 22. Uncertainties in SPRs derived using the stoichiometric and DECT method, respectively, when different levels of variations were introduced to (a) the density, (b) the percentage of the oxygen (O)–carbon (C) pair, (c) the percentage of the hydrogen (H)–oxygen pair and hydrogen–carbon pair and (d) the percentage of the calcium (Ca)–oxygen pair and calcium–carbon pair. The variation was relative for density while the percentage variation for elemental compositions was absolute. The percentage variation on the x -axis was introduced to the first element within each element pair, while the reverse variation was introduced to the second element, in order to keep the total percentage constant.

4.3.2.3 *‘Individualized’ Human Tissues*

Figure 23 shows the histograms of uncertainties in the SPRs of ‘individualized’ human tissues estimated using the DECT method and the stoichiometric method. The DECT method was observed to have great robustness with respect to tissue composition variations: the RMS uncertainties in the estimated SPRs increase from 0.24% for the ‘reference’ human tissues to 0.28% for the ‘individualized’ human tissues. The RMS uncertainties in SPRs derived using the stoichiometric method were found to increase from 0.65% for the ‘reference’ human tissues to 1.26% for the ‘individualized’ human tissues. The maximal uncertainty could reach 6% for the stoichiometric method, compared to 2% for the DECT method.

Overall, the DECT method has the potential to achieve higher accuracy than the conventional calibration method in estimating SPRs for patients of different ages, health conditions, etc.

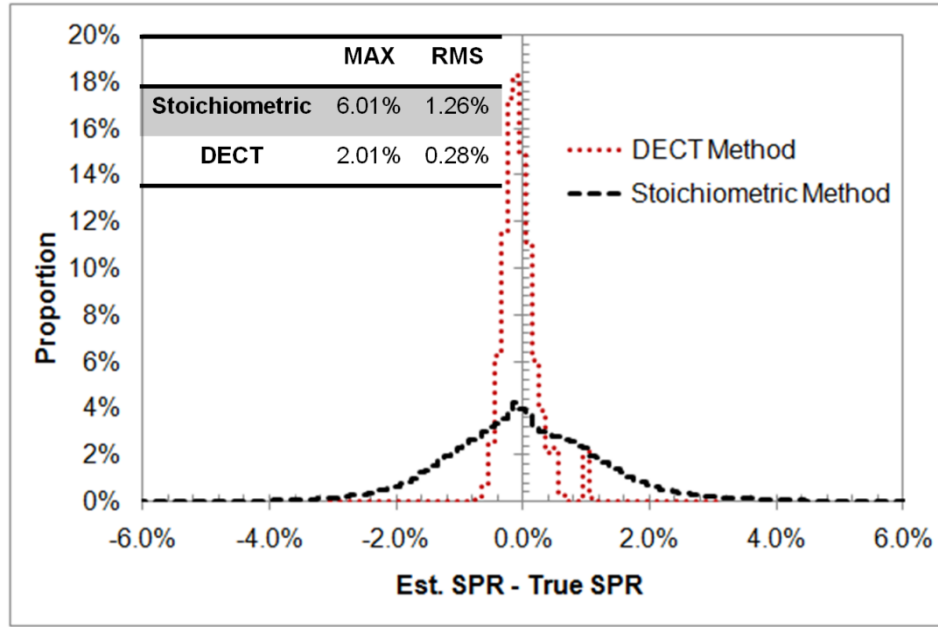


Figure 23. Histograms of relative errors in proton SPRs of the ‘individualized’ human tissues estimated using the DECT method and the stoichiometric calibration method, respectively

4.4 Discussion

4.4.1 CT Calibration for DECT Calculation

The DECT calculation algorithm requires knowledge of the x-ray spectra to model the CT scanner. The accuracy of the DECT calculation relies on the ‘closeness’ of the x-ray spectra assumed in the DECT calculation to the actual spectra. However, it is not a trivial task to determine the x-ray spectra accurately, especially when considering the beam hardening effect. In this section, we will discuss a simple and effective method to determine the x-ray spectra for the DECT calculation.

The ‘ideal’ x-ray spectra for the DECT calculation are the x-ray spectra which match the measured CT numbers completely. However, these ‘ideal’ spectra do not exist because of the beam hardening effect, which will be explained in the following

paragraphs. As a compromise, we can determine the best-match spectra first, and then determine a calibration curve to bring the measured and calculated CT numbers closer.

It is unpractical to vary the poly-energetic spectra directly to search for the ‘ideal’ spectra because of the large number of variables. Mono-energetic x-rays have only one variable and it is easy to determine the optimal energy that best matches the measured CT numbers. To take advantage of the useful feature of mono-energetic x-rays, we developed a working hypothesis that there exists a mono-energetic representation for any poly-energetic spectrum, i.e., the CT numbers of human tissues and tissue substitutes calculated based on the mono-energetic x-ray match those calculated based on the poly-energetic spectrum. If this hypothesis is true, a mono-energy should exist, which fits with the measured CT numbers equally well as the ‘ideal’ spectrum. In other words, it is only necessary to find the ‘ideal’ energy instead of the ‘ideal’ spectrum.

It is not the intent of this study to prove the hypothesis about the existence of equivalent mono-energy for any poly-energetic spectrum comprehensively. However, we did find some legitimate indications to support our hypothesis. We calculated CT numbers of various human body tissues and tissue substitutes using the simulated spectra of the 100 kVp, 140 kVp, 1MV beams. Then we calculated their CT numbers using different mono-energies to search for the best-match to each spectrum. The results were successful and we found very good matches for each poly-energetic spectrum (Fig. 24). The RMS relative differences between the CT numbers calculated based on the poly-energetic x-ray spectrum and the mono-energy counterparts were less than 0.1% for all four beams.

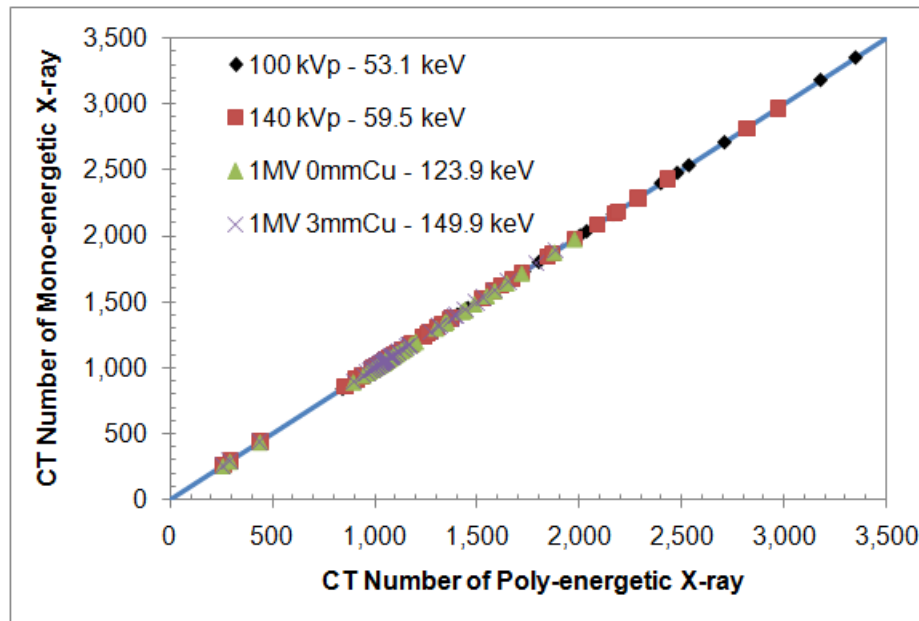


Figure 24. Comparison of CT numbers of various human body tissues and tissue substitutes calculated based on the poly-energetic x-ray beams and their equivalent mono-energetic x-ray beams.

We could not find a mono-energy that fitted the measured CT numbers of all tissue substitutes perfectly, indicating that the ‘ideal’ spectrum does not exist. Table 21 shows that the relative difference between the measured CT numbers and the calculated ones using the best-match mono-energy can still be up to 9% for lung substitutes and 3% for bone substitutes. Therefore, it is necessary to perform the calibration process (Fig. 25) to bring the measured CT numbers closer to the calculated ones. After the calibration, the relative difference became less than 1%. For comparison, we also performed the calibration process for a simulated 100 kVp spectrum (Fig. 26). After the calibration, the relative difference was still almost 4% (Table 22). It shows that the best-

match mono-energy gave better results for the DECT calculation compared to the simulated spectrum. This finding makes the DECT calculation more convenient to carry out in real clinics. Users just need to scan a few tissue substitutes to obtain the single energy that matches the measured CT numbers. This can be done without simulating or measuring the entire x-ray spectrum.

Table 21. Comparison of the calculated and measured CT numbers of various tissue substitutes for the 100 kVp beam. The calculated CT numbers were based on the best-match mono-energy (70.0 keV) to the measured CT numbers. The measured CT numbers were further adjusted using the calibration curve shown in Fig. 25 so that they match with the calculated CT numbers.

Tissue Substitutes	Cal. CT#	Meas. CT#	Rel. Diff.	Adjusted Meas. CT#	Rel. Diff.
LN-300	276	300	8.9%	276	0.2%
LN-450	434	459	5.8%	433	-0.1%
Adipose tissue	894	898	0.4%	895	0.1%
Breast	946	948	0.1%	944	-0.3%
Solid Water	1003	1009	0.6%	1004	0.1%
Water	1000	1004	0.4%	999	-0.1%
Brain	1006	1013	0.7%	1008	0.2%
Liver	1080	1085	0.5%	1079	-0.1%
B-200	1274	1291	1.4%	1258	-1.2%
CB2-30%	1507	1548	2.7%	1519	0.8%
CB2-50%	1944	1981	1.9%	1960	0.8%
Cortical Bone	2448	2449	0.0%	2436	-0.5%

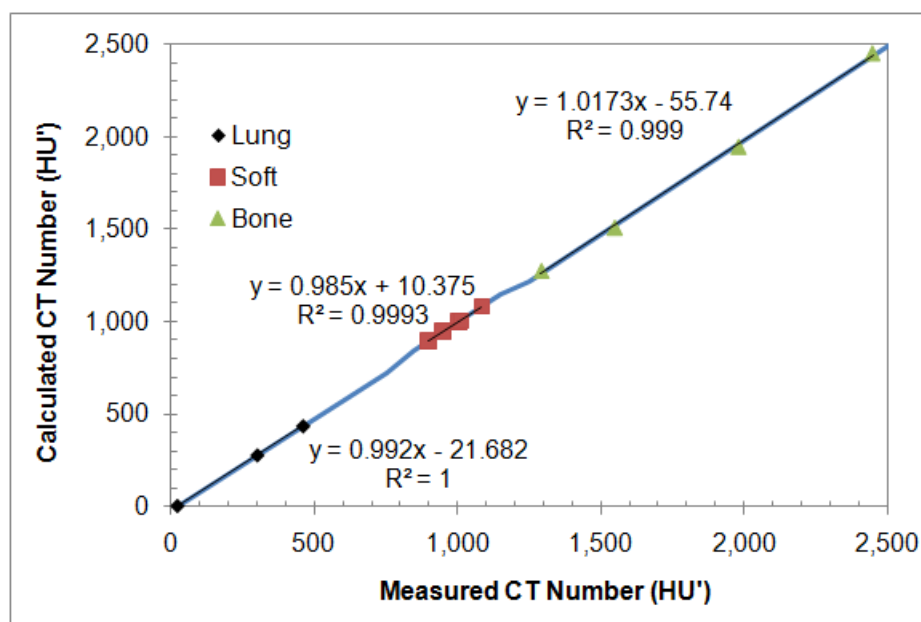


Figure 25. Linear regression fit of the calculated and measured CT numbers of various tissue substitutes for the 100 kVp beam (Table 21). The fits were carried out for lung, soft and bone tissue groups separately. The calculated CT numbers were based on the best-match mono-energy (70.0 keV) to the measured CT numbers.

Table 22. Comparison of the calculated and measured CT numbers of various tissue substitutes for the 100 kVp beam. The calculated CT numbers were based on the 100 kVp spectrum determined from Monte Carlo simulations. The measured CT numbers were adjusted using the calibration curve determined in Fig. 26 for better fitting.

Tissue Substitutes	Cal. CT#	Meas. CT#	Rel. Diff.	Adjusted Meas. CT#	Rel. Diff.
LN-300	277	300	8.5%	277	0.1%
LN-450	435	459	5.5%	435	0.0%
Adipose tissue	864	898	3.9%	867	0.3%
Breast	931	948	1.8%	925	-0.7%
Solid Water	1010	1009	-0.1%	996	-1.4%
Water	1000	1004	0.4%	991	-0.9%
Brain	970	1013	4.4%	1001	3.2%
Liver	1088	1085	-0.3%	1085	-0.3%

B-200	1426	1291	-9.5%	1377	-3.4%
CB2-30%	1723	1548	-10.2%	1769	2.7%
CB2-50%	2398	1981	-17.4%	2430	1.4%
Cortical Bone	3175	2449	-22.8%	3145	-0.9%

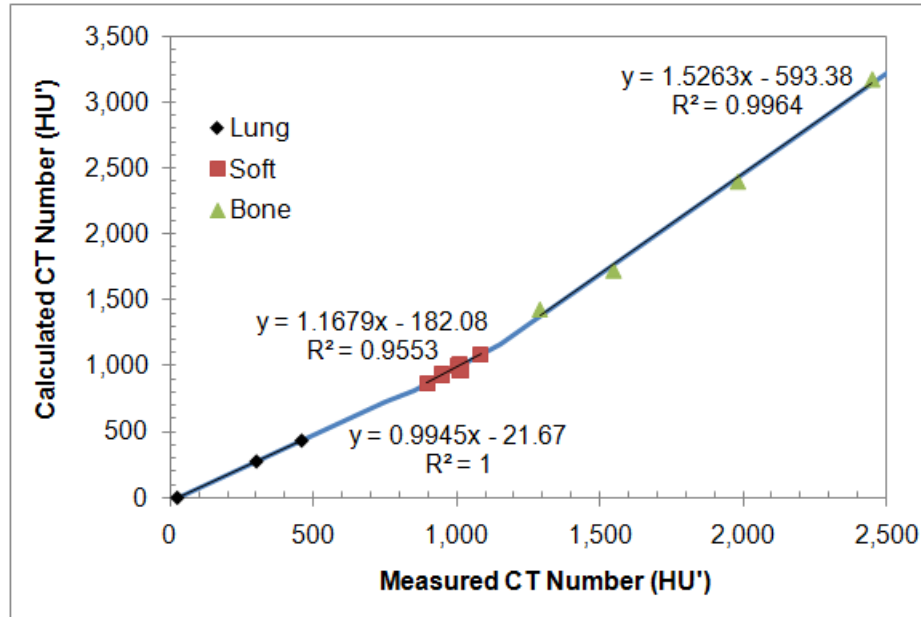


Figure 26. Linear regression fit of the calculated and measured CT numbers for various tissue substitutes using a 100 kVp beam (Table 22). The fits were carried out for lung, soft and bone tissue groups separately.

4.4.2 Our Recipe for Implementing the DECT Method

Our recipe for anyone who wants to implement the DECT calculation method for patient SPR distribution is listed below:

- 1) Scan tissue substitutes of known densities and elemental compositions using both x-ray beams of the DECT scanner. The tissue substitutes should cover the lung tissue, soft tissue, and bone tissue range.
- 2) Identify the representative mono-energy for each x-ray beam by calculating CT numbers of the tissue substitute with the highest density used in step one,

normally the cortical bone, for different x-ray energies (Eq. 2) followed by searches for the energy where the calculated CT number match the measured CT number best for that material.

- 3) Calculate CT numbers for all tissue substitutes used in step one based on the representative mono-energies determined in step two, and determine a calibration curve between the calculated CT numbers and measured CT numbers by linear regression fit within each tissue group.
- 4) Develop a DECT calculation program to calculate EDRs and EANs from two CT numbers simultaneously. The DECT calculation program is based on the mono-energies determined in step two.
- 5) Determine the empirical relationship between EAN and $\ln(I_m)$ for human body tissues (Fig. 19) and incorporate that into the DECT calculation program to derive SPR from EDR and EAN.

CHAPTER 5. SPECIFIC AIM III – DEVELOPING CRITERIA FOR SELECTING X-RAY PAIRS FOR DECT

5.1 Introduction

Specific Aim III: To develop criteria to select x-ray energy pairs for using in a DECT configuration.

This aim is necessary to investigate the impact of uncertainties in CT numbers on the accuracy of DECT calculation of proton SPRs for human body tissues. The DECT calculation of EDR and EAN is known to be sensitive to CT number variation, which can substantially compromise the theoretical benefit of the DECT method, i.e., more accurate and robust against human tissue composition variations. We hypothesized that the sensitivity of the DECT calculation to CT number variations could be minimized by choosing an appropriate x-ray pair. In search of the general criteria for selecting x-ray pairs for the DECT calculation, we started with three representative x-ray pairs. Their accuracy of estimating SPRs for human body tissues under the impact of different CT artifacts such as random noise and the beam hardening effect were compared. We then performed an uncertainty propagation analysis on the DECT calculation, and extended the comparison to mono-energetic x-ray pairs with energies ranging from 5 keV to 1 MeV. From the comparison between mono-energetic

x-ray pairs, we found the general criteria for selecting x-ray pairs for the DECT calculation. .

This chapter starts with a description of the selected representative x-ray pairs, our methods of simulating random noise and the beam hardening effect, and the uncertainty propagation analysis. Then, the results of comparisons between the representative x-ray pairs and the mono-energy x-ray pairs are presented. Lastly, the general criteria for selecting x-ray pairs for the DECT calculation and some interesting observations about the DECT calculation are discussed.

5.2 Methods and Materials

5.2.1 Selection of Three Representative X-ray Pairs

Three representative x-ray pairs were selected in this study. The first pair was a kV-kV pair consisting of a 100 kVp beam and a 140 kVp beam. The second pair was a kV-MV pair consisting of a 100 kVp beam and a 1 MV beam. The third pair was a MV-MV pair consisting of two 1 MV beams with different external filtration.

Poly-energetic x-ray spectra used in this study were generated from Monte Carlo simulations according to the x-ray tube specifications (Fig. 27). The Monte Carlo simulations were carried out using the BEAMnrc and EGSnrc Monte Carlo simulation systems provided by the National Research Council of Canada (Rogers *et al.*, 2005; Kawrakow *et al.*, 2009). The 100 kVp and 140 kVp beams were generated by simulating the x-ray tube used in the GE RT¹⁶ CT scanner (GE Healthcare, Wauwatosa, Wisconsin). The key parameters for simulating the x-ray tube were determined from the manufacture specifications (GE LightSpeed Technical Reference Manual 2007): the

target material was tungsten, the anode angle was 7° , and the equivalent filter thickness in aluminum was 7.4 mm. The spectra of the 1 MV beams were generated by simulating the compact linac made by the Varian Medical Systems (Clayton *et al.*, 2009). The x-ray beams were run through an additional 16 cm of water to simulate the spectrum change along the beam path. The average energy of the simulated spectra of the 100 kVp beam, 140 kVp beam and 1MV beams with 0mm Cu external filter and 3mm Cu external filter was 61.2 keV, 74.1 keV, 352.6 keV and 397.9 keV, respectively.

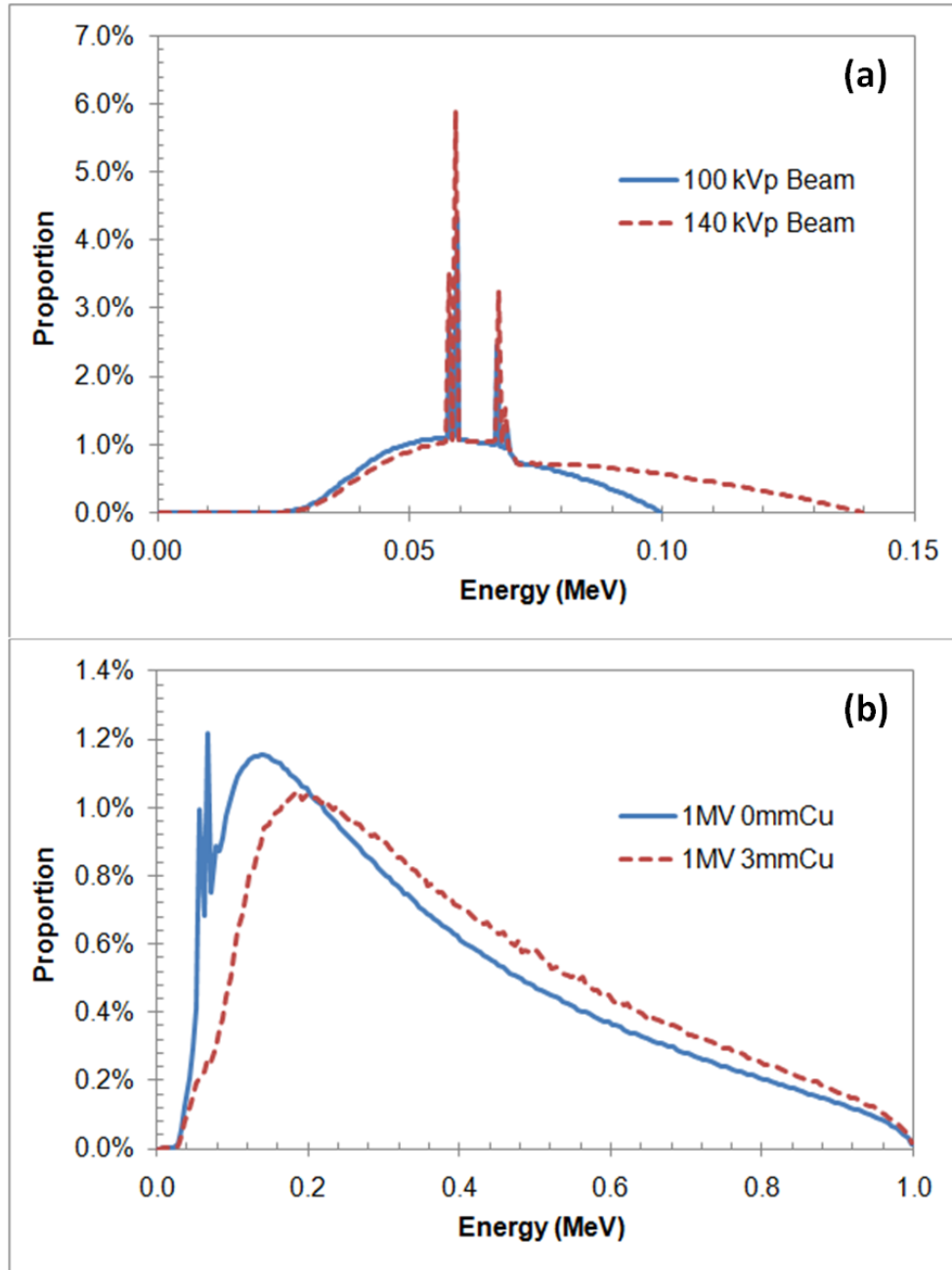


Figure 27. X-ray spectra generated for the (a) 100 kVp and 140 kVp beams and (b) 1MV 0mmCu and 1MV 3mmCu beams using the BEAMnrc Monte Carlo simulation package.

5.2.2 Simulation of Random Noise and Beam Hardening Effect

Various artifacts (e.g., random noise, beam hardening effect, metal artifact, etc.) can cause a CT measurement to deviate from its true value. The calculation of EDRs and EANs using the DECT method is known to be sensitive to CT number variations because the calculation is based on the difference between two CT measurements of the same object (Williamson *et al.*, 2006). Because of that, we were interested in investigating the accuracy of all three x-ray pairs under the impact of CT artifacts.

In this study, the random noise in CT imaging was assumed to follow the Gaussian distribution (Chvetsov and Paige, 2010). Random noise was introduced to a CT number by replacing the original value with a random number sampled from a Gaussian distribution with μ equal to the original value. The level of the noise introduced was controlled by the ratio of standard deviation (σ) to mean (μ) of the Gaussian distribution, $\frac{\sigma}{\mu}$. 1000 random numbers were sampled for each tissue type and each specific value of $\frac{\sigma}{\mu}$. The SPRs derived from the CT numbers introduced with random noise were compared to the true SPRs to quantify the impact of noise.

The x-ray spectra of both x-ray beams are required for the DECT algorithm to model the interactions in the scanning process. Because of the beam hardening effect, there is no “exact beam spectra”; instead, a set of “average spectra” were used in our DECT calculation program. The spectra detected at the center of a typical patient were regarded as the average spectra. The diameter of a typical patient was estimated to be 32 cm. Thus, the average x-ray spectra were determined by directing the x-ray through a 16 cm water slab.

Various x-ray spectra, each with a non-standard ‘hardness’, were generated by changing the thickness of the water slab from 0 cm to 32 cm. CT numbers were

calculated for the ‘reference’ human tissues based on those spectra. The SPRs derived from those CT numbers were compared to the corresponding true SPRs.

5.2.3 Uncertainty Propagation

The Bethe-Bloch equation can be rewritten as

$$\rho'_{s,x} = \rho'_{e,x} * \frac{A - \ln I_{m,x}}{B} \quad , \quad (23)$$

where $A = \ln[2m_e c^2 \beta^2 / (1 - \beta^2)] - \beta^2$ and $B = \ln[2m_e c^2 \beta^2 / I_{m,w} (1 - \beta^2)] - \beta^2$.

Their values were calculated to be 12.8 and 8.45, respectively, for proton energy equal to 175 MeV. The value of the mean excitation energy of water ($I_{m,w}$) used in this study was 75 eV. According to the empirical relationship shown in Fig. 19, the $\ln I_{m,x}$ of a human tissue can be derived from its EAN (Z_x) by

$$\ln I_{m,x} \approx C * Z_x + D \quad . \quad (24)$$

For soft tissues, C and D were calculated to be 0.121 and 3.40 while they were 0.103 and 3.31 for bone tissues. After substituting $\ln I_{m,x}$ with Eq. 24 and performing differential derivative, Eq. 23 becomes

$$\frac{d\rho'_{s,x}}{\rho'_{s,x}} = \frac{d\rho'_{e,x}}{\rho'_{e,x}} - \frac{C * dZ_x}{(A - D) - C * Z_x} \quad . \quad (25)$$

The factor $\frac{C}{(A-D)-C*Z_x}$ was found to be near constant within each tissue group, with the relative standard deviations of 0.6% for soft tissues and 1.2% for bone tissues. Thus, Eq. 25 can be rewritten as

$$\frac{d\rho'_{s,x}}{\rho'_{s,x}} = \frac{d\rho'_{e,x}}{\rho'_{e,x}} - E * dZ_x \quad , \quad (26)$$

where E is equal to 1.43% and 1.21% for soft tissues and bone tissues, respectively.

Our next step was to study the uncertainty propagation in the DECT calculation of EDRs and EANs. After differentiation, Eq. 19 becomes

$$dZ_x = \left(\frac{d\mu'_{x,L}}{\mu'_{x,L}} - \frac{d\mu'_{x,H}}{\mu'_{x,H}} \right) \times \frac{\frac{\mu'_{x,L}}{\mu'_{x,H}} \times \frac{A_{w,L}}{A_{w,H}} \times [SumF(Z_x)_L \times SumG(Z_x)_H - SumF(Z_x)_H \times SumG(Z_x)_L]}{4 \left[SumF(Z_x)_L - \frac{\mu'_{x,L}}{\mu'_{x,H}} \times \frac{A_{w,L}}{A_{w,H}} \times SumF(Z_x)_H \right]^{5/4} \times \left[\frac{\mu'_{x,L}}{\mu'_{x,H}} \times \frac{A_{w,L}}{A_{w,H}} \times SumG(Z_x)_H - SumG(Z_x)_L \right]^{3/4}} \quad (27)$$

After differentiation, Eq. 20 becomes

$$\begin{aligned} \frac{d\rho'_{e,x}}{\rho'_{e,x}} &= \frac{d\mu'_{x,L}}{\mu'_{x,L}} \times \frac{SumF(Z_x)_H}{SumF(Z_x)_H - \frac{\mu'_{x,H}}{\mu'_{x,L}} \times \frac{A_{w,H}}{A_{w,L}} \times SumF(Z_x)_L} \\ &+ \frac{d\mu'_{x,H}}{\mu'_{x,H}} \times \frac{-\frac{\mu'_{x,H}}{\mu'_{x,L}} \times \frac{A_{w,H}}{A_{w,L}} \times SumF(Z_x)_L}{SumF(Z_x)_H - \frac{\mu'_{x,H}}{\mu'_{x,L}} \times \frac{A_{w,H}}{A_{w,L}} \times SumF(Z_x)_L} \end{aligned} \quad (28)$$

After substituting dZ_x and $\frac{d\rho'_{e,x}}{\rho'_{e,x}}$ with Eqs. 27 and 28, Eq. 26 becomes

$$\frac{d\rho'_{s,x}}{\rho'_{s,x}} = R_L * \frac{d\mu'_{x,L}}{\mu'_{x,L}} + R_H * \frac{d\mu'_{x,H}}{\mu'_{x,H}} \quad , \quad (29)$$

where $R_L = FuncA - E * FuncB$, $R_H = FuncA - E * FuncC$,

$$\begin{aligned} FuncA &= \frac{\frac{\mu'_{x,L}}{\mu'_{x,H}} * \frac{A_{w,L}}{A_{w,H}} * [SumF(Z_x)_L * SumG(Z_x)_H - SumF(Z_x)_H * SumG(Z_x)_L]}{4 \left[SumF(Z_x)_L - \frac{\mu'_{x,L}}{\mu'_{x,H}} * \frac{A_{w,L}}{A_{w,H}} * SumF(Z_x)_H \right]^{5/4} * \left[\frac{\mu'_{x,L}}{\mu'_{x,H}} * \frac{A_{w,L}}{A_{w,H}} * SumG(Z_x)_H - SumG(Z_x)_L \right]^{3/4}}, \\ FuncB &= \frac{SumF(Z_x)_H}{SumF(Z_x)_H - \frac{\mu'_{x,H}}{\mu'_{x,L}} * \frac{A_{w,H}}{A_{w,L}} * SumF(Z_x)_L} \quad \text{and} \quad FuncC = \frac{SumF(Z_x)_L}{\frac{\mu'_{x,L}}{\mu'_{x,H}} * \frac{A_{w,L}}{A_{w,H}} * SumF(Z_x)_H - SumF(Z_x)_L} \end{aligned}$$

The factors R_L and R_H are termed as the sensitivity ratio factors in this study, and can be calculated for each human tissue if the tissue composition and the DECT x-ray spectra are known. Finally, the uncertainties in SPRs can be determined by

$$\frac{\sigma_{\rho'_{s,x}}}{\rho'_{s,x}} = \sqrt{\left(R_L * \frac{\sigma_{\mu'_{x,L}}}{\mu'_{x,L}}\right)^2 + \left(R_H * \frac{\sigma_{\mu'_{x,H}}}{\mu'_{x,H}}\right)^2} . \quad (30)$$

5.3 Results

5.3.1 Comparison of Three Representative X-ray Pairs

5.3.1.1 *Tissue Composition Variations*

All three x-ray pairs achieved similar accuracy in deriving SPRs for both the ‘reference’ human body tissues and ‘individualized’ human body tissues when theoretical CT numbers were used as the input for the DECT calculation (Fig. 28). The theoretical CT numbers were calculated based on the x-ray spectra stored in the DECT calculation program. In this case, the DECT calculation program modeled the ‘virtual’ CT scanner perfectly. Under this ideal condition, the selection of the x-ray pairs had negligible impact on the accuracy of SPR estimation.

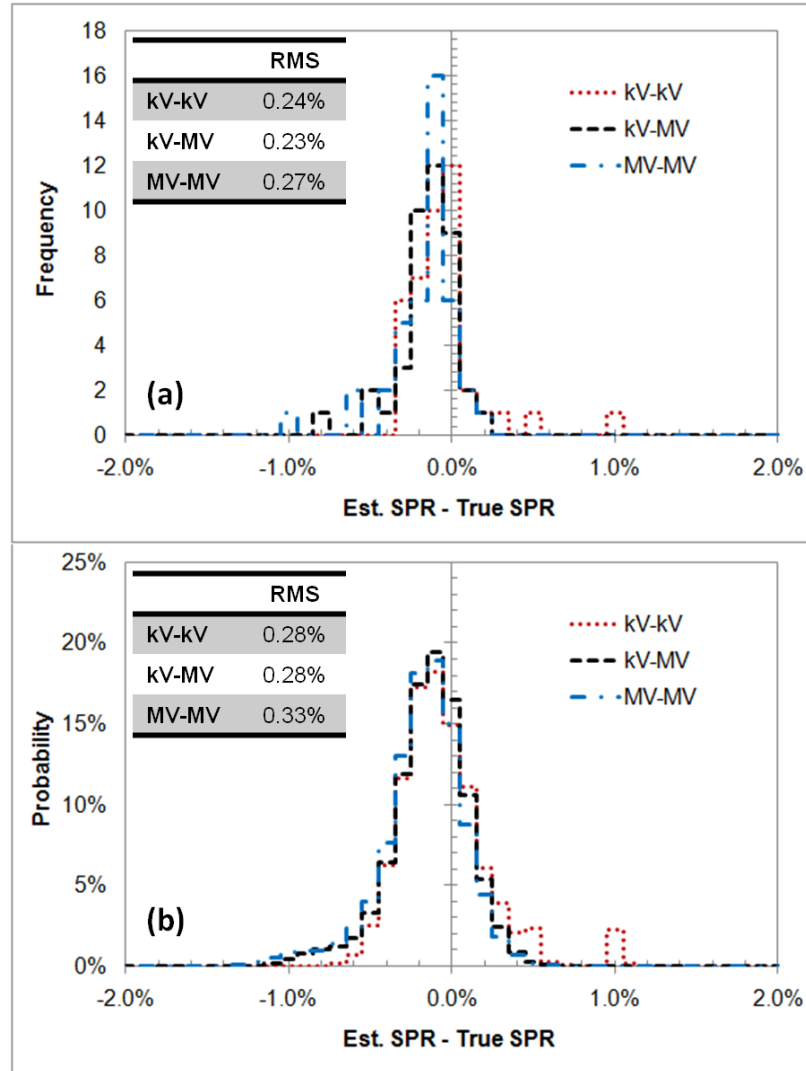


Figure 28. Histograms of the relative errors in SPRs estimated using the kV-kV, kV-MV, and MV-MV DECT for the (a) ‘reference’ human body tissues and (b) ‘individualized’ human body tissues. The RMS error was calculated to describe the overall magnitude of uncertainty distribution. The results showed that, under ideal conditions (i.e., without imaging artifacts), the uncertainties in the DECT calculation were independent of the x-ray energy pairs.

5.3.1.2 *Random Noise*

The uncertainties in estimated SPRs increased with random noise linearly for all three energy pairs (Fig. 29). The sensitivity of RMS errors to random noise was 6.76,

1.16, and 6.28 for the kV-kV, kV-MV, and MV-MV pairs, respectively. The SPR estimation was substantially less sensitive to random noise when using the kV-MV pair than that using the other two pairs.

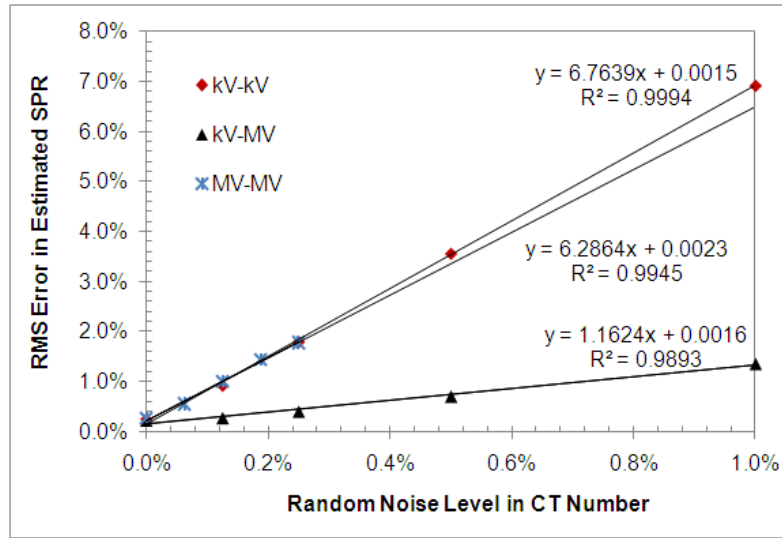


Figure 29. Dependence of the RMS errors in SPRs estimated using the DECT method on random noise in CT numbers for the ‘reference’ human body tissues.

5.3.1.3 Uncertainty Propagation

The ratios of absolute EAN variation (dZ_x) and relative EDR variation ($\frac{d\rho'_{e,x}}{\rho'_{e,x}}$) to relative CT number variation ($\frac{d\mu'_x}{\mu'_x}$) were calculated for all three x-ray pairs according to Eqs. 27 and 28, respectively. Table 23 shows that the calculated EANs of soft tissues were more sensitive to CT number variations than those of bone tissues. The EDRs of bone tissues were similarly sensitive except for the kV-kV DECT. In addition, the EDRs were less sensitive to variations of high-energy CT numbers ($\frac{d\mu'_{x,H}}{\mu'_{x,H}}$) than

variations of low-energy CT numbers ($\frac{d\mu'_{x,L}}{\mu'_{x,L}}$) for all cases, especially for the kV-MV DECT. Overall, the DECT calculation using the kV-MV pair was the least sensitive to CT number variations among all three x-ray pairs studied.

The ratios of relative SPR variations ($\frac{d\rho'_{s,x}}{\rho'_{s,x}}$) to relative CT number variations were calculated for all three x-ray pairs based on Eq. 29. The kV-MV DECT was the least sensitive to CT number uncertainties; the sensitivity ratio factors, R_L and R_H , were at least 1/3 smaller for the kV-MV pair than those for the other two pairs. The conventional kV-kV DECT was slightly less sensitive to CT number variations than was the MV-MV DECT. R_L was smaller than 1/3 of R_H for the kV-MV DECT, indicating that it is more effective to reduce the overall uncertainties in SPRs by reducing the uncertainties in kV CT imaging than the uncertainties in MV CT imaging.

Our uncertainty propagation analysis validated the linear relationship between the random noise level in CT numbers and the RMS errors in SPRs observed in Fig 29. According to the sensitivity ratio factors listed in Table 24, a 1% random noise in low-energy CT numbers leads to a 4.14%, 0.31%, and 5.60% SPR uncertainty for the kV-kV, kV-MV, and MV-MV DECT, respectively. A 1% random noise in high-energy CT numbers leads to a 5.14%, 1.31%, and 6.56% SPR uncertainty, respectively. By adding the uncertainties from both the low-energy and high-energy CT numbers in quadrature, a 1% random noise in both CT numbers leads to a 6.58%, 1.34%, and 8.63% SPR uncertainty for the kV-kV, kV-MV, and MV-MV DECT, respectively. These agree with the corresponding values determined from simulations (Fig. 29), especially for the kV-kV and kV-MV DECT, which serves as a validation of our uncertainty propagation analysis.

Table 23. Ratios of absolute EAN variations and relative EDR variations over relative CT number variations in the DECT calculations for different x-ray energy pairs. The values were averaged of all tissue types within each tissue group.

Energy Pairs	Tissue Groups	$\frac{d\rho'_{e,x}/\rho'_{e,x}}{d\mu'_{x,L}/\mu'_{x,L}}$	$\frac{d\rho'_{e,x}/\rho'_{e,x}}{d\mu'_{x,H}/\mu'_{x,H}}$	$\frac{dZ_x}{d\mu'_{x,L}/\mu'_{x,L}}$	$\frac{dZ_x}{d\mu'_{x,H}/\mu'_{x,H}}$
kV-kV	Soft Tissue	-2.81	3.81	70.5	-70.5
	Bone Tissue	-4.30	5.30	43.8	-43.8
kV-MV	Soft Tissue	-0.06	1.06	19.6	-19.6
	Bone Tissue	-0.09	1.09	9.1	-9.1
MV-MV	Soft Tissue	-1.09	2.09	366	-366
	Bone Tissue	-1.17	2.17	118	-118

Table 24. SPR sensitivity ratio factors, R_L and R_H , calculated for all three x-ray beam pairs. The values were averaged of all tissue types within each tissue group.

Energy Pairs	Tissue Groups	$R_L(\frac{d\rho'_{s,x}/\rho'_{s,x}}{d\mu'_{x,L}/\mu'_{x,L}})$	$R_H(\frac{d\rho'_{s,x}/\rho'_{s,x}}{d\mu'_{x,H}/\mu'_{x,H}})$
kV-kV	Soft Tissues	3.82	4.82
	Bone Tissues	4.85	5.84
	All Tissues	4.19	5.18
kV-MV	Soft Tissues	0.34	1.34
	Bone Tissues	0.21	1.21
	All Tissues	0.30	1.30
MV-MV	Soft Tissues	6.36	7.35
	Bone Tissues	2.63	3.63
	All Tissues	5.38	6.34

5.3.2 Comparison of Mono-energetic X-ray Pairs

The sensitivity ratio factors, R_L and R_H , were calculated for various mono-energetic x-ray beam pairs. The energies of mono-energetic x-rays studied here ranged from 5 keV to 1 MeV with a step size of 5 keV. Generally, the SPR sensitivity to CT number variations decreased with the difference between two x-ray spectra. We

changed the energy of one beam at a time in order to demonstrate how the sensitivity changes with the beam energies.

First, the energy of the low-energy beam was set to 60 keV, the average energy of our 100 kVp x-ray, and the energy of the high-energy beam was changed from 65 keV to 1 MeV. It was noticed that R_L was always negative and R_H was always positive. In the following paragraphs of this section, when we mention the sensitivity ratio factors R_L and R_H , unless specified otherwise, we mean their absolute values because the absolute value is what matters in uncertainty propagation. Fig. 30(a) shows that both R_L and R_H decreased quickly with the energy of the high-energy beam before they reached a plateau.

Next, the high-energy component was set to the average energy of the 1 MV x-ray beam, 400 keV, and the low-energy x-ray was changed from 5 keV to 395 keV. R_L and R_H were observed to increase substantially with the energy of the low-energy beam (Fig. 30(b)). This was especially true for R_L , which increased more than 20% for every 5 keV step from 25 keV to 60 keV. This finding indicates that the energy of the low-energy beam needs to be as low as practically possible, while the energy of the high-energy beam just needs to be above a threshold value. The threshold value was observed to be about 200 keV above the effective energy of the low-energy beam. The low energy beam is dominant in determining the minimum sensitivity that is achievable. When the energy of the low energy beam is 5 keV, R_L is reduced to 0.03 while R_H only reduced to 1.03, indicating that the SPR uncertainty will become increasingly dominated by uncertainties in the high-energy CT imaging as the energy of the low-energy beam decreases.

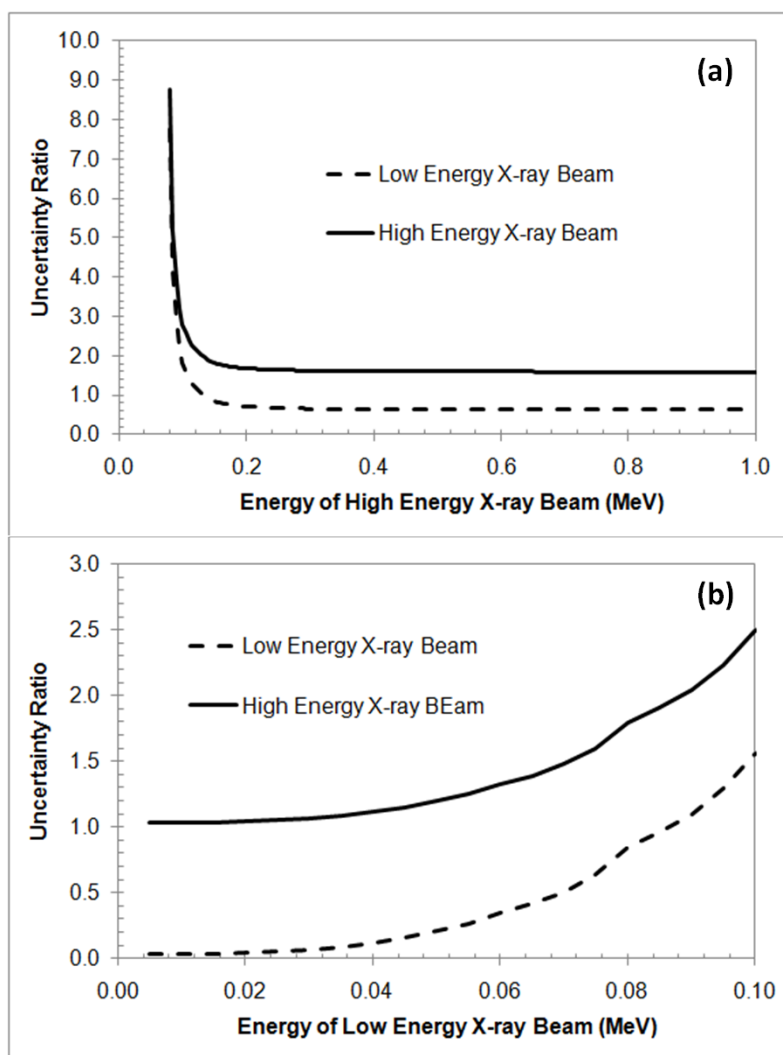


Figure 30. Relationship between the SPR sensitivity ratio factors (the absolute value of R_L and R_H) and the energy of (a) the high-energy x-ray beam and (b) the low-energy x-ray beam used for DECT scans. In (a), the energy of the low-energy x-ray beam was 60 keV, and in (b), the energy of the high-energy x-ray beam was 400 keV. Mono-energetic x-ray beams were used in these simulations.

5.4 Discussion

5.4.1 Criteria for Selecting X-ray Pairs

The kV-MV pair was the best of all three beam pairs investigated in this study because its SPR estimation was the least sensitive to CT number variations. However, our goal was to find general principles for selecting the optimum x-ray pairs for DECT calculations and to test whether there is a beam pair that is better than our kV-MV pair in terms of reducing the sensitivity ratio factors. The general principle was concluded to be: the energy of the low-energy beam needs to be made as low as practically possible while the energy of the high-energy beam needs to be at least 200 keV higher than that of the low-energy beam. The average energy of the 100 kVp and 1 MV beams of the kV-MV pair were about 60 keV and 400 keV, respectively. R_L and R_H were found to decrease from 0.648 to 0.636 and from 1.616 to 1.603, respectively, as the energy of the high-energy beam increased from 400 keV to 1 MeV. It suggests that no significant gain will be achieved by replacing the 1 MV beam with a beam with higher energy, e.g., a 6 MV therapy beam.

The key is to lower the energy of the low-energy beam in order to reduce the sensitivity of the DECT calculation to CT number variations. But the CT imaging uncertainties due to the beam hardening effect increase as the x-ray energy gets low, which competes with the reduction of the sensitivity ratio factors. The typical x-ray peak energies used in current CT scanners are 80 keV, 100 keV, 120 keV and 140 keV. In the next specific aim, both the sensitivity ratio factors and CT imaging uncertainties associated with each beam will be determined, based on which the optimal kV beam will be determined to pair with the 1 MV beam.

5.4.2 Interesting Observations about DECT Calculations

According to our uncertainty propagation analysis, the energy of the low energy x-ray beam determines the lowest achievable sensitivity ratio while the energy of the high energy x-ray beam just needs to be high enough to achieve that minimum value. The DECT calculation depends on the difference between two CT measurements of the same object. It implicitly indicates that the larger the difference is, the less sensitive the calculation will be to CT number variations. The CT number is essentially the ratio of photon linear attenuation coefficients of the object of interest relative to water. The photon linear attenuation coefficient for photons with energy below 1.02 MeV has two major components – the photoelectric absorption and Compton scatter. The cross section of photoelectric absorption depends on both the EAN and x-ray energy strongly, while that of the Compton scatter does not depend on the EAN at all and depends on the energy slightly. As the energy increases, the cross section of photoelectric interaction decreases quickly, while that of Compton scatter remains almost constant. As a result, the CT number changes from a value depending on both EDR and EAN toward a constant value that is proportional to EDR. Therefore, the maximal CT number difference between two energies depends on the lower energy, and the higher energy just needs to be high enough to reach that maximal difference. This explains how the sensitivity ratio factors change with the energy of the low energy and high energy x-ray beams.

Table 17 shows that the sensitivity ratios of EAN to CT number variations are always positive for the low energy x-ray beam, $\frac{dZ_x}{d\mu_{x,L}/\mu_{x,L}}$, while negative for the high energy x-ray beam, $\frac{dZ_x}{d\mu_{x,H}/\mu_{x,H}}$. The CT number of the low energy x-ray beam (HU'_L) depends on the EAN more strongly than the CT number of the high energy x-ray beam

(HU'_H), so the EAN calculated based on the difference of two CT numbers increases with HU'_L and decreases with HU'_H . Table 17 also shows that the sensitivity ratios of EDR over CT number variations are always negative for the low energy x-ray beam, $\frac{d\rho'_{e,x}/\rho'_{e,x}}{d\mu'_{x,L}/\mu'_{x,L}}$, while positive for the high energy x-ray beam, $\frac{d\rho'_{e,x}/\rho'_{e,x}}{d\mu'_{x,H}/\mu'_{x,H}}$. Similarly, the sensitivity ratio increases with HU'_H because HU'_H depends more strongly on the EDR compared to HU'_L . As shown in Eq. 26, the SPR variation increases with EDR variation and decreases with EAN variation. An increase of HU'_L results in an increase of EAN, a decrease of EDR, and thus a decrease of SPR. On the contrary, an increase of HU'_H leads to a decrease of EAN, an increase of EDR, and thus an increase of SPR. This explains why R_L is always negative while R_H is always positive. Fig. 30 shows that R_L approaches 0 while R_H approaches 1 as the energy of the low energy beam becomes low (0 keV to 10 keV). In that energy range, the photoelectric interaction is dominant so the CT number difference is proportional to EAN^3 . Thus, CT number variations have a limited impact on EAN calculation. The other factor, EDR, is essentially a weighted average of both CT numbers. In the energy range of 0 keV to 10 keV, the EDR calculations depend on HU'_H almost completely. Therefore, in that energy range, the variation of HU'_L has little impact on both EDR and EAN while the variation of HU'_H has little impact on EAN but large impact on EDR. This explains why R_L and R_H approaches 0 and 1, respectively, as the energy of the low energy x-ray beam becomes low.

CHAPTER 6: SPECIFIC AIM IV – ESTIMATION OF MARGIN REDUCTION BY USING DECT

6.1 Introduction

Specific Aim IV: To evaluate the margin reduction by using DECT for treatment planning.

This aim is necessary to study the clinical benefit of DECT in proton therapy and to test our hypothesis of margin reduction by a factor of 2. The uncertainties in DECT calculations were also broken down into five categories. The uncertainties were estimated for each category and each tissue group, based on which a composite range uncertainty estimate was determined for prostate, lung and head-and-neck cancer sites.

This chapter starts with a brief description of our methods of estimating the uncertainties in SPR estimation when using the DECT method. Then the measurements using four kV beams and one MV beam are presented, followed by our uncertainty estimates for the kV-MV DECT. Finally, a few interesting topics about the DECT method are discussed, such as comparison of the DECT method with the stoichiometric method, measures to improve the DECT method, practical limitations and other benefits of the DECT method.

6.2 Methods and Materials

6.2.1 Uncertainties in SPR Estimates Using the DECT Method

Similar to the stoichiometric method, the uncertainties in SPRs estimated using the DECT method were divided into 5 categories: the inherent uncertainty in the presence of human tissue composition variations, the CT modeling uncertainty, the CT imaging uncertainty, the uncertainty in mean excitation energy and the SPR variation with proton energy. The uncertainty of each category was estimated for the DECT method similar to those for the stoichiometric method. The inherent uncertainties in the presence of human tissue composition variations were estimated by comparing the SPRs derived using the DECT and the true SPRs of the ‘individualized’ human tissues. The CT modeling uncertainties were estimated by comparing the measured CT numbers and the calculated CT numbers of tissue substitute inserts. The imaging uncertainties were estimated by comparing the CT numbers of the same tissue substitutes measured under different conditions as described in Section 3.2.3.3. The CT modeling uncertainties and CT imaging uncertainties were estimated for both beams of the energy pair, based on which the induced SPR uncertainties were calculated, using Eq. 30. The SPR uncertainties due to the uncertainties in mean excitation energies and SPR variations with proton energies have the same estimated values for the DECT method and the stoichiometric method.

6.3 Results

The imaging uncertainties and modeling uncertainties were determined based on experimental measurements for four kV beams – the 80 kVp, 100 kVp, 120 kVp and 140 kVp beams, in order to determine which kV beam is the optimal one to pair with the MV beam as discussed in Section 5.4. The imaging uncertainties and modeling

uncertainties were estimated for the MV beam based on measurements using a TomoTherapy machine instead of the Varian compact linear accelerator. The equivalence of the two beams was discussed in Section 6.3.2. The overall uncertainty estimates were first determined for the kV-MV beam pair, and then the composite range uncertainty was estimated for prostate, lung and head-and-neck patients.

6.3.1 Selection of the Best kV Beam to Pair with the MV Beam

The same set of measurements as used in estimating the imaging uncertainties for the stoichiometric method was repeated for four kV beams – the 80 kVp, 100 kVp, 120 kVp and 140 kVp. Based on the measurements, the effective energies of the 80 kVp, 100 kVp, 120 kVp and 140 kVp beams were estimated to be 62.0 keV, 69.9 keV, 76.4 keV and 82.7 keV, respectively, using the method described in Section 4.4. The sensitivity ratio factors were calculated for them based on their effective energies and the effective energy of the 1 MV beam (Table 25). The sensitivity ratio factors for both the low energy and high energy beams (R_L and R_H) decrease substantially as the energy of the kV beam decreases, which agrees with our general principle found in Section 5.4. The imaging uncertainties and modeling uncertainties increases as the beam energy decreases (Table 26 and Table 27), but the decrease of both sensitivity ratio factors outcompete the increase of imaging uncertainties and modeling uncertainties. As a result, the pair of the 80 kVp – 1 MV beams was able to produce the smallest SPR uncertainties. Therefore, the 80 kVp beam was chosen to pair with the 1 MV beam. In the following, the kV-MV pair refers to the 80 kVp – 1 MV pair, unless specified otherwise.

Table 25. Sensitivity ratio factors calculated for the 80 kVp, 100 kVp, 120 kVp and 140 kVp beams, respectively, when paired with the 1 MV beam.

	Tissue Types	80 kVp	100 kVp	120 kVp	140 kVp
R_L	Lung Tissues	0.47	0.64	0.88	1.2
	Soft Tissues	0.43	0.59	0.82	1.1
	Bone Tissues	0.16	0.20	0.26	0.32
R_H	Lung Tissues	1.4	1.6	1.8	2.1
	Soft Tissues	1.4	1.6	1.8	2.1
	Bone Tissues	1.2	1.2	1.2	1.3

Table 26. Our estimates of imaging uncertainties (1σ) of the 80 kVp, 100 kVp, 120 kVp and 140 kVp beams.

Tissue Groups	Imaging Uncertainties (1σ)			
	80 kVp	100 kVp	120 kVp	140 kVp
Lung tissues	3.6%	3.5%	3.0%	2.9%
Soft Tissues	0.61%	0.63%	0.57%	0.58%
Bone tissues	2.5%	2.3%	2.1%	2.1%

Table 27. Statistics of modeling uncertainties (1σ) for the 80 kVp, 100 kVp, 120 kVp, 140 kVp beams and the MV beam of the TomoTherapy machine.

Tissue Groups	Modeling Errors (1σ)				
	80 kVp	100 kVp	120 kVp	140 kVp	TomoTherapy
Lung tissues	0.04%	0.12%	0.23%	0.08%	0.25%
Soft Tissues	0.15%	0.16%	0.15%	0.16%	0.03%
Bone tissues	1.0%	0.88%	0.71%	0.59%	0.00%

6.3.2 MV Measurements using the TomoTherapy Machine

Our estimates of the modeling errors and the imaging uncertainties for the 1 MV beam were based on the measurements using the TomoTherapy machine. The MV beam of the TomoTherapy machine has a peak energy of 3.5 MeV (Jeraj *et al.*, 2004), which is higher than our 1 MV beam. But as discussed in Section 5.4, the effective energy of our 1 MV beam is already high enough to couple with the kV beam, and further increase of the energy does not decrease the sensitivity ratio factors substantially

(less than 5%). The imaging uncertainties may be reduced further by using the 3.5 MV beam instead of the 1 MV beam. But considering that current TomoTherapy machines are not dedicated for imaging, it is reasonable to expect future dedicated MV scanners to achieve an uncertainty no worse than current TomoTherapy machines. The experimental measurements for determining the modeling errors and the imaging uncertainties for the MV beam were the same as those for the kV beams.

Table 27 lists the modeling uncertainties associated with the MV beam, which were found smaller for soft tissues and bone tissues than the kV beams, due to the dominance of the Compton interaction in the MV energy range. Table 28 lists our estimates of the imaging uncertainties for the MV beam of the TomoTherapy machine. The CT number uncertainties related to the phantom size and the position in the scan were found smaller for the MV beam than for the kV beams, especially for bone tissues. One thing to note in Table 28 is that the uncertainty estimates of the factors, the time and scanner and the couch position, for the MV beam were actually taken from our previous estimates for the kV beam. The uncertainty estimates of the factor, time and scanner, for the kV beams were based on the repeated CT measurements of the same set of tissue substitute inserts in monthly QAs. But those CT number measurements are not included in the monthly QAs of the TomoTherapy machine, because the TomoTherapy machine is not used regularly for patient treatment planning purpose. Our estimates for the couch height for the 1 MV beam were not based on the measurements of the TomoTherapy machine, because our measurements indicated that the TomoTherapy machine has not been designed to give accurate CT numbers when the couch is at different height thus it will be over-estimating to use its uncertainty values as estimates

for future dedicated MV scanners. The CT numbers measured using the TomoTherapy machine were found to vary substantially when the treatment couch was at different height. Moreover, no clear pattern was observed in CT number variations for the TomoTherapy machine, e.g., the CT number variation for water was 2% while it was only 0.2% for liver and 1% for CB2-50%. On the contrary, a clear pattern was observed for the dedicated kV CT scanner, i.e., the variations were always small for materials with CT number value close to water and the variation became larger as the difference increased. Therefore, we decided to use the uncertainty estimates of the following factors, the time and scanner and the couch position, for the kV beam when calculating the total imaging uncertainties for the MV beam, so that the comparison of the DECT method with the stoichiometric method would be fair.

Table 28. Statistics of CT number uncertainties ($1-\sigma$) due to different factors for different tissue groups for the MV TomoTherapy beam.

Tissue Groups	Major Uncertainty Contributing Factors ($1-\sigma$)				Total (RSS)
	Time and Scanner*	Patient Size	Position in the Scan	Couch Position*	
Lung	1.0%	0.69%	1.6%	1.0%	2.3%
Soft	0.33%	0.21%	0.35%	0.27%	0.59%
Bone	0.61%	0.16%	0.30%	0.46%	0.84%

*. The data of this category are from the data of the kV beam listed in Table 14.

6.3.3 Summary

Table 29 lists the summary of the uncertainties of each category estimated for the DECT with the 80 kVp – 1 MV pair. The imaging uncertainties were found to be the dominant factor for all three tissue types. The total SPR uncertainties were estimated to be 3.7%, 0.99% and 1.4% for lung, soft and bone tissues, respectively. The composite

range uncertainties calculated based on these values are 1.9%, 2.3% and 1.9% for prostate, lung and head-and-neck patients, respectively.

Table 29. Summary of our estimates of the relative SPR uncertainties ($1-\sigma$) when using the DECT with the 80 kVp – 1 MV pair.

Uncertainty Sources		Relative SPR Uncertainty ($1-\sigma$)		
		Lung	Soft	Bone
Inherent uncertainties in the presence of human tissue composition variations		0.23%	0.32%	0.43%
CT# Related	Modeling errors in predicted CT numbers	0.36%	0.08%	0.15%
	CT imaging uncertainties	3.7%	0.89%	1.0%
SPR Related	Uncertainties in mean excitation energies	0.17%	0.23%	0.65%
	SPR variations with energies	0.17%	0.17%	0.41%
Total (RSS)		3.7%	0.99%	1.4%

6.4 Discussion

6.4.1 Comparison of the DECT Method and the Stoichiometric Method

Our study shows that the kV-MV DECT can reduce the range uncertainty (Table 30) but it fails to reach our main goal, i.e., reducing the total uncertainty by a factor of two. However, our study demonstrates that the DECT method holds a possible advantage over the stoichiometric method with the extra tissue composition information.

Currently, the dominant uncertainty factor for the stoichiometric method using the kV beam is the inherent uncertainty in the presence of tissue composition variations. This uncertainty cannot be reduced because it is due to the inherent drawback of the stoichiometric method itself, i.e., the incapability of fully capture SPR variation with a single CT number. The uncertainties due to the other three factors – CT modeling

uncertainties, the uncertainties in mean excitation energy and SPR variations with proton energy cannot be reduced neither because they are all limited by the method itself. Only the CT imaging uncertainties may be reduced with the advance in CT technologies, e.g., better beam hardening correction algorithm, more stable CT imaging, etc. But the reduction of CT imaging uncertainties does not lead to substantial reduction of the total uncertainty for the stoichiometric method using the kV beam: the total uncertainty is only reduced from about 3.0% to 2.6% (Table 30) even when assuming an ideal case scenario, i.e., the CT imaging uncertainties are removed completely. On the contrary, the total range uncertainty using the kV-MV DECT can be reduced substantially in the ideal case scenario: the composite range uncertainty can be reduced below 1%. In that case, the composite range uncertainty can be reduced by a factor of two compared to the corresponding uncertainty of the kV stoichiometric method.

One potential way to reduce the inherent uncertainties in the presence of tissue composition variations for the stoichiometric method is to use an x-ray beam of higher energy such as the MV beam. As the x-ray energy increases, the Compton scatter interaction becomes more dominant, which reduces the nonlinearity between CT number and SPR thus the sensitivity to tissue composition variations. As shown in Table 30, the stoichiometric method using the MV beam can achieve similar or even slightly better accuracy compared to the kV-MV DECT, owing to both its lower sensitivity to tissue composition variations compared to the kV stoichiometric method and lower imaging uncertainties compared to the kV-MV DECT. However, the dominant uncertainty for the MV stoichiometric method is still its sensitivity to tissue composition variations. Because of that, in an ideal case, when CT imaging uncertainty

is completely removed, its total uncertainty becomes larger than that of the kV-MV DECT.

Overall, the kV-MV DECT is advantageous over the stoichiometric method in theory, and it may promise the reduction of the total uncertainty by a factor of two in the future, when CT imaging uncertainties are reduced further.

Table 30. Summary of comparison of the DECT method and the stoichiometric method.

The DECT Method					The Stoichiometric Calibration Method			
Methodology	SPR derived from two CT numbers based on both density and tissue composition information				SPR derived from a single CT number based on a pre-defined CT#-to-SPR calibration curve			
Strength	Resolve composition difference better, insensitive to tissue composition variation				Less sensitive to CT number variation			
Weakness	The DECT calculation is sensitive to CT number variation				Sensitive to tissue composition variation due to CT degeneracy problem			
		Prostate	Lung	HN		Prostate	Lung	HN
Margin (Current Technology)	kV-MV	1.9%	2.3%	1.9%	kV	3.0%	3.4%	3.1%
					MV	1.8%	1.9%	1.8%
Margin (Ideal Condition, no CT Imaging Uncertainty)	kV-MV	0.85%	0.82%	0.87%	kV	2.6%	3.0%	2.8%
					MV	1.4%	1.4%	1.5%

6.4.2 Measures to Improve the DECT Method's Accuracy

The dominant uncertainty factor for the kV-MV DECT is the CT imaging uncertainty (Table 29), which prevents us from reducing the total range uncertainty by a factor of two. Therefore, the key to reduce the total uncertainty is to reduce the imaging uncertainties. There are two important factors determining the imaging uncertainty, i.e., the sensitivity ratio factors (R_L and R_H) and the imaging uncertainties of the high-energy beam. The sensitivity ratio factors can be further reduced by lowering the energy

of the low-energy beam. The 80 kVp x-ray was the x-ray with the lowest energy that was available to us. Its effective energy was about 60 keV. If the effective energy can be reduced from 60 keV to 40 keV, the composite range uncertainty can be reduced from 1.9%, 2.3% and 1.9% to 1.5%, 1.8% and 1.6% for prostate, lung and head-and-neck patients. But as the x-ray energy becomes lower, CT number variations may increase. Further measurements need to be performed to find the optimum balance between the reduction of the sensitivity ratio factors and the increase of the CT imaging uncertainties. Moreover, the low energy mono-energetic x-rays may be an option for the kV beam in which case the beam hardening artifact is totally eliminated.

Another critical factor is the imaging uncertainties of the MV imaging. In this study, the CT imaging uncertainty estimates were based on the measurements using the TomoTherapy machine, which is not optimized for the reduction of CT imaging uncertainties. The imaging uncertainties may be further reduced by using dedicated MV scanners in future. If the CT imaging uncertainties can be reduced by a factor of two from current value, i.e., from 0.59% to 0.3%, the total range uncertainty ($2\text{-}\sigma$) for prostate, lung and head-and-neck patients can be reduced from 1.9%, 2.3% and 1.9% to 1.4%, 1.8% and 1.4%, respectively. This way, the composite range uncertainty can be reduced by a factor of 2 for prostate and head-and-neck patients, and a factor of 1.94 for lung patients.

6.4.3 Practical Limitations of Estimating Patient SPRs Using DECT

One general issue for DECT applications, especially quantitative applications like ours, is the misalignment of two CT image sets caused by patient movements between two CT scans. In general, patient motion artifact can be substantially reduced

by acquiring CT images for both energies simultaneously. There are two types of CT scanners with this capability – the scanner with fast kVp switching x-ray tubes and the scanner with two x-ray tubes mounted on the gantry orthogonally (Grasruck *et al.*, 2009; Flohr *et al.*, 2006). In our case, the most probable design for the kV-MV DECT scanner will be the dual source design. The negative effect of cross-scattered radiation in dual source CT systems can be mitigated by either model-based or measurement-based scatter correction techniques (Kyriakou and Kalender, 2007; Petersilka *et al.*, 2010). Besides, deformable image registration tools can also be helpful in reducing the misalignment.

Another common issue with DECT applications is the extra dose delivered to patients by one additional CT scan. A kV-kV DECT scan will deliver about twice the dose as a conventional kV-CT scan, and a kV-MV DECT scan will deliver an even higher dose. Our Monte Carlo simulations showed that the 1 MV beam needs to deliver about 5 times the dose as the 100 kVp beam, to achieve the same level of image noise. The detector modeled in our simulation was a 0.6 mm cesium iodide (CsI) scintillator detector. As shown before, the sensitivity ratio factor for the MV CT number is larger than that for the kV CT number, which indicates that it is more important to reduce the noise in the MV CT image. The image noise can be reduced by simply using a higher radiation dose. Although the imaging dose in treatment planning is negligible compared to the dose delivered by the radiation treatment itself, the ALARA (As Low As Reasonably Achievable) concept is valid and it is important to reduce the dose to the patient as much as possible. One way to accomplish this is to use thicker detectors. There have been several studies showing that the dose can be reduced substantially for

the MV CT if a thicker segmented scintillation detector is used (Sawant *et al.*, 2005; Monajemi *et al.*, 2006; Wang *et al.*, 2008; Wang *et al.*, 2009). Our Monte Carlo simulation results showed the ratio between the dose needed for a 1 MV beam and that for a 100 kVp beam to achieve the same noise level can be reduced from 6 to 2 by increasing the detector thickness from 0.6 mm to 10 mm. Another way is to reduce the noise by applying software solutions. The impact of random noise to the overall range uncertainty is reduced further considering the averaging effect along the beam path (Chvetsov and Paige, 2010).

6.4.4 Other Benefits of DECT

One additional benefit of the 1 MV beam is the reduction of metal artifacts in CT images of patients with high Z material, such as dental fillings. In a previous study, the use of a 320 kVp beam substantially reduced metal artifacts caused by a Ti insert (Yang *et al.*, 2008). Compared to the 320 kVp beam, the 1 MV beam has a higher peak energy thus should reduce the metal artifact even more and make it easier for physicians to draw contours in the artifact-affected area. In the artifact-affected area, the CT number of the kV beam may deviate substantially from its true value, which may cause errors in DECT calculation. Under that circumstance, the SPR can be estimated using just the MV CT number, which will minimize the imaging artifacts.

Another potential application of the EAN information derived from DECT is to help with tissue parameterization for Monte Carlo proton dose calculations. The element weighting proportion information is needed to determine the cross sections of different proton interactions for Monte Carlo dose calculations (Paganetti *et al.*, 2008). Currently, patient elemental proportion information is determined from CT numbers

based on the correlation between CT numbers and the percentages of each major element (Schneider *et al.*, 2000; Espana and Paganetti, 2010). The EAN should have a better correlation with elemental percentages compared to the CT number because CT number also depends on the density in addition to elemental compositions. We plotted the EAN versus the percentage for each major element for the ‘reference’ human body tissues listed in Table 2. The correlation between EANs and elemental proportions were found truly better than that between CT numbers and elemental proportions, especially for bone tissues (Fig. 31). Further study needs to be done to determine the overall benefit achievable by using the DECT, accounting for the relative large uncertainties carried in the EAN calculation.

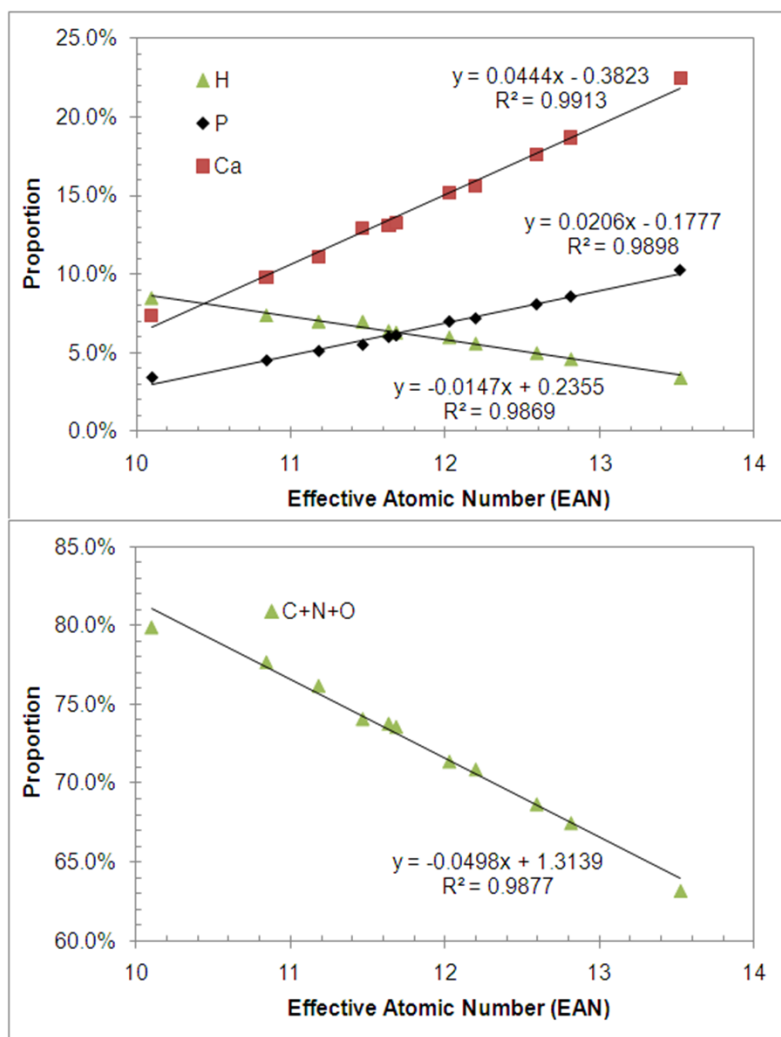


Figure 31. Elemental proportions of Hydrogen (H), Potassium (P), Calcium (Ca) and the summation of elemental proportion of Carbon (C), Nitrogen (N) and Oxygen (O), respectively, versus the effective atomic number (EAN) of human bone tissues listed in Table 2.

CHAPTER 7: CONCLUSIONS

7.1 Specific Aim I – Estimation of Range Uncertainty (SPR-related) in Current Practice

The uncertainties in estimated SPRs in current practice were thoroughly examined: 1) the uncertainties were broken down into five categories; 2) the uncertainties (1σ) were estimated for lung, soft and bone tissues separately; 3) the composite uncertainties (2σ) were estimated for prostate, lung and head-and-neck patients after accounting for different radiological path lengths going through different tissues in actual patient geometries.

The dominating uncertainty factor was found to be the inherent uncertainty in the presence of tissue composition variations. The uncertainties (1σ) in estimated SPRs of different tissue groups were shown substantially different (from 1.6% to 5.0%); however, the combined uncertainty (2σ) was fairly consistent at 3.0-3.4%. The current value used for distal and proximal margin design – 3.5% was found to be comparative, compared to our uncertainty estimates (3.0- 3.4%).

7.2 Specific Aim II – Development of the DECT Method

An empirical relationship was discovered between the mean excitation energies and effective atomic numbers (EANs) in human body tissues. This key discovery enabled us to develop an innovative method utilizing the dual-energy computed tomography (DECT) to derive proton stopping power ratio (SPR) distribution inside

patients (the DECT method). The DECT method was shown to hold theoretical advantages over the conventional stoichiometric method because of the extra tissue composition information. The DECT method can achieve higher accuracy in estimating SPRs than the stoichiometric method, especially in the presence of human tissue composition variations: the uncertainties using the DECT method increase from 0.24% for the ‘reference’ human tissues to 0.28% for the ‘individualized’ human tissues while they increase from 0.65% to 1.26% when using the stoichiometric method. Moreover, the maximal uncertainty could reach 6% for the stoichiometric method, much larger than 2% for the DECT method.

7.3 Specific Aim III – Developing Criteria for Selecting X-ray Pairs for DECT

The kV-MV DECT achieved substantially higher accuracy in SPR estimation than the kV-kV DECT, which was confirmed by our uncertainty propagation analysis. Our uncertainty propagation analysis also yielded the general principles for selecting x-ray pairs to minimize the sensitivity of the DECT calculation to CT number variations. The low-energy x-ray beam is the key; its effective energy needs to be made as low as practically possible. Meanwhile, the effective energy of the high-energy x-ray needs to be about 200 keV above that of the low-energy x-ray beam, in order to achieve the minimum sensitivity determined by the low-energy x-ray beam.

7.4 Specific Aim IV – Estimation of Margin Reduction using the DECT

The 80 kVp beam was found to be the optimum kV beam to pair up with the MV beam because of its relatively low sensitivity to CT number variations. The DECT with the kV-MV pair was shown to be capable of reducing total range uncertainty substantially, i.e., from current value, 3.5% to 2%, but failed to achieve the main goal of reducing the total uncertainty by a factor of two. It was largely limited by the imaging uncertainties existing in current CT technologies, especially in the MV imaging. However, it has been shown that the kV-MV DECT still has the promise to reduce the total uncertainty by a factor of two in future, if the CT imaging uncertainty can be reduced further with future advances in CT technologies such as better beam hardening correction.

7.5 Testing the Hypothesis

The first part of our hypothesis was tested to be true, i.e., the DECT can be designed to derive more accurate proton SPRs of human tissues than the stoichiometric method. The second part of the hypothesis was tested to be false, i.e., the margin to account for range uncertainties in SPRs for treatment planning can NOT be reduced by a factor of two as we hypothesized. Instead, the margin can be reduced from 3.5% to 1.9% for prostate and head-and-neck patients and 2.3% for lung patients. The imaging uncertainties in current CT technologies, especially the MV imaging, was found to be the major reason that prevented the kV-MV DECT from reaching the margin reduction by a factor of two.

APPENDIX A – ESTIMATION OF UNCERTAINTIES IN HUMAN TISSUE COMPOSITIONS PUBLISHED IN THE LITERATURE

A thorough literature review was performed in order to get a realistic estimate of the systematic and statistical uncertainties in the recommended tissue compositions of the ‘reference’ human tissues listed in Table 2. Our estimate of the systematic uncertainties in the recommended values was based on the difference between the recommended values of the same tissue type from different published articles. Our estimate of the statistical uncertainties was based on several studies by Woodard and White (Woodard, 1964; Woodard and White, 1982, 1986; White *et al.*, 1987; White *et al.*, 1991). In the remainder of this appendix, our estimates of the uncertainties in the recommended values of the key factors will be explained in details. The key factors include the density and the percentages of hydrogen (H) and calcium (Ca).

The recommended density values for most human tissues found in the literature were not determined by direct experimental measurements. Instead, they were determined by indirect calculation based on a tissue component model (Woodard and White, 1986; White *et al.*, 1987). The tissue component model assumes that all human body tissues are composed of several fundamental components such as water, lipids, proteins, minerals, etc., and the density of any human tissue can be simply calculated using the following equation:

$$\rho_x = \frac{1}{\sum_{i=1}^n \frac{w_i}{\rho_i}} , \quad (31)$$

where w_i and ρ_i are the weight by mass and the density of the i_{th} component, respectively. There is an inherent flaw in this method: it ignores possible structural changes after mixing these components *in vivo*. The difference between the density calculated with this method and its actual value can be up to 2% (Woodard and White, 1986). The reason why the densities calculated this way are still used in spite of their known possible errors is that the measured densities are not available for most human tissues (White *et al.*, 1991). Table 31 lists the recommended density values of several human tissue types from different articles. The relative differences were seen to range from 0.0% to 3.6% with the root-mean-square (RMS) average equal to 2.1%. Based on those facts, 2.1% was chosen as our estimate (1σ) of the systematic uncertainties in the recommended density values. Table 32 lists the mean density values and the standard deviations of seven human tissues estimated by Woodard and White (1986). The relative standard deviations were seen to range from 0.0% to 3.4% with the RMS average equal to 1.7%, which was used as our estimate (1σ) of the statistical uncertainties.

Table 31. Comparison of the recommended density values of the same human tissue type from different publications.

Tissue Types	Density (g/cm ³)		Rel. Diff.
	Woodard and White (1986)	ICRU 44 (1989)	
Adipose	0.95	0.916	3.6%
Mammary gland	1.02	1.05	2.9%
Liver	1.06	1.053	0.7%
Muscle	1.05	1.04	1.0%
Skin	1.09	1.1	0.9%
Eye Lens	1.07	1.1	2.8%

Lung (deflated)	1.05	1.05	0.0%
Ovary	1.05	1.048	0.2%
Red Marrow	1.03	1.03	0.0%
Thyroid	1.05	1.05	0.0%
Heart (blood filled)	1.06	1.03	2.8%
Cortical bone	1.92	1.85	3.6%
Root-mean-square (RMS)			2.1%

Table 32. Mean densities ($\langle\rho\rangle$) and standard deviations (σ) of human tissues from Woodard and White (1986). The relative standard deviation (σ_{rel}) was also calculated.

Tissue Types	$\langle\rho\rangle$, g/cm³	σ	σ_{rel}
Adipose	0.95	0.02	2.1%
Mammary Gland	1.02	0.035	3.4%
Liver	1.06	0.01	0.9%
Kidney	1.05	0.0	0.0%
Muscle	1.05	0.0	0.0%
Skin	1.09	0.0	0.0%
Heart	1.05	0.0	0.0%
Cortical Bone*	1.91	0.05	2.4%
Root-mean-square			1.7%

*: The mean and standard deviation of cortical bone is from Woodard (1964).

The hydrogen percentages of human body tissues published in the literature were also calculated instead of measured, based on the tissue component model. There are three major tissue components containing substantial amounts of hydrogen, which are water, lipids and proteins. Based on the component model, the hydrogen percentage of a human body tissue can be calculated using the following equation

$$H_x = \omega_W * H_W + \omega_L * H_L + \omega_P * H_P \quad , \quad (32)$$

where ω_W , ω_L and ω_P are the weight by mass of water, lipids and proteins in that body tissue, respectively. H_W , H_L and H_P are the hydrogen percentage by mass in water, lipids and proteins, respectively. The uncertainty in the calculated hydrogen percentage can be determined by taking the first derivative of Eq. 32,

$$\sigma_{H_x} = \sqrt{(\sigma_{\omega_W} * H_W)^2 + (\sigma_{\omega_L} * H_L)^2 + (\sigma_{\omega_P} * H_P)^2 + (\omega_W * \sigma_{H_W})^2 + (\omega_L * \sigma_{H_L})^2 + (\omega_P * \sigma_{H_P})^2} \quad , \quad (33)$$

where σ_{ω_W} , σ_{ω_L} and σ_{ω_P} are the uncertainty in the weight by mass of water, lipids and proteins, respectively, and σ_{H_W} , σ_{H_L} and σ_{H_P} are the uncertainty in the hydrogen percentage, respectively. Table 33 lists the uncertainties in hydrogen percentages of seven human body tissues estimated by Woodard and White (1986), which only accounted for the uncertainties in the weights of water, lipids, and proteins in human tissues. In order to determine the total uncertainty, we estimated the uncertainties in the hydrogen percentages of water, lipids, and proteins.

The uncertainty in hydrogen percentage of water (σ_{H_W}) is simply zero because the hydrogen percentage of water is constant. The uncertainty in hydrogen percentage of lipids (σ_{H_L}) was determined to be 1.0% by calculating the standard deviation of the hydrogen percentages of four major biological substances within the lipid category (Table 34). The uncertainty in hydrogen percentage of protein (σ_{H_P}) was determined to be 1.8% by calculating the standard deviation of the hydrogen percentages of twenty-three major amino acids, the building blocks of proteins. It is known that one water molecule is lost when two amino acids bind to each other. For a relatively long peptide, each amino acid loses one water molecule on average, which was considered when calculating the hydrogen percentages of amino acids shown in Table 35. After putting all those values back into Eq. 33, the total standard deviation of hydrogen percentage was calculated for each tissue type (Table 36). The RMS average standard deviation was calculated to be 0.5%, which was used as our estimate (1σ) of the statistical uncertainty in hydrogen percentage.

Table 33. Compositions of seven human tissues from Woodard and White (1986) and the calculated standard deviation of hydrogen percentages (σ'_H). Three tissue compositions are provided for each human tissue: mean and mean ± 1 standard deviation (σ). The hydrogen percentage was calculated based on the relative weight by mass and the hydrogen percentage of each tissue component.

Tissue Types	Category	Relative Weight by Mass			H	σ'_H
		Water	Lipid	Protein		
Adipose	Mean + σ	30.5%	61.4%	7.9%	11.2%	0.2%
	Mean	21.2%	74.1%	4.4%	11.4%	
	Mean – σ	11.4%	87.3%	1.0%	11.6%	
Heart	Mean + σ	71.0%	10.0%	18.2%	10.3%	0.0%
	Mean	75.9%	6.2%	17.1%	10.4%	
	Mean – σ	80.9%	2.4%	15.9%	10.4%	
Kidney	Mean + σ	72.3%	6.9%	19.9%	10.2%	0.1%
	Mean	76.6%	4.8%	17.7%	10.3%	
	Mean – σ	80.5%	2.8%	15.8%	10.4%	
Liver	Mean + σ	72.8%	7.8%	16.1%	10.1%	0.1%
	Mean	74.5%	4.6%	17.6%	10.0%	
	Mean – σ	75.6%	1.5%	19.6%	9.9%	
Mammary Gland	Mean + σ	30.2%	56.2%	13.3%	10.9%	0.3%
	Mean	51.4%	30.9%	17.4%	10.6%	
	Mean – σ	72.6%	5.6%	21.5%	10.2%	
Muscle	Mean + σ	70.0%	6.8%	21.3%	10.0%	0.1%
	Mean	74.1%	4.2%	19.8%	10.1%	
	Mean – σ	78.6%	1.6%	17.9%	10.2%	
Skin	Mean + σ	58.6%	13.5%	27.2%	10.0%	0.1%
	Mean	65.3%	9.4%	24.6%	10.0%	
	Mean – σ	72.1%	5.2%	22.0%	10.1%	

Table 34. Hydrogen percentages of major lipid substances from Woodard and White (1986).

Major Lipid Substances	H
Cerebroside	9.8%
Cholesterol	12.0%
Glycerol Trioleate	11.8%
Sphingomyelin	11.7%
Standard Deviation	1.0%

Table 35. Hydrogen percentages of amino acids.

Amino Acids	H
Isoleucine	9.8%
Leucine	9.8%
Lycine	9.4%

Methionine	6.9%
Phenylalanine	6.2%
Threonine	7.0%
Tryptophan	5.4%
Valine	9.2%
Alanine	7.1%
Asparagine	5.3%
Aspartic Acid	4.4%
Cysteine	4.9%
Glutamic acid	5.5%
Glutamine	6.3%
Glycine	5.3%
Proline	7.3%
Selenocysteine	3.4%
Serine	5.8%
Tyrosine	5.6%
Arginine	7.7%
Histidine	5.1%
Ornithine	8.8%
Taurine	4.7%
Min	3.4%
Max	9.8%
Mean	6.6%
Standard Deviation	1.8%

Table 36. Our estimates of the uncertainties corresponding to the first three items in Eq. 33 given by Woodard and White (1986) (σ'_H), our estimates of the uncertainties corresponding to the last three items in Eq. 33 ($\omega_W * \sigma_{HW}$ for water, $\omega_L * \sigma_{HL}$ for lipid, and $\omega_P * \sigma_{HP}$ for protein), and the total uncertainty (σ_H) calculated using Eq. 33 for seven human tissue types.

Tissues	σ'_H	$\omega_W * \sigma_{HW}$	$\omega_L * \sigma_{HL}$	$\omega_P * \sigma_{HP}$	σ_H
Adipose	0.2%	0.0%	0.7%	0.1%	0.8%
Heart	0.0%	0.0%	0.1%	0.3%	0.3%
Kidney	0.1%	0.0%	0.0%	0.3%	0.3%
Liver	0.1%	0.0%	0.0%	0.3%	0.3%
Mammary Gland	0.3%	0.0%	0.3%	0.3%	0.6%
Muscle	0.1%	0.0%	0.0%	0.4%	0.4%
Skin	0.1%	0.0%	0.1%	0.4%	0.5%
Root-mean-square (RMS)					0.5%

The uncertainties in calcium percentage of bone tissues depend strongly on the uncertainty in calcium percentage of cortical bone. This is because the elemental compositions of bone tissues were calculated based on the weights by mass and the

elemental compositions of fundamental bone tissue components – cortical bone (compact bone), trabecular bone (cancellous bone or spongiosa), bone marrow and cartilage (Woodard and White, 1982). Among them, only cortical bone and trabecular bone contain substantial amount of calcium. Cortical bone contains more calcium than trabecular bone, i.e., 22.2% by mass for cortical bone compared to 7.47% for trabecular bone. Cortical bone is also much denser than trabecular bone, i.e., 1.90 g/cm^3 for cortical bone compared to 1.18 g/cm^3 for trabecular bone. In a typical adult, about 80% of total bone mass is cortical bone and the rest is trabecular bone (Valentin and Streffer, 2002). Moreover, the calcium percentage of trabecular bone was calculated based on the assumption that trabecular bone is a combination of cortical bone and bone marrow. Thus, we decided to only study the uncertainty in the calcium percentage of cortical bone and apply it for all bone tissues.

Table 37 shows the mean value and the range of calcium percentage of cortical bone in adults and children. The relative standard deviation was calculated to be 0.5% and 0.8% for adults and children, respectively. It is understandable that the calcium percentage in children has a larger spread because bones in children are still growing. We chose 1% as our estimate of statistical uncertainties in calcium percentage to cover both adult and pediatric patients. The systematic uncertainties in calcium percentage were determined using the difference between the recommended calcium percentages for adults from two publications (Table 37), which was calculated to be 1% as well.

Table 37. Calcium percentages in human cortical bone.

Groups	Ca %				Sources
	Mean	STD	Min	Max	
Age 2-19	20.8%	0.83%	19.0%	22.8%	Woodard (1964)

Age 20-74	22.5%	0.50%	21.0%	23.8%	
Adult	21.5%				Valentin and Streffer (2002)

One limitation of our estimation is that all our data were taken from studies based on healthy adults. It is known that tissue compositions depend on the state of health, nutrition, sex, age, etc (White *et al.*, 1991). Most cancer patients receiving radiation therapy are relatively old in age and in bad health condition. Therefore, further studies are needed to determine tissue compositions of cancer patients and compare them with healthy adults.

Additionally, our data from the literature did not consider spatial variation of tissue compositions within a tissue. Kalef-Ezra *et al.* (1998; 1999) found substantial variations of electron densities of lung tissues within the thoracic region. The variations were found to be approximately 10% for the same gender.

It is possible that our estimate of the uncertainties in the recommended human tissue compositions is smaller than reality because we did not consider the two factors mentioned in previous paragraphs.

APPENDIX B – METAL ARTIFACT REDUCTION USING HIGH ENERGY COMPUTED TOMOGRAPHY

This appendix is a summary of our preliminary work before developing the kV-MV DECT, which was evaluating metal artifact reduction and the improvement in EDR measurement using orthovoltage CT (OVCT) imaging and kilovoltage CT (KVCT).

A bench-top CT imaging system was constructed using the x-ray tube with adjustable peak voltage up to 320 kVp (Fig. 32). The RMI 467 phantom loaded with various human tissue equivalent samples were scanned using the 125 kVp (KVCT) and 320 kVp (OVCT) x-ray beams. The CT#-to-EDR calibration curves were determined for both beams using the stoichiometric method. The metal artifact and its impact on EDR measurement of the metal itself and the surrounding areas were studied by comparing CT images with and without metal inserts such as a titanium rod and an aluminum rod (Fig. 33).

The relationships between the CT numbers (HUs) and EDRs were seen to be more predictable for OVCT than KVCT (Fig. 34). Moreover, unlike KVCT, the calibration curve for OVCT was insensitive to the subset of tissue substitutes chosen for the calibration, so it is robust to generate the calibration curve just based on tissue substitutes for OVCT (Fig. 35). Metal artifacts were found to be substantially reduced by using the OVCT compared to the kVCT (Fig. 36). Uncertainties in EDR measurements due to severe metal artifact were reduced substantially from 42% (Max) and 18% (RMS) in KVCT to 12% and 2% in OVCT, respectively. Improvements were

also seen in areas with less metal artifact. Overall, the OVCT were found to be a good option to achieve high precision treatment planning for patients with metal implants.

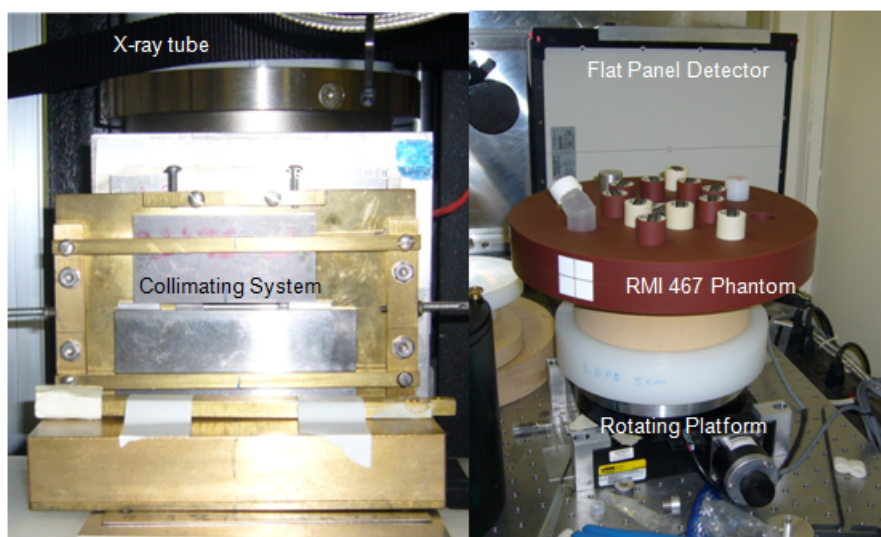


Figure 32. Experimental setup of the bench-top CT imaging system.

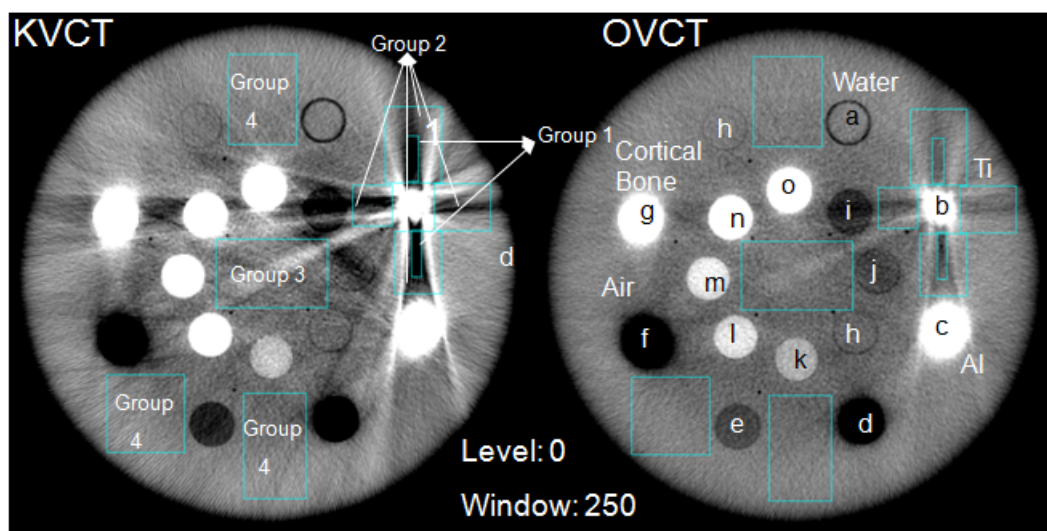


Figure 33. Axial CT images of the RMI 467 phantom scanned using KVCT (left) versus OVCT (right) beam, respectively. The arrangement of the inserts is identical in both images, for which the keys are provided in Table 38. The object distortion and streak artifacts are significantly

reduced by using OVCT. Note that the same window and level was used for both images. Ten rectangular ROIs were chosen, which were grouped to four groups based on the level of the artifact in KVCT image, to evaluate the CT number deviations of solid water affected by the metal streaking artifact.

Table 38. This table lists the materials of inserts used in the RMI 467 phantom and their positions in the phantom. The positions here correspond to the labels used in Fig. 33. Also listed are the nominal electron densities relative to water (EDRs), the mean CT number, and the standard error of the mean (SEM) CT number within the material insert.

Materials	Position in Phantom	Nominal Electron Density Relative to Water	KVCT		OVCT	
			Mean CT number	SEM	Mean CT number	SEM
Air	f	0.00	-1000.0	1.28	-1000.0	1.14
Lung (LN-450)	d	0.40	-542.7	1.37	-549.4	1.15
Adipose (AP6)	i	0.90	-96.3	1.20	-96.5	1.24
Breast	j	0.96	-79.8	1.44	-62.2	0.97
CT Solid Water	h	0.99	-9.4	0.75	-6.6	0.78
True Water	a	1.00	0.0	0.90	0.0	0.86
Liver (LV1)	k	1.07	71.4	1.10	50.8	0.91
Inner Bone	l	1.09	218.5	1.30	106.0	1.00
Bone (B200)	m	1.11	221.1	1.15	114.2	0.97
Bone (CB2-30%)	o	1.28	449.5	1.03	269.0	1.03
Bone (CB2-50%)	p	1.47	822.1	1.56	488.9	1.04
Cortical Bone (SB3)	g	1.69	1236.8	1.41	777.3	1.04
Aluminum	c	2.34	1895.6	2.00	1380.4	1.47
Titanium	b	3.79	4800.7	11.27	2929.1	6.80

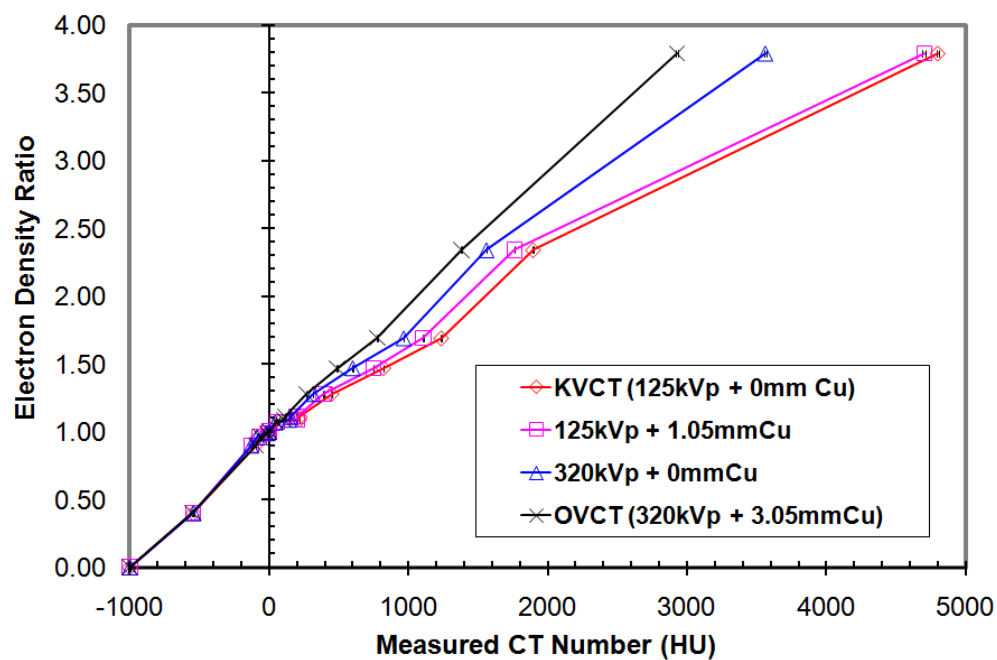


Figure 34. Relationship between the relative electron density and the measured CT number (HU) of the materials for x-ray beams with different energy spectra. '125 kVp + 1.05mm Cu' represents the beam of 125 kVp with 1.05mm extra Au filter, and '320 kVp + 0mmCu' represents the beam of 320 kVp with no Au filter. The relationship between relative electron density and the measured CT number are shown to follow a more predictable linear relationship for OVCT than for KVCT.

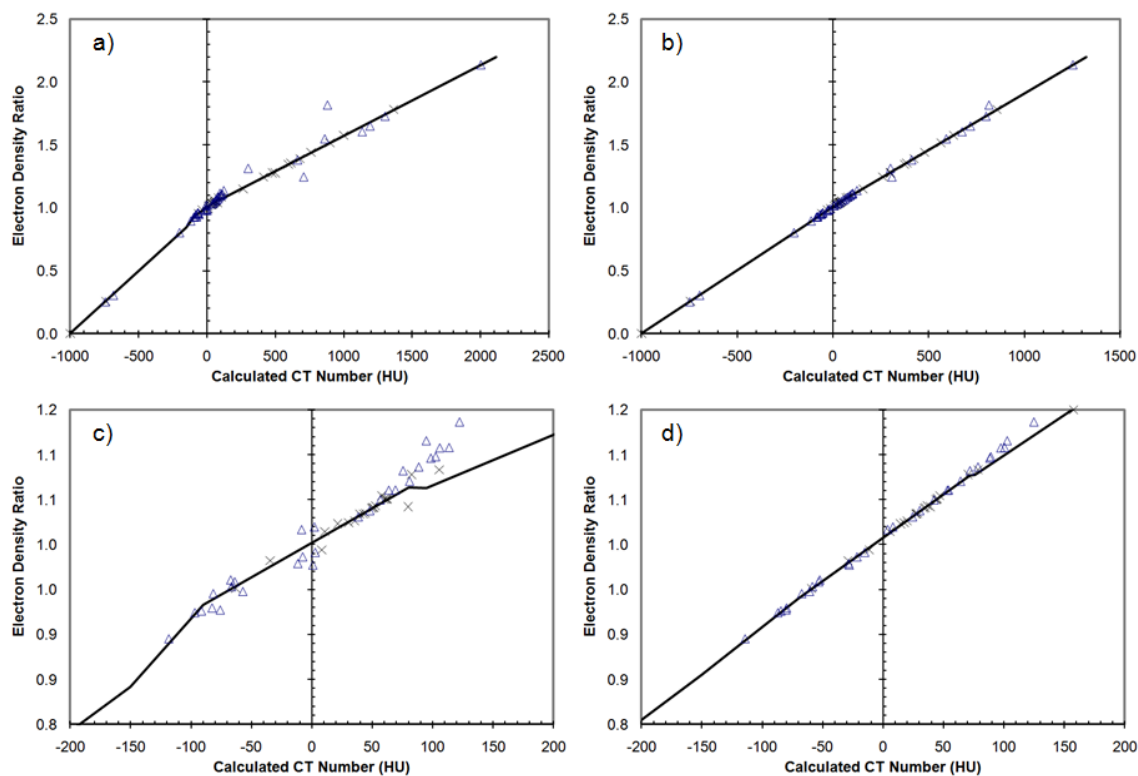


Figure 35. Stoichiometric CT Number calibration curves for KVCT (a,c) and OVCT (b,d). (c) and (d) are the zoomed-in versions of (a) and (b), respectively. The crosses represent real tissue and the triangles represent tissue substitutes. The solid line represent the calibration curve, which is obtained by three linear regression fit to real tissue points. Real tissue points are shown to fit better with the calibration curve for OVCT than for KVCT.

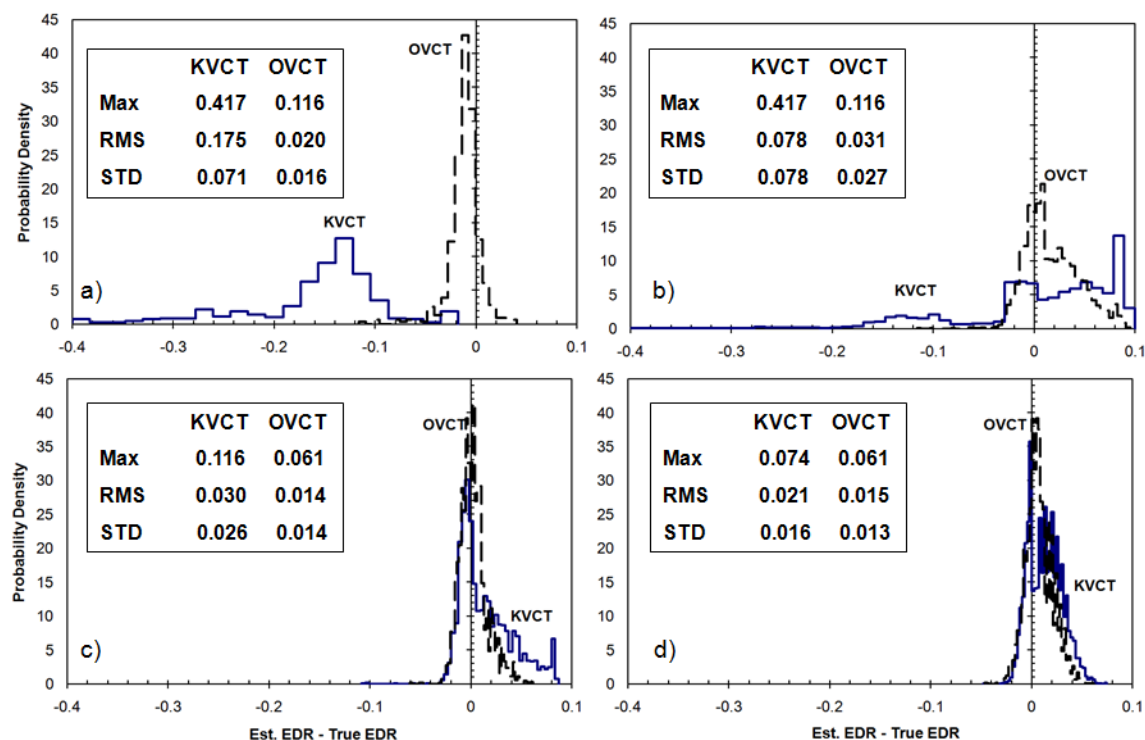


Figure 36. Comparison of KVCT and OVCT showing the deviation of estimated relative electron densities from true relative electron densities for solid water ROIs belonging to four different groups. ROIs are grouped based on the metal artifact level in KVCT image in Fig. 33(a) – (d) are histograms of the deviation distribution for Group 1 with most severe artifact, Group 2 with heavy artifact, for Group 3 with medium artifact, for Group 4 with least artifact, respectively. The maximal absolute deviation, the root-mean-square (RMS) deviation and the standard deviation (STD) are provided for each deviation distribution.

REFERENCES

- 2003 Computed tomography (CT) accreditation program phantom testing criteria
- 2007 LightSpeedTM RT¹⁶, Xtra Technical Reference Manual.
- Alvarez R and Seppi E 1979 A comparison of noise and dose in conventional and energy selective computed tomography *IEEE Trans. Nucl. Sci.* **26** 2853-2856
- Alvarez R E and Macovski A 1976 Energy-selective reconstructions in X-ray computerised tomography *Physics in Medicine and Biology* **21** 733-44
- Anferov V 2010 Analytic estimates of secondary neutron dose in proton therapy *Physics in Medicine and Biology* **55** 7509-22
- Barrett J F and Keat N 2004 Artifacts in CT: Recognition and avoidance *Radiographics* **24**
- Bazalova M, Carrier J F, Beaulieu L and Verhaegen F 2008 Dual-energy CT-based material extraction for tissue segmentation in Monte Carlo dose calculations *Physics in Medicine and Biology* **53** 2439-56
- Berger M J, Hubbell J H, Seltzer S M, Chang J, Coursey J S, Sukumar R. and Zucker D S 2005 XCOM: Photon Cross Section Database (version 1.3).
- Bischel H and Hiraoka T 1992 Energy loss of 70 MeV protons in elements *Nuclear Inst. and Methods in Physics Research, B* **66** 345-51
- Brooks R A 1977 A quantitative theory of the Hounsfield unit and its application to dual energy scanning *Journal of Computer Assisted Tomography* **1** 487-93
- Cann C E 1987 Quantitative CT applications: Comparison of current scanners *Radiology* **162** 257-61
- Cann C E, Gamsu G, Birnberg F A and Webb W R 1982 Quantification of calcium in solitary pulmonary nodules using single- and dual-energy CT *Radiology* **145** 493-6

- Chen G T Y, Singh R P and Castro J R 1979 Treatment planning for heavy ion radiotherapy *International Journal of Radiation Oncology Biology Physics* **5** 1809-19
- Chvetsov A V and Paige S L 2010 The influence of CT image noise on proton range calculation in radiotherapy planning *Physics in Medicine and Biology* **55** N141-N9
- Civinini C, Brianzi M, Bruzzi M, Bucciolini M, Candiano G, Capineri L, Cirrone G A P, Cuttone G, Lo Presti D, Marrazzo L, Mazzaglia E, Menichelli D, Pieri S, Randazzo N, Sipala V, Stancampiano C, Talamonti C, Tesi M and Valentini S 2010 Towards a proton imaging system *Nuclear Instruments and Methods in Physics Research, Section A: Accelerators, Spectrometers, Detectors and Associated Equipment* **623** 588-90
- Clayton J, Virshup G, Yang M, Mohan R and Dong L 2009 Improvements in medical CT image reconstruction accuracy in the presence of metal objects by using X-rays up to 1 MeV. In: *Proceedings of SPIE - The International Society for Optical Engineering*, (San Diego, CA
- Coleman A J and Sinclair M 1985 A beam-hardening correction using dual-energy computed tomography *Physics in Medicine and Biology* **30** 1251-6
- Constantinou C, Harrington J C and DeWerd L A 1992 An electron density calibration phantom for CT-based treatment planning computers *Medical Physics* **19** 325-7
- Cormack A M 1963 Representation of a function by its line integrals, with some radiological applications *Journal of Applied Physics* **34** 2722-7
- Cormack A M 1964 Representation of a function by its line integrals, with some radiological applications. II *Journal of Applied Physics* **35** 2908-13
- Cormack A M and Koehler A M 1976 Quantitative proton tomography: Preliminary experiments *Physics in Medicine and Biology* **21** 560-9
- De Cecco C N, Buffa V, Fedeli S, Luzietti M, Vallone A, Ruopoli R, Miele V, Rengo M, Paolantonio P, Maurizi Enrici M, Laghi A and David V 2010 Dual energy CT (DECT) of the liver: Conventional versus virtual unenhanced images *European Radiology* **20** 2870-5

- DeMarco J J, Solberg T D and Smathers J B 1998 A CT-based Monte Carlo simulation tool for dosimetry planning and analysis *Medical Physics* **25** 1-11
- Di Chiro G, Brooks R A and Kessler R M 1979 Tissue signatures with dual-energy computed tomography *Radiology* **131** 521-3
- Du Plessis F C P, Willemse C A, Lotter M G and Goedhals L 1998 The indirect use of CT numbers to establish material properties needed for Monte Carlo calculation of dose distributions in patients *Medical Physics* **25** 1195-201
- Emfietzoglou D, Garcia-Molina R, Kyriakou I, Abril I and Nikjoo H 2009 A dielectric response study of the electronic stopping power of liquid water for energetic protons and a new I-value for water *Physics in Medicine and Biology* **54** 3451-72
- Espana S and Paganetti H 2010 The impact of uncertainties in the CT conversion algorithm when predicting proton beam ranges in patients from dose and PET-activity distributions *Physics in Medicine and Biology* **55** 7557-71
- Finger P T and Chin K J 2011 Fluorodeoxyglucose positron emission tomography/computed tomography (pet/ct) physiologic imaging of choroidal melanoma: Before and after ophthalmic plaque radiation therapy *International Journal of Radiation Oncology Biology Physics* **79** 137-42
- Flampouri S, Slopesma R, Yeung D, Malyapa R, Keole S, Vargas C and Li Z 2007 Realistic estimation of proton range uncertainties and dosimetric implications *Med. Phys.* **34** 2643
- Flohr T G, McCollough C H, Bruder H, Petersilka M, Gruber K, Sub C, Grasruck M, Stierstorfer K, Krauss B, Raupach R, Primak A N, Kuttner A, Achenbach S, Becker C, Kopp A and Ohnesorge B M 2006 First performance evaluation of a dual-source CT (DSCT) system *European Radiology* **16** 256-68
- Fraser R G, Barnes G T and Hickey N 1986 Potential value of digital radiography. Preliminary observations on the use of dual-energy subtraction in the evaluation of pulmonary nodules *Chest* **89**

- Genant H K and Boyd D 1977 Quantitative bone mineral analysis using dual energy computed tomography *Investigative Radiology* **12** 545-51
- Gottschalk B 2006 Neutron dose in scattered and scanned proton beams: In regard to Eric J. Hall (Int J Radiat Oncol Biol Phys 2006;65:1-7) *International Journal of Radiation Oncology Biology Physics* **66** 1594
- Granton P V, Pollmann S I, Ford N L, Drangova M and Holdsworth D W 2008 Implementation of dual- and triple-energy cone-beam micro-CT for postreconstruction material decomposition *Medical Physics* **35** 5030-42
- Grasruck M, Kappler S, Reinwand M and Stierstorfer K 2009 Dual energy with dual source CT and kVp switching with single source CT: A comparison of dual energy performance. In: *Progress in Biomedical Optics and Imaging - Proceedings of SPIE*, (Lake Buena Vista, FL
- Hall E J 2006 Intensity-modulated radiation therapy, protons, and the risk of second cancers *International Journal of Radiation Oncology Biology Physics* **65** 1-7
- Hanson K M, Bradbury J N, Cannon T M, Hutson R L, Laubacher D B, MacEk R J, Paciotti M A and Taylor C A 1981 Computed tomography using proton energy loss *Physics in Medicine and Biology* **26** 965-83
- Hsieh J 2003 Image artifacts: Appearances, causes and corrections *Computed Tomography: Principles, Design, Artifacts and Recent Advances* 167-240
- ICRU 1989 Tissue substitutes in radiation dosimetry and measurement *ICRU Report 44*
- ICRU 1993 Stopping Power and Ranges for Protons and Alpha Particles *ICRU Report 49*
- ICRU 2005 Stopping Ions Heavier Than Helium *ICRU Report 73*
- Jäkel O and Reiss P 2007 The influence of metal artefacts on the range of ion beams *Physics in Medicine and Biology* **52** 635-44
- Jeraj R, Mackie T R, Balog J, Olivera G, Pearson D, Kapatoes J, Ruchala K and Reckwerdt P 2004 Radiation characteristics of helical tomotherapy *Medical Physics* **31** 396-404

- Jiang H, Seco J and Paganetti H 2007 Effects of Hounsfield number conversion on CT based proton Monte Carlo dose calculations *Medical Physics* **34** 1439-49
- Johnson T R C, Kraub B, Sedlmair M, Grasruck M, Bruder H, Morhard D, Fink C, Weckbach S, Lenhard M, Schmidt B, Flohr T, Reiser M F and Becker C R 2007 Material differentiation by dual energy CT: Initial experience *European Radiology* **17** 1510-7
- Kalef-Ezra J, Karantanas A and Tsekeris P 1999 CT measurement of lung density *Acta Radiologica* **40** 333-7
- Kalef-Ezra J A, Karantanas A H, Koligliatis T, Boziari A and Tsekeris P 1998 Electron density of tissues and breast cancer radiotherapy: A quantitative ct study *International Journal of Radiation Oncology Biology Physics* **41** 1209-14
- Kalender W A 2006 X-ray computed tomography *Physics in Medicine and Biology* **51**
- Kanematsu N, Matsufuji N, Kohno R, Minohara S and Kanai T 2003 A CT calibration method based on the polybinary tissue model for radiotherapy treatment planning *Physics in Medicine and Biology* **48** 1053-64
- Kawrakow I, Mainegra-Hing E, Tessier F and Walters B R B 2009 The EGSnrc C++ class library.
- Keall P J, Joshi S, Sastry Vedam S, Siebers J V, Kini V R and Mohan R 2005 Four-dimensional radiotherapy planning for DMLC-based respiratory motion tracking *Medical Physics* **32** 942-51
- Kelcz F, Joseph P M and Hilal S K 1979 Noise considerations in dual energy CT scanning *Medical Physics* **6** 418-25
- Knopf A, Parodi K, Paganetti H, Cascio E, Bonab A and Bortfeld T 2008 Quantitative assessment of the physical potential of proton beam range verification with PET/CT *Physics in Medicine and Biology* **53** 4137-51
- Knopf A C, Parodi K, Paganetti H, Bortfeld T, Daartz J, Engelsman M, Liebsch N and Shih H 2011 Accuracy of proton beam range verification using post-treatment positron emission

tomography/computed tomography as function of treatment site *International Journal of Radiation Oncology Biology Physics* **79** 297-304

Kumazaki Y, Akagi T, Yanou T, Suga D, Hishikawa Y and Teshima T 2007 Determination of the mean excitation energy of water from proton beam ranges *Radiation Measurements* **42** 1683-91

Kyriakou Y and Kalender W A 2007 Intensity distribution and impact of scatter for dual-source CT *Physics in Medicine and Biology* **52** 6969-89

Lawrence J H, Tobias C A, Born J L, McCombs R K, Roberts J E, Anger H O, Low-Beer B V and Huggins C B 1958 Pituitary irradiation with high-energy proton beams: a preliminary report *Cancer research* **18** 121-34

Li T, Liang Z, Singanallur J V, Satogata T J, Williams D C and Schulte R W 2006 Reconstruction for proton computed tomography by tracing proton trajectories: A Monte Carlo study *Medical Physics* **33** 699-706

Liu X, Yu L, Primak A N and McCollough C H 2009 Quantitative imaging of element composition and mass fraction using dual-energy CT: Three-material decomposition *Medical Physics* **36** 1602-9

Lomax A J 2008a Intensity modulated proton therapy and its sensitivity to treatment uncertainties 1: The potential effects of calculational uncertainties *Physics in Medicine and Biology* **53** 1027-42

Lomax A J 2008b Intensity modulated proton therapy and its sensitivity to treatment uncertainties 2: The potential effects of inter-fraction and inter-field motions *Physics in Medicine and Biology* **53** 1043-56

Lomax A J 2009 Charged particle therapy: The physics of interaction *Cancer Journal* **15** 285-91

- Maaß C, Baer M and Kachelrieß M 2009 Image-based dual energy CT using optimized precorrection functions: A practical new approach of material decomposition in image domain *Medical Physics* **36** 3818-29
- Menichelli D, Bruzzi M, Bucciolini M, Candiano G, Pablo Cirrone G A, Capineri L, Civinini C, Cuttone G, Presti D L, Marrazzo L, Pallotta S, Randazzo N, Sipala V, Talamonti C, Valentini S, Pieri S, Reggioli V, Brianzi M and Tesi M 2010 Characterization of a silicon strip detector and a YAG:Ce calorimeter for a proton computed radiography apparatus *IEEE Transactions on Nuclear Science* **57** 8-16
- Millner M R, McDavid W D and Waggener R G 1979 Extraction of information from CT scans at different energies *Medical Physics* **6** 70-1
- Monajemi T T, Fallone B G and Rathee S 2006 Thick, segmented CdWO₄-photodiode detector for cone beam megavoltage CT: A Monte Carlo study of system design parameters *Medical Physics* **33** 4567-77
- Moyers M F, Miller D W, Bush D A and Slater J D 2001 Methodologies and tools for proton beam design for lung tumors *International Journal of Radiation Oncology Biology Physics* **49** 1429-38
- Moyers M F, Sardesai M, Sun S and Miller D W 2009 Ion Stopping Powers and CT Numbers *Medical Dosimetry* **35** 179-94
- Nakamura K 2010 Review of Particle Physics *Journal of Physics G: Nuclear and Particle Physics* **37** 075021
- Noh J, Fessler J A and Kinahan P E 2009 Statistical sinogram restoration in dual-energy CT for PET attenuation correction *IEEE Transactions on Medical Imaging* **28** 1688-702
- Paganetti H, Jiang H, Parodi K, Slopsema R and Engelsman M 2008 Clinical implementation of full Monte Carlo dose calculation in proton beam therapy *Physics in Medicine and Biology* **53** 4825-53

- Parodi K, Paganetti H, Shih H A, Michaud S, Loeffler J S, DeLaney T F, Liebsch N J, Munzenrider J E, Fischman A J, Knopf A and Bortfeld T 2007 Patient Study of In Vivo Verification of Beam Delivery and Range, Using Positron Emission Tomography and Computed Tomography Imaging After Proton Therapy *International Journal of Radiation Oncology Biology Physics* **68** 920-34
- Paul H, Geithner O and Jakel O 2007 The Influence of Stopping Powers upon Dosimetry for Radiation Therapy with Energetic Ions *Advances in Quantum Chemistry* **52** 289-306
- Perez-Andjar A, Newhauser W D and Deluca P M 2009 Neutron production from beam-modifying devices in a modern double scattering proton therapy beam delivery system *Physics in Medicine and Biology* **54** 993-1008
- Petersilka M, Stierstorfer K, Bruder H and Flohr T 2010 Strategies for scatter correction in dual source CT *Medical Physics* **37** 5971-92
- Polf J C and Newhauser W D 2005 Calculations of neutron dose equivalent exposures from range-modulated proton therapy beams *Physics in Medicine and Biology* **50** 3859-73
- Primak A N, Ramirez Giraldo J C, Liu X, Yu L and McCollough C H 2009 Improved dual-energy material discrimination for dual-source CT by means of additional spectral filtration *Medical Physics* **36** 1359-69
- Rietzel E, Chen G T Y, Choi N C and Willet C G 2005 Four-dimensional image-based treatment planning: Target volume segmentation and dose calculation in the presence of respiratory motion *International Journal of Radiation Oncology Biology Physics* **61** 1535-50
- Rogers D W O, Walters B and Kawrakow I 2005 BEAMnrc users manual.
- Rutherford E 1919 Collisions of α -particles with light atoms. III. Nitrogen and oxygen atoms *Philosophical Magazine* **37** 571-80
- Rutherford R A, Pullan B R and Isherwood I 1976 X ray energies for effective atomic number determination *Neuroradiology* **11** 23-8

- Sawant A, Antonuk L E, El-Mohri Y, Zhao Q, Li Y, Su Z, Wang Y, Yamamoto J, Du H, Cunningham I, Klugerman M and Shah K 2005 Segmented crystalline scintillators: An initial investigation of high quantum efficiency detectors for megavoltage x-ray imaging *Medical Physics* **32** 3067-83
- Schaffner B and Pedroni E 1998 The precision of proton range calculations in proton radiotherapy treatment planning: Experimental verification of the relation between CT-HU and proton stopping power *Physics in Medicine and Biology* **43** 1579-92
- Schneider U, Pedroni E and Lomax A 1996 The calibration of CT Hounsfield units for radiotherapy treatment planning *Physics in Medicine and Biology* **41** 111-24
- Schneider W, Bortfeld T and Schlegel W 2000 Correlation between CT numbers and tissue parameters needed for Monte Carlo simulations of clinical dose distributions *Physics in Medicine and Biology* **45** 459-78
- Seltzer S M and Berger M J 1982 Evaluation of the collision stopping power of elements and compounds for electrons and positrons *International Journal of Applied Radiation and Isotopes* **33** 1189-218
- Sipala V, Bruzzi M, Bucciolini M, Candiano G, Capineri L, P. Cirrone G A, Civinini C, Cuttone G, Lo Presti D, Marrazzo L, Mazzaglia E, Menichelli D, Randazzo N, Talamonti C and Valentini S 2010 A proton imaging device: Design and status of realization *Nuclear Instruments and Methods in Physics Research, Section A: Accelerators, Spectrometers, Detectors and Associated Equipment* **612** 566-70
- Slater J M, Archambeau J O, Miller D W, Notarus M I, Preston W and Slater J D 1992 The proton treatment center at Loma Linda University Medical Center: Rationale for and description of its development *International Journal of Radiation Oncology Biology Physics* **22** 383-9
- Smith A R 2009 Vision 2020: Proton therapy *Medical Physics* **36** 556-68
- Svendsen O L, Hassager C, Bergmann I and Christiansen C 1993 Measurement of abdominal and intra-abdominal fat in postmenopausal women by dual energy X-ray absorptiometry and

anthropometry: Comparison with computerized tomography *International Journal of Obesity* **17** 45-51

Talamonti C, Reggioli V, Bruzzi M, Bucciolini M, Civinini C, Marrazzo L, Menichelli D, Pallotta S, Randazzo N, Sipala V, Cirrone G A P, Petterson M, Blumenkrantz N, Feldt J, Heimann J, Lucia D, Seiden A, Williams D C, Sadrozinski H F W, Bashkirov V and Schulte R 2010 Proton radiography for clinical applications *Nuclear Instruments and Methods in Physics Research, Section A: Accelerators, Spectrometers, Detectors and Associated Equipment* **612** 571-5

Torikoshi M, Tsunoo T, Sasaki M, Endo M, Noda Y, Ohno Y, Kohno T, Hyodo K, Uesugi K and Yagi N 2003 Electron density measurement with dual-energy x-ray CT using synchrotron radiation *Physics in Medicine and Biology* **48** 673-85

Tran D N, Straka M, Roos J E, Napel S and Fleischmann D 2009 Dual-energy CT Discrimination of Iodine and Calcium. Experimental Results and Implications for Lower Extremity CT Angiography *Academic Radiology* **16** 160-71

Trofimov A, Wang Y, Merrick S, Wong J and Efstathiou J 2010 WE-A-BRA-03: Considerations of Inter-Observer and Inter-Fractional Anatomical Variability in Estimating the Beam Range Uncertainty in Proton Therapy of Prostate Cancer *Medical Physics* **37** 3409-10

Underberg R W M, Lagerwaard F J, Cuijpers J P, Slotman B J, Van Sornsen De Koste J R and Senan S 2004 Four-dimensional CT scans for treatment planning in stereotactic radiotherapy for stage I lung cancer *International Journal of Radiation Oncology Biology Physics* **60** 1283-90

Unkelbach J, Bortfeld T, Martin B C and Soukup M 2009 Reducing the sensitivity of IMPT treatment plans to setup errors and range uncertainties via probabilistic treatment planning *Medical Physics* **36** 149-63

Urie M, Goitein M and Wagner M 1984 Compensating for heterogeneities in proton radiation therapy *Physics in Medicine and Biology* **29** 553-66

- Valentin J and Streffer C 2002 Basic anatomical and physiological data for use in radiological protection: Reference values - ICRP Publication 89 *Annals of the ICRP* **32** 1-265
- Wang Y, Antonuk L E, El-Mohri Y, Zhao Q, Sawant A and Du H 2008 Monte Carlo investigations of megavoltage cone-beam CT using thick, segmented scintillating detectors for soft tissue visualization *Medical Physics* **35** 145-58
- Wang Y, Antonuk L E, Zhao Q, El-Mohri Y and Perna L 2009 High-DQE EPIDs based on thick, segmented BGO and CsI:Tl scintillators: Performance evaluation at extremely low dose *Medical Physics* **36** 5707-18
- White D R, Widdowson E M, Woodard H Q and Dickerson J W T 1991 The composition of body tissues. (II) Fetus to young adult *British Journal of Radiology* **64** 149-59
- White D R, Woodard H Q and Hammond S M 1987 Average soft-tissue and bone models for use in radiation dosimetry *British Journal of Radiology* **60** 907-13
- Williamson J F, Li S, Devic S, Whiting B R and Lerma F A 2006 On two-parameter models of photon cross sections: Application to dual-energy CT imaging *Medical Physics* **33** 4115-29
- Williamson J F, Whiting B R, Benac J, Murphy R J, Blaine G J, O'Sullivan J A, Politte D G and Snyder D L 2002 Prospects for quantitative computed tomography imaging in the presence of foreign metal bodies using statistical image reconstruction *Medical Physics* **29** 2404-18
- Wilson R R 1946 Radiological use of fast protons *Radiology* **47** 487-91
- Woodard H Q 1964 The composition of human cortical bone: effect of age and of some abnormalities *Clinical Orthopaedics and Related Research* **37** 187-93
- Woodard H Q and White D R 1982 Bone models for use in radiotherapy dosimetry *British Journal of Radiology* **55** 277-82
- Woodard H Q and White D R 1986 The composition of body tissues *British Journal of Radiology* **59** 1209-18

Yang M, Virshup G, Clayton J, Zhu R X, Mohan R and Dong L 2010 Theoretical variance analysis of single- and double-energy computed tomography methods for measuring proton stopping power ratios of biological tissues *Physics in Medicine and Biology* **55** 1343-62

Yang M, Virshup G, Mohan R, Shaw C C, Zhu X R and Dong L 2008 Improving accuracy of electron density measurement in the presence of metallic implants using orthovoltage computed tomography *Medical Physics* **35** 1932-41

Zheng Y, Newhauser W, Klein E and Low D 2009 Monte Carlo simulation of the neutron spectral fluence and dose equivalent for use in shielding a proton therapy vault *Physics in Medicine and Biology* **54** 6943-57

VITA

Ming Yang was born in Xi'an, Shaanxi Province, P.R.China on April 19, 1980, the Son of Fengying Zhao and Jincheng Yang. After graduating from Xi'an 85th High School, Xi'an, P.R.China in 1998, he entered University of Science and Technology of China (USTC) in Hefei, Anhui Province, P.R.China. He received the degree of Bachelor of Science with a major in Applied Physics from USTC in July of 2003. In August of 2003, he entered Rice University in Houston, Texas, and received the degree of Master of Science with a major in physics in May of 2006. In August of 2006, he entered The University of Texas Health Science Center at Houston Graduate School of Biomedical Sciences.

Permanent address:

Zi Wei Garden, Room# 11-321

249 First Dian Zi Street

Xi'an, Shaanxi Province, P.R.China 710065